

Quantitative biomedical imaging of magnetic nanoparticles by magnetorelaxometry with optically pumped magnetometers

Dissertation

zur Erlangung des akademischen Grades
Doctor technicae (Dr. techn)

verfasst im Rahmen des
Doktoratsstudiums Technische Wissenschaften

vorgelegt von:
Dipl.-Ing. Mag. rer. nat. Aaron Jaufenthaler BSc.

betreut von:
Univ.-Prof. Dr.-Ing. Daniel Baumgarten

an der
UMIT – Private Universität für Gesundheitswissenschaften,
Medizinische Informatik und Technik

Institut für Elektrotechnik und Biomedizinische Technik

Hall in Tirol, Mai 2022

Abstract

Magnetic nanoparticles (MNP) offer a large variety of promising applications in medicine, e.g., magnetic hyperthermia and magnetic drug targeting. In magnetic hyperthermia, MNP are injected into a tumor. By applying an alternating magnetic field, the MNP generate heat with the aim of locally ablating tumor tissue. In magnetic drug targeting, the MNP are drug loaded and a magnetic field is used to enrich a region with MNP, leading to local application of the drug. Quantitative imaging of the MNP distributions is crucial for planning and monitoring of these treatments. A promising method therefor is magnetorelaxometry imaging (MRXI). In magnetorelaxometry (MRX), the magnetic moments of superparamagnetic MNP are aligned by applying a constant magnetic excitation field. After rapidly switching off the excitation field, the relaxation of the MNP's net magnetic moment is monitored by a magnetometer. The MNP can be quantified and their binding state can be extracted by analyzing the relaxation curve. In MRXI, quantitative spatial information about the MNP distribution is obtained by repeating the MRX procedure with spatially different excitation fields and solving an ill-posed inverse problem. State of the art magnetometers for measuring the MNP's relaxation signals are superconducting quantum interference devices (SQUID). Recent developments in laser physics enabled novel optically pumped magnetometers (OPM) reaching similar sensitivities in the low $\text{fT}/\sqrt{\text{Hz}}$ range. OPM offer flexible sensor positioning and the omission of cryogenic cooling, potentially facilitating the translation of MRXI towards clinical applications.

The general objective of this thesis was to investigate the potential of commercial and noncommercial OPM for MRX and MRXI, with respect to biomedical applications and operation in real world scenarios. This includes the investigation of the principal applicability of OPM for a single channel MRX system, as well as the challenging translation to a multichannel MRXI system. A prerequisite for both is the investigation and optimization of different parameters like dead time, bandwidth, sensitivity and sensor crosstalk. To reach these goals, several experiments were designed from ground up in the course of this thesis. Custom pulsed current sources for the excitation fields in MRX and MRXI were built and characterized. Different clinically relevant MNP were selected for the experiments, including Resovist[®], Bionized NanoFerrite (BNF) and Perimag[®]. Three different types of OPM were investigated. A major challenge was the development and evaluation of novel readout and data analysis techniques for each sensor type.

In a first step, it could be demonstrated that commercially available OPM are generally suitable for MRX. The quantification results were in good agreement with SQUID measurements. An iron detection limit of $6 \mu\text{g}$ for immobilized Resovist[®] MNP was reached. In an important intermediate step towards MRXI, MRX was extended to 1D reconstruction of MNP distributions. For this study, a single OPM and multiple excitation

coils were used. This avoids sensor crosstalk and the need for channel matching. The setup was later extended to 2D OPM-MRXI, while exploiting flexible sensor positioning. The region of interest was 12 cm by 8 cm. After sensor- and coil localization, as well as solving the inverse problem, point-like MNP distributions with clinically relevant iron concentrations could be reconstructed precisely and accurately.

To exploit this achieved potential also when biomedical applications use fast relaxing MNP, the current 35 ms dead time of the commercial OPM needs to be drastically decreased, while increasing the current bandwidth of 135 Hz. Several OPM operation modes were investigated in this respect. With a novel pulsed free spin precession OPM, we were able to reduce the dead time after switching off the excitation field to several microseconds. The bandwidth could be increased adaptively up to 80 kHz with a tradeoff in sensitivity.

With special interest for magnetic hyperthermia and nonlinear MRXI, it was demonstrated, that excitation fields as high as 100 mT can be tolerated by OPM. Further experiments showed, that not only the relaxation of MNP can be measured with OPM, but also their magnetization behavior, which offers novel encoding techniques for MRXI. In order to even more facilitate the use of MRX, an OPM setup for unshielded MRX was envisioned. To achieve this goal, the influence of background magnetic fields, e.g., the Earth magnetic field on the relaxation parameters was investigated. It could be shown, that these parameters are significantly altered by the background magnetic field and need to be considered in real world applications. Novel spatial encoding techniques by applying background magnetic fields are envisioned.

Based on the high adaptive bandwidth, short dead time, the findings at different background magnetic fields and a gradiometric detection scheme, quantification of BNF-MNP (which are also used in magnetic hyperthermia) in liquid suspension could be successfully demonstrated. In an unshielded laboratory environment with a novel portable tabletop system, an outstanding iron detection limit of 1.37 μg was reached.

In this thesis it was demonstrated, that OPM have high potential for MRX and MRXI. First, SQUID-like sensitivities were reached. Further, clinically relevant MNP with relaxation times ranging from sub-millisecond up to several seconds were detected. Therefore, OPM-MRX and OPM-MRXI are promising for the use in biomedical applications. The flexible sensor positioning and the omission of cryogenic cooling facilitate the use of OPM in real world scenarios. Finally, unshielded OPM-MRX was successfully demonstrated. These findings are a profound foundation for future OPM-MRXI research towards the combination of MRXI and biomedical applications. Unshielded OPM-MRXI and the use with magnetic hyperthermia is envisioned.

Kurzfassung

Magnetische Nanopartikel (MNP) bieten vielversprechende Anwendungen in der Medizin, z. B. magnetische Hyperthermie und magnetisches Drug Targeting. Bei der magnetischen Hyperthermie werden die MNP in einen Tumor injiziert. Durch Anlegen eines magnetischen Wechselfeldes erzeugen die MNP Wärme, um so das Tumorgewebe lokal zu veröden. Beim magnetischen Drug Targeting werden MNP mit Medikamenten beladen. Mit Hilfe eines Magnetfeldes werden die MNP in einer Region angereichert, was zu einer lokalen Anwendung des Medikaments führt. Dadurch werden unerwünschte Nebenwirkungen an anderen Stellen im Körper minimiert. Eine quantitative Bildgebung der MNP-Verteilung im Körper ist für die Planung und Überwachung dieser Behandlungen essentiell. Eine vielversprechende Methode dafür ist die „Bildgebung mittels Magnetorelaxometrie“ (MRXI). Bei der Magnetorelaxometrie (MRX) werden die magnetischen Momente der superparamagnetischen MNP durch Anlegen eines konstanten magnetischen Anregungsfeldes ausgerichtet. Nach schnellem Abschalten des Anregungsfeldes wird die Relaxation der MNP mit einem Magnetfeldsensor gemessen. Durch Analyse der Relaxationskurve können die MNP quantifiziert und ihr Bindungszustand bestimmt werden. Bei MRXI werden quantitative räumliche Informationen über die MNP-Verteilung gewonnen, indem das MRX-Verfahren mit unterschiedlichen Anregungsfeldern wiederholt, und ein schlecht gestelltes inverses Problem gelöst wird. Die modernsten Magnetometer zur Messung der MNP-Relaxationssignale sind supraleitende Quanteninterferenzgeräte (SQUID). Jüngste Entwicklungen in der Laserphysik ermöglichen neuartige optisch gepumpte Magnetometer (OPM), die ähnliche Empfindlichkeiten im niedrigen $fT/\sqrt{\text{Hz}}$ -Bereich erreichen. OPM bieten eine flexible Sensorpositionierung und den Wegfall der kryogenen Kühlung, was die Umsetzung von MRXI in klinische Anwendungen erleichtern könnte.

Das Ziel dieser Arbeit war die Untersuchung des Potenzials kommerzieller und nichtkommerzieller OPM für MRX und MRXI im Hinblick auf biomedizinische Anwendungen und den Betrieb in realitätsnahen Szenarien. Dies beinhaltet sowohl die grundlegende Untersuchung der Geeignetheit von OPM für ein einkanaliges MRX-System, als auch den komplexen Übergang in ein mehrkanaliges MRXI-System. Die Voraussetzung dafür sind die Untersuchung und die Optimierung verschiedener Parameter wie Totzeit, Bandbreite, Empfindlichkeit und gegenseitige Beeinflussung der Sensoren.

Um diese Ziele zu erreichen, wurden im Rahmen dieser Arbeit mehrere Experimente von Grund auf konzipiert. Gepulste Stromquellen für die Anregungsfelder in MRX und MRXI wurden gebaut und charakterisiert. Verschiedene klinisch relevante MNP wurden für die Experimente ausgewählt, darunter Resovist[®], Bionized NanoFerrite (BNF) und Perimag[®]. Insgesamt konnten drei verschiedene Arten von OPM untersucht werden. Eine große Herausforderung war die Entwicklung und Charakterisierung neuartiger

Auslese- und Datenanalysetechniken für jeden einzelnen Sensortyp.

In einem ersten Schritt konnte gezeigt werden, dass handelsübliche OPM generell für MRX geeignet sind. Die Quantifizierungsergebnisse wiesen eine gute Übereinstimmung mit den SQUID-Messungen auf. Eine Detektionsgrenze von 6 μg Eisen für immobilisierte Resovist[®] MNP wurde erreicht. In einem wichtigen Zwischenschritt in Richtung MRXI, wurde MRX auf die 1D-Rekonstruktion von MNP-Verteilungen erweitert. Für diese Studie wurden ein einzelner OPM und mehrere Erregerspulen verwendet. Dadurch wird ein Übersprechen der Sensoren und die Notwendigkeit einer Kanalanpassung vermieden. Der Aufbau wurde später auf 2D OPM-MRXI erweitert, wobei die flexible Positionierung der Sensoren ausgenutzt wurde. Ein 12 cm mal 8 cm großer Bildgebungsbereich wurde realisiert. Nach der Sensor- und Spulenlokalisation, sowie der Lösung des inversen Problems konnten punktförmige MNP-Verteilungen mit klinisch relevanten Eisenkonzentrationen präzise und akkurat rekonstruiert werden.

Um dieses erreichte Potenzial auch bei biomedizinischen Anwendungen mit schnell relaxierenden MNP auszuschöpfen, muss die derzeitige Totzeit des kommerziellen OPM von 35 ms drastisch gesenkt und gleichzeitig die aktuelle Bandbreite (135 Hz) erhöht werden. In diesem Zusammenhang wurden mehrere OPM-Betriebsarten untersucht. Mit einem neuartigen gepulsten OPM mit freier Spinpräzession konnten wir die Totzeit nach dem Abschalten des Anregungsfeldes auf einige Mikrosekunden reduzieren. Die Bandbreite konnte adaptiv bis zu 80 kHz erhöht werden, wobei stets ein Kompromiss zwischen Bandbreite und Sensitivität gewählt werden muss.

Es wurde gezeigt, dass Anregungsfelder bis zu 100 mT von OPM toleriert werden können. Dies ist von besonderem Interesse für die magnetische Hyperthermie und die nichtlineare MRXI. Weitere Experimente zeigten, dass nicht nur die Relaxation von MNP mit OPM gemessen werden kann, sondern auch deren Magnetisierungsverhalten, was neuartige Kodierungstechniken für MRXI ermöglicht.

Um den Einsatz von MRX noch weiter zu erleichtern, wurde ein OPM-Aufbau für ungeschirmtes MRX ins Auge gefasst. Um dieses Ziel zu erreichen, wurde der Einfluss von Hintergrundmagnetfeldern, z.B. des Erdmagnetfeldes, auf die Relaxationsparameter untersucht. Es konnte gezeigt werden, dass diese Parameter durch das Hintergrundmagnetfeld erheblich verändert werden und in realen Anwendungen berücksichtigt werden müssen. Auch dies könnte zu neuartigen räumlichen Kodierungstechniken führen.

Basierend auf der hohen adaptiven Bandbreite, der kurzen Totzeit, den Ergebnissen bei unterschiedlichen Hintergrundmagnetfeldern und einem gradiometrischen Detektionsschema konnte die Quantifizierung von BNF-MNP (die auch in der magnetischen Hyperthermie eingesetzt werden) in flüssiger Suspension erfolgreich demonstriert werden. In einer ungeschirmten Laborumgebung mit einem neuartigen tragbaren Tischsystem wurde eine herausragende Detektionsgrenze von 1.37 μg Eisen erreicht.

In dieser Arbeit wurde gezeigt, dass OPM ein hohes Potenzial für MRX und MRXI haben. Zunächst wurden SQUID-ähnliche Empfindlichkeiten erreicht. Darüber hinaus wurde gezeigt, dass klinisch relevante MNP mit Relaxationszeiten im Bereich von Sub-Millisekunden bis hin zu mehreren Sekunden detektierbar sind. Daher sind OPM-MRX und OPM-MRXI vielversprechend für den Einsatz in biomedizinischen Anwendungen.

Die flexible Positionierung der Sensoren und der Wegfall der kryogenen Kühlung erleichtern den Einsatz von OPM in realen Szenarien. Schließlich wurde ungeschirmtes OPM-MRX erfolgreich demonstriert.

Diese Ergebnisse bilden eine wesentliche Grundlage für künftige OPM-MRXI-Forschung in Richtung Kombination von MRXI und biomedizinischen Anwendungen. Ungeschirmtes OPM-MRXI und der Einsatz in der magnetischen Hyperthermie scheinen erreichbar.

Contents

1	Introduction and motivation	1
2	Theoretical background	3
2.1	Magnetic nanoparticles – definition, properties and biomedical applications	3
2.2	MNP relaxation dynamics and Magnetorelaxometry (MRX)	4
2.2.1	Relaxation dynamics	4
2.2.2	Magnetorelaxometry	5
2.2.3	Relaxation signal modeling and parameter estimation	6
2.3	Magnetorelaxometry Imaging (MRXI)	7
2.4	Superconducting Quantum Interference Device (SQUID)	10
2.5	Optically Pumped Magnetometers (OPM)	12
2.5.1	Introduction	12
2.5.2	Bloch equations	12
2.5.3	Alkali atoms: ^{87}Rb and Cs	14
2.5.4	Optical pumping, interaction with magnetic fields and optical probing	16
2.6	Selected OPM operation modes	18
2.6.1	Introduction	18
2.6.2	Spin Exchange Relaxation Free (SERF) magnetometer	19
2.6.3	Intensity Modulated (IM) magnetometer	20
2.6.4	Free-Spin-Precession (FSP) magnetometer	22
2.6.5	Feedback-controlled OPM	24
2.6.6	Vectorizing a scalar OPM	24
3	State of the art	28
3.1	Optically pumped magnetometers: sensitivity and other parameters with respect to MRX(I)	28
3.2	Magnetorelaxometry using different magnetometers	29
3.3	Magnetorelaxometry imaging: experiments in literature	31
3.4	Other selected MNP imaging techniques	32
4	Objective and scope of the thesis	34
5	Materials and methods	36
5.1	Optically pumped magnetometers	36
5.1.1	QZFM from QuSpin	36
5.1.2	Intensity modulated OPM from Leibniz-IPHT	36

5.1.3	OMG from Twinleaf	37
5.2	Magnetic nanoparticles	38
5.2.1	Resovist	38
5.2.2	Bionized NanoFerrite (BNF)	38
5.2.3	Perimag	39
5.2.4	Berlin Heart	39
5.2.5	Which MNP sizes contribute to the measured MRX signal?	39
5.3	Pulsed current sources for MRX	40
6	From quantification to imaging	46
6.1	Introduction	46
6.2	Quantification of MNP with QZFM from QuSpin	46
6.2.1	Objectives	46
6.2.2	Materials and Methods	46
6.2.3	Results	48
6.2.4	Discussion	49
6.3	1D reconstruction of MNP distributions	51
6.3.1	Objectives	51
6.3.2	Materials and Methods	51
6.3.3	Results	52
6.3.4	Discussion	53
6.4	2D imaging of MNP with OPM-MRXI	53
6.4.1	Objectives	53
6.4.2	Materials and Methods	54
6.4.3	Results	54
6.4.4	Discussion	55
6.5	Summary	56
7	Investigation and optimization of selected parameters	57
7.1	Introduction	57
7.2	Investigating OPM bandwidth and dead time with a pulsed free-spin- precession magnetometer	57
7.2.1	Objectives	57
7.2.2	Materials and Methods	58
7.2.3	Results	60
7.2.4	Discussion	65
7.3	High excitation fields in OPM-MRX	65
7.3.1	Objectives	65
7.3.2	Materials and Methods	65
7.3.3	Results	67
7.3.4	Discussion	68
7.4	OPM-MRX at DC background fields	69
7.4.1	Objectives	69
7.4.2	Materials and Methods	69

7.4.3	Results	70
7.4.4	Discussion	76
7.5	MNP alignment measurement with an OPM	77
7.5.1	Introduction and Objectives	77
7.5.2	Materials and Methods	77
7.5.3	Results	78
7.5.4	Discussion	78
7.6	Summary	79
8	Unshielded OPM-MRX	80
8.1	Objectives	80
8.2	Materials and Methods	80
8.3	Results	81
8.4	Discussion	85
9	Conclusion and Outlook	87
9.1	Conclusion	87
9.2	New opportunities of OPM-MRXI for human applications	88
9.2.1	OPM-MRXI for human applications – glioblastoma imaging	88
9.2.2	OPM-MRXI in unshielded environments	89
	Nomenclature	91
	List of Figures	92
	List of Tables	97
	Bibliography	98
	Scientific contributions	117
	Peer-reviewed publications	117
	Book chapter	117
	Poster presentations at scientific conferences	117
	Oral presentations at scientific conferences	119
	Invited oral presentations	119

1 Introduction and motivation

The title of this thesis *Quantitative biomedical imaging of magnetic nanoparticles by magnetorelaxometry with optically pumped magnetometers* builds on many interdisciplinary key words, connecting biomedicine with quantum- and nanotechnology. Nanotechnology is rapidly growing in the last decades. Generally, nano implies something very small in size, since one nanometer (1 nm) is 10^{-9} m. A common known example for nanotechnology is the so called nano-coating, a layer which repels water like the lotus flower. Another example is nanoelectronics, currently reaching node size in the single digit nanometer range. Nanowaste and nanopollution e.g., from car tires are well discussed topics in environmental protection. Nanoparticles are indispensable in cosmetics and medicine. In this thesis, only (synthetic) nanoparticles with a magnetic core are considered, which are called magnetic nanoparticles (MNP). They can be used in biomedicine as contrast agents or biomarkers, for magnetic separation, magnetic drug targeting, or the especially promising method of magnetic hyperthermia. For most of these applications there's a strong need in *quantitative* imaging of the particle distributions for treatment planning and monitoring. A promising technique therefor is magnetorelaxometry (MRX) imaging, which requires ultra high sensitivity magnetometers. Currently, superconducting quantum interference devices (SQUID) are used as magnetometers, with the drawback of expense operation costs due to the required cryogenic cooling. The thermal insulation shell limits the distance to the magnetic nanoparticles. Further, the thermal insulation limits the flexibility of the imaging setup, i.e., the placement of sensors. A novel type of sensors, called optically pumped magnetometers (OPM) or quantum magnetometers might have the potential to drastically improve these limitations. OPM exploit the interaction of spins with electric fields (e.g., laser light) and magnetic fields to measure magnetic fields with extremely high sensitivity. While the basic principle was known for long time, only recent developments made them competitive or complementary to SQUID. In the recent years, companies also started to commercialize OPM, promising a rapid distribution of the technology.

The general objective of this thesis is to investigate the potential of commercial and non-commercial OPM for magnetorelaxometry and magnetorelaxometry imaging of magnetic nanoparticles, with respect to biomedical applications and operation in real world scenarios. A detailed description of the objective is presented in Chapter 4, after introducing the theoretical background in Chapter 2, to allow for a better understanding of the details and challenges of this work.

If this potential can be shown, the OPM's flexible positioning might be used to improve the inverse problem in MRXI. As a result, the reconstruction quality might be increased and/or the data acquisition time during an examination might be reduced. The flexible

positioning would further allow for the construction of patient specific or disease specific MRXI setups. With the omission of cryogenic cooling, the operation cost could be drastically reduced, since no liquid helium cycle is needed. The decrease of the thermal insulation thickness would allow for minimized sensor to target distance, potentially improving the signal to noise ratio of measurements. On top of that, specific OPM might be suitable for the operation in moderately shielded or even unshielded environments, drastically accelerating the acceptance of the relatively new technology MRXI. These benefits could make OPM-MRXI setups feasible even for smaller facilities. The biomedical applications like magnetic drug targeting and magnetic hyperthermia would benefit from these developments. In conclusion, quantitative imaging like OPM-MRXI would be the key for safe and efficient treatments.

This thesis is structured as follows: In Chapter 2, the theoretical background of magnetic nanoparticles (Section 2.1), relaxation dynamics and magnetorelaxometry (Section 2.2), magnetorelaxometry imaging (Section 2.3), SQUID (Section 2.4) and optically pumped magnetometers (Sections 2.5 and 2.6) is elaborated. In Chapter 3, the state of the art of OPM, MRX, MRXI and other selected MNP imaging techniques is presented. After defining the detailed objective and scope of the thesis in Chapter 4, the material and methods used in the experimental work of this thesis is presented in Chapter 5. Chapter 6 treats the applicability of OPM for MRX and the translation to OPM-MRXI. Selected parameters of OPM for MRX and MRXI are investigated and optimized in Chapter 7. Finally, unshielded MRX measurements are presented in Chapter 8. An outlook is given in Chapter 9.

It should be noted, that parts of this work were previously published in several scientific journals [Jau20a, Jau20b, Jau21, Sch21], in a book chapter [Lebed], and were presented at numerous scientific conferences (see Appendix).

The work from [Jau20a, Jau20b, Jau21] is reported here with partial modification and are originally licensed under a Creative Commons Attribution 4.0 International License (CC BY 4.0).

2 Theoretical background

2.1 Magnetic nanoparticles – definition, properties and biomedical applications

Magnetic nanoparticles (MNP) are composed of one or multiple magnetic cores and a nonmagnetic shell. MNP have in common, that their diameter typically ranges from a few nm up to about 100 nm. The very broad class of magnetic nanomaterials can be classified by a rich set of parameters, ranging from geometrical properties, over magnetic properties to biological properties. However, the standardization of MNP and MNP characterization is still an ongoing process [Ort13, Bog15, Sch19a, RR21, Ped21]. An important factor for biomedical applications is the biocompatibility of the MNP, which is enabled by encapsulating the magnetic material of the MNP with a biocompatible shell [Dut20]. Further, the shell needs to prevent the MNP from agglomerating, which would alter the MNP's properties and therefore challenging treatment control and safety. The most common types of MNP are composed of magnetite (Fe_3O_4) or maghemite (Fe_2O_3) [Akb12], and non-functionalized shells are composed, e.g., of starch or dextran.

Biomedical applications of MNP include magnetic hyperthermia, MRI contrast agents, magnetic separation and targeted drug delivery [Pan03, Pan09, Shu09]. Contrast agents are widely used in MRI to detect blood brain barrier disruption, aneurysms, clogged blood vessels or increased vascular permeability [Wah18]. Gadolinium based contrast agents are predominantly used, but in the recent years long-term safety concerns arised [Kan16, Wah18]. Lately, MNP are developing towards a promising alternative [Sun08, Wah18]. Another use case for MNP is magnetic drug targeting, where the MNP are drug loaded and a magnetic field is used to enrich a region with MNP and therefore with the drug. As a result, the drug will lead to less adverse effects in not-to-be-treated tissue, and a smaller overall drug dose can be administered [Lüb96, Lüb01, Pan03, Che08]. By means of coating the MNP with antibodies or other molecules, the MNP will specifically bind to a target, e.g., a tumor [Mod14], bacteria [Lee14] or red blood cells [Mol82]. Through (quantitative) imaging of these bound MNP, the target distribution can be monitored. If the fluid containing the MNP is accessible, the MNP including the bound target can be removed by magnetic separation. In a magnetic separator, the fluid is exposed to a magnetic field gradient, dragging the MNP aside [Pan03]. Another very promising application of MNP is magnetic hyperthermia. The idea is to deliver MNP to a tumor region and to locally ablate the tissue. The tissue is indirectly heated by applying AC magnetic fields to the MNP. The underlying physical processes of MNP's heat generation are susceptibility loss, viscous heating (friction) and hysteresis loss, while the

latter is the prominently exploited one [He18]. A magnetic field applied for hyperthermia might have a frequency $f = 100$ kHz and a field strength $H = 20$ kA/m [Fer21]. However, these parameters do strongly vary in literature. A common parameter is the product of f and H , which needs to be below 5×10^9 A/(s m) to avoid high eddy currents in the patient's tissue and therefore discomfort. Nevertheless, remarkable heating can be achieved using these parameters, reaching specific absorption rates of 250 W/g and higher [Gav21]. If the location of MNP is precisely controlled, the main advantage of magnetic hyperthermia can be claimed as the possibility of generating local heat, conserving surrounding tissue. Quantitative imaging of the local MNP distribution, which is still challenging, significantly improves treatment planning and monitoring [RR21, Fer21] and is a requirement to translate hyperthermia to clinics [Hea22].

2.2 MNP relaxation dynamics and Magnetorelaxometry (MRX)

2.2.1 Relaxation dynamics

The dynamics of the MNP's magnetic moments can be described by two processes, namely Brownian and Néel relaxation. Whole particle rotation is named Brownian relaxation and the rotation of the MNP's internal magnetization is called Néel relaxation. The zero field Néel relaxation time is defined as [Née49]:

$$\tau_N = \tau_0 \exp\left(\frac{KV_c}{k_B T}\right), \quad (2.1)$$

where τ_0 is the damping time, K is the effective magnetic anisotropy, V_c is the particle's core volume, k_B is the Boltzmann constant and T is the temperature. In the presence of an external magnetic field H (i.e., H_{ex}), the Néel relaxation time expands to [Née49]:

$$\tau_N(H) = \tau_0 \exp\left(\frac{KV_c(1 - h^2)}{k_B T}\right), \quad (2.2)$$

with $h = H/H_k$, where $H_k = 2K/(\mu_0 M_s)$ is the anisotropy field, with the saturation magnetization M_s . It has been shown experimentally using SQUID, that Néel relaxation can be accelerated by applying external magnetic fields [Sar09b].

The Brownian relaxation time τ_B depends on the viscosity η , the particle's hydrodynamic volume V_h and the temperature T [BJ63]:

$$\tau_B = \frac{3\eta V_h}{k_B T}. \quad (2.3)$$

In the presence of a background magnetic field, the Brownian relaxation time needs to be extended [Sar11].

If the MNP are freely moving, e.g., if they are suspended in a liquid, both processes occur

in parallel, while the faster process dominates. This results in an effective relaxation time τ_{eff} [Rai94]:

$$\tau_{\text{eff}} = \frac{\tau_{\text{N}}\tau_{\text{B}}}{\tau_{\text{N}} + \tau_{\text{B}}}. \quad (2.4)$$

The Brownian relaxation time, the Néel relaxation time, and the effective relaxation time in dependence of the core and hydrodynamic diameter of MNP are visualized in Figure 2.1. A constant shell thickness of 10 nm is assumed.

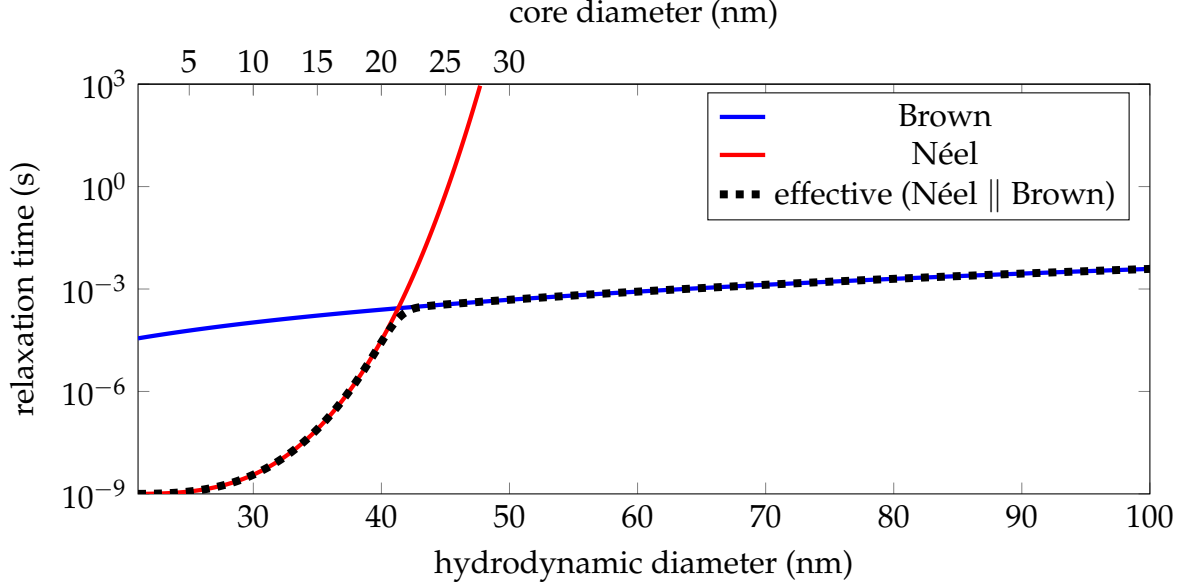


Figure 2.1: Relaxation time constants in dependence of core and hydrodynamic diameter. The MNP's shell thickness is selected as 10 nm, $T = 293.15$ K, $\kappa = 1 \times 10^4$ J/m³, $\tau_0 = 1 \times 10^{-9}$ s and $\eta = 0.01$ Pa s.

2.2.2 Magnetorelaxometry

In magnetorelaxometry (MRX), an external magnetic field H_{ex} , called excitation or magnetization field, is applied to an MNP sample. The magnetic moment of each MNP tends to orient with the field, forming a net magnetic moment. After switching-off the excitation field, the net magnetic moment decays, which can be described by Brownian and Néel relaxation. It is now desired to monitor the magnetization dynamics using a magnetometer. The basic principle of MRX is also visualized in Figure 2.2. At this point it should be pointed out, that the dynamics observed during the excitation phase and during the relaxation phase are not equivalent. This will be discussed in further detail in Section 7.5. At a distance of several millimeters between the magnetometer and an MNP sample with a clinically relevant iron concentration, a magnetometer sensitivity in the fT/ $\sqrt{\text{Hz}}$ to the low pT/ $\sqrt{\text{Hz}}$ is required [Wie12a]. Since most sensitive magnetometers, e.g., commercially available SQUID-magnetometers, are not designed to operate during millitesla excitation fields, only the relaxation signals are investigated. The amplitude of the relaxation signal can be used for quantifying an MNP sample. Further,

by analyzing the temporal properties of the relaxation curve, the MNP's binding state can be obtained [Lie15].

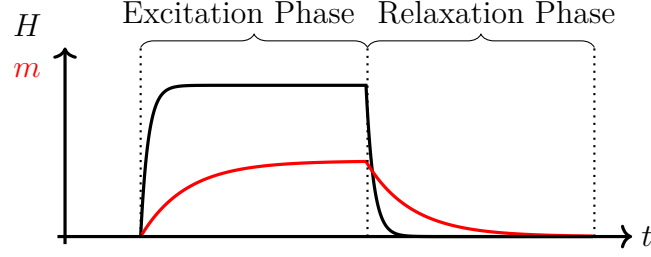


Figure 2.2: Basic principle of magnetorelaxometry. The external field B is shown in black. The MNP's net magnetic moment m is shown in red.

2.2.3 Relaxation signal modeling and parameter estimation

The net magnetic moment of an MNP sample can be described by the superposition of the single MNP's magnetic moments. The relaxation of the magnetic moment of the MNP ensemble gives rise to a time dependent net magnetic flux density B at the sensor location, while assuming equal relaxation times for each MNP in the sample [Rai94]:

$$B(t) = B_{\text{relax}} \exp\left(-\frac{t}{\tau_{\text{eff}}}\right) + O, \quad (2.5)$$

with the relaxation amplitude B_{relax} and the offset O . In the case of a sample with multiple diameter fractions, the relaxation can be modeled as superposition of these individual fractions:

$$B(t) = \sum_i B_i \exp\left(-\frac{t}{\tau_i}\right) + O. \quad (2.6)$$

Often, the core and hydrodynamic particle size distribution is reasonably well described by the logarithmic normal distribution. Additionally, MNP might form clusters due to aggregation. A (cluster) moment superposition model (MSM) can be used to describe the relaxation process of real MNP systems [Cha83, Ebe06]:

$$B(t) = a_{\text{sys}} \int_V V P(V) L(V, H, T) \left(1 - e^{-\frac{t_{\text{ex}}}{\tau_{\text{eff}}(K, V, H_{\text{ex}}, T)}} \right) e^{-\frac{t}{\tau_{\text{eff}}(K, V, H_0, T)}} dV + \mu_0 H_0, \quad (2.7)$$

Geometrical properties of the MRX system are described by the parameter a_{sys} . The particle's size distribution is denoted by $P(V)$. In this MSM it is assumed, that the MNP's magnetic moment directly scales with the volume V of the particles, while they relax in a background field H_0 . Further, the finite excitation time t_{ex} is considered. The nonlinear magnetization is taken into account by the Langevin function L . Ideally, the

model should be extended to consider both, the hydrodynamic and core diameter distribution independently. The fit of even a simple MSM to experimental MRX data is an ill-conditioned inverse problem. The parameter variance and mutual interdependence is often very high, not only due to the contribution of environmental noise. Prior knowledge obtained by the means of other measurement techniques is therefore a requirement for a detailed and precise analysis.

An alternative is the phenomenological model of a stretched exponential [Ebe06]:

$$B(t) = B_{\text{relax}} \exp\left(-\left(\frac{t}{\tau_{\text{eff}}}\right)^\beta\right) + O, \quad (2.8)$$

where β is the stretching parameter.

In alternative to the presented models, the magnetization dynamics can be described by differential equations, e.g., Fokker-Planck-equation and Landau-Lifshitz-Gilbert-equation [Ree14, Tei15, Har17]. As modeled mathematically by Fokker-Plank-equations, it has been shown that the Brownian and Néel relaxation times decrease monotonically with increasing magnetic field strength, while for large fields ($> \text{mT}$) Néel relaxation is much more sensitive to magnetic fields [Dei14]. In practical MRX measurements, the detection time of the MRX curve is limited, i.e., a certain dead time and sensor bandwidth prevents or distorts the acquisition of very early parts of the relaxation. The practicality restricts the duration of the measurement. This measurement window defines which diameter fraction of the MNP sample contributes to the measured MRX signal [Dol15, Wie12b, Sch17b]. In experiments the phenomenological parameters ΔB and $t_{1/e}$ are used often to describe the data [Ebe06]. The difference between the first and last measured magnetic field values is the relaxation amplitude ΔB . The time span in which the first measured magnetic field value drops by the factor e is called $t_{1/e}$. If the measurement data has a poor SNR it might be beneficial to fit a model to the data before estimating the parameters ΔB and $t_{1/e}$. When trying to lowpass-filter the data, much attention needs to be paid. First of all, classical filters introduce frequency dependent phase shifts. Zero-phase filters can be practically implemented by forward-backward filtering. The filter realization as Bessel filter is advantageous to preserve sharp edges in the data. The initial parameters of the filter need to be well-chosen.

A robust parameter for the relaxation time is the integral relaxation time [Gar96], often called correlation time [Cof94]. It is denoted as the area under the amplitude-normalized relaxation curve. A benefit of this method is, that no filtering is needed, and no curve-fitting needs to be involved, excluding model uncertainties. In this work, the integral relaxation time is extended to the integral alignment time for measurements of the alignment of the MNP's magnetic moments. Generalized, the two parameters are denoted here as integral time.

2.3 Magnetorelaxometry Imaging (MRXI)

By repeating MRX measurements with different excitation fields and/or by using multiple magnetometers it is possible to obtain quantitative spatial information about the

MNP distribution. This process is called magnetorelaxometry imaging (MRXI). An exemplary MRXI setup, composed of nine vectorial magnetometers and four times nine excitation coils arranged around a region of interest (ROI) is depicted in Figure 2.3.

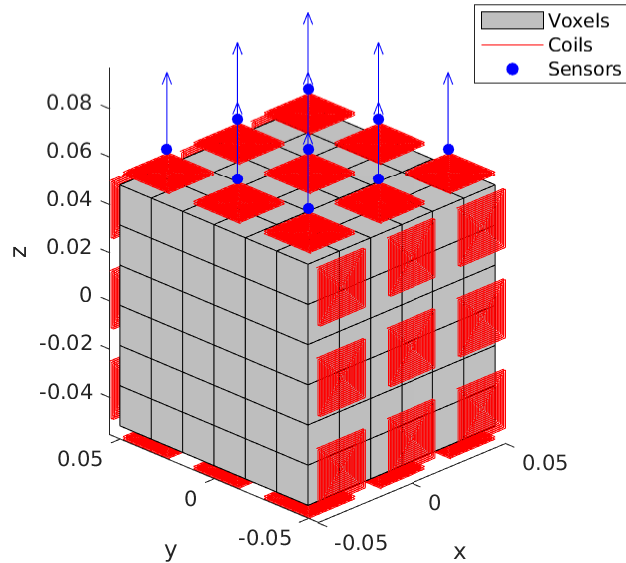


Figure 2.3: Exemplary MRX imaging setup composed of nine vectorial magnetometers (blue) and 36 excitation coils (red) arranged around a region of interest (grey), which is divided into voxels.

The excitation coils are activated in a known sequence (e.g., sequentially), while the relaxation signals are acquired in-between the excitation pulses. For the quantitative imaging of the MNP distribution in the ROI, a forward model for MRX is required. In a first step, the interaction of the active excitation coil(s) and the MNP needs to be modeled. Then, after switching-off the excitation field, the time-dependent magnetic flux density at the sensor's location, which is generated by the MNP, needs to be modeled. This is repeated for each excitation-coil-current configuration. The so-generated mathematical system model can predict the relaxation signals which would be measured by magnetometers given a known quantitative MNP distribution. In MRX imaging the associated inverse problem needs to be solved, i.e., the measured signals need to be transformed into quantitative MNP estimations.

Without referring to intricate optimization problems for improving imaging capabilities, each of the steps described is very complex. In the following paragraphs, several assumptions to reduce the complexity of the problem are described and discussed.

In a first step, the ROI is discretized into N_v voxels. The voxel grid needs to be selected fine enough to reasonably fulfill the assumption of a homogeneous MNP distribution within one voxel. Often, a regular voxel grid is selected. Depending on the size of the voxels, each voxel i might be modeled as single magnetic dipole, or as an array of magnetic dipoles. When the excitation field is switched on, the magnetic moments of the MNP resp. dipoles are aligned with the field. Usually, particle-particle interactions are

neglected not only here, but in the whole modeling process. The applied magnetic field not only determines the orientation of the MNP resp. dipoles, but also the magnitude of magnetization of the ensemble, i.e., the magnitude of the modeled magnetic dipole moment \vec{m} . The magnetization of an MNP ensemble can be described the Langevin function (compare Equation 2.7). If the excitation field H_{ex} is small enough (which usually is the case in MRXI), the model can be linearized and expressed as

$$\vec{m}(\vec{H}_{\text{ex}}) = \chi c \vec{H}_{\text{ex}}, \quad (2.9)$$

where χ is the dynamic susceptibility, i.e., the slope of the Langevin function around $H = 0$ and c is the amount of MNP. It should be noted that there is no magnetization hysteresis in case of superparamagnetic MNP. Since the geometric and magnetic properties of the excitation system are known, the resulting magnetic field at each voxel position can be calculated using the Biot-Savart law [Han02], while geometrical uncertainties of the experimental setup shouldn't be underestimated.

After switching-off the excitation field, the relaxation of the MNP's net magnetic moment needs to be modeled. A spatio-temporal approach is possible but very time consuming [Bau10]. Alternatively, like described in Section 2.2, the relaxation amplitude can be used as measure for the quantity of MNP. This is valid under the assumption of equal average relaxation times within the whole ROI. The magnetic field B produced by a magnetic dipole m at a distance \vec{r} is

$$\vec{B} = \frac{\mu_0}{4\pi} \left(\frac{3\vec{r}(\vec{r} \cdot \vec{m})}{|\vec{r}|^5} - \frac{\vec{m}}{|\vec{r}|^3} \right). \quad (2.10)$$

Thus, a magnetometer detects the superposition of all modeled dipoles m_i with a sensor-dipole-distance r_i

$$\vec{B} = \sum_i \frac{\mu_0}{4\pi} \left(\frac{3\vec{r}_i(\vec{r}_i \cdot \vec{m}_i)}{|\vec{r}_i|^5} - \frac{\vec{m}_i}{|\vec{r}_i|^3} \right). \quad (2.11)$$

Depending on the magnetometer used, vectorial or scalar magnetic field information will be available.

To sum up, \vec{H}_{ex} needs to be computed at each voxel position, then \vec{m} can be calculated for each voxel, and finally \vec{B} at each sensor location is computed. This is repeated for all intended or used excitation fields. With all the assumptions above, the MNP concentration is linear with respect to the measured fields. Therefore, the forward model of a system with N_v voxels, N_s sensors, and N_e excitation sequences can be written as a set of linear equations

$$\mathbf{L} \cdot \vec{c} = \vec{b}, \quad (2.12)$$

with the system matrix or lead field matrix $\mathbf{L} \in \mathbb{R}^{N_s N_e \times N_v}$, the concatenated MNP concentrations (or amounts) of all voxels $\vec{c} \in \mathbb{R}^{N_v}$, and the measured or simulated magnetic field amplitudes $\vec{b} \in \mathbb{R}^{N_s N_e}$.

The associated inverse problem (i.e., we solve Equation 2.12 for \vec{c}) is usually ill-conditioned, appealing regularization techniques, which incorporate a priori information about the

MNP distribution. The condition number

$$\text{cond}(\mathbf{L}) = \|\mathbf{L}\| \|\mathbf{L}^+\| = \frac{\sigma_{\max}(\mathbf{L})}{\sigma_{\min}(\mathbf{L})} \quad (2.13)$$

is an indicator on how strongly measurement noise is amplified when solving the inverse problem. \mathbf{L}^+ is the pseudoinverse of \mathbf{L} , and $\sigma_{\max}(\mathbf{L})$ resp. $\sigma_{\min}(\mathbf{L})$ denote the maximum resp. minimum singular value of \mathbf{L} . The lower bound of the reconstruction error, without accounting for model uncertainties, can be stated as

$$\frac{\|\delta\vec{c}\|}{\|\vec{c}\|} \leq \text{cond}(\mathbf{L}) \cdot \frac{\|\delta\vec{b}\|}{\|\vec{b}\|}, \quad (2.14)$$

with $\delta\vec{b}$ denoting the noise of the measured relaxation amplitudes and $\delta\vec{c}$ the deviation from the true quantitative MNP distribution \vec{c} .

For the solution of this inverse problem, a non-negativity constraint is recommended since the amount of MNP cannot be negative. Depending on the expected MNP distribution shape, l_1 or l_2 regularization might be selected. For a discussion about iterated Tikhonov (l_2 regularization) and sensitivity weighted iterative shrinkage-thresholding algorithm (l_1 regularization) see [Sch19b].

A short note about the notation in this work: The abbreviation MRX stands for magnetorelaxometry using a single magnetometer, MRXI stands for magnetorelaxometry imaging, usually employing multiple magnetometers and the abbreviation MRX(I) means both, MRX and MRXI.

2.4 Superconducting Quantum Interference Device (SQUID)

Superconducting Quantum Interference Devices (SQUID) are well established and extremely sensitive sensors for measuring magnetic flux. Direct current, low-temperature SQUID (DC LTS SQUID) currently reach sub-fT sensitivities [Sto16, Gra21], are very robust and are even operated underwater [Chw19]. An understanding of the basic principle, operating parameters and limiting factors of SQUID is crucial, since they are state of the art magnetometers and are predominantly used as reference in literature for MRX(I) measurements.

DC SQUID consist of a superconducting loop, which is interrupted by two Josephson junctions. Josephson junctions are very thin barriers, where electric currents can flow by tunneling electrons (Cooper pairs) through this barrier. To reach the superconducting state, the pickup loop needs to be cooled to a very low temperature (e.g. below 10 K for niobium). The flux inside a superconducting loop (with or without Josephson junctions) can only be integer multiples of the magnetic flux quantum ϕ_0 . This effect is called flux quantization: If an external magnetic flux is applied, a self-induced current flows through the superconducting loop to compensate the flux in units of ϕ_0 . In other words,

if the external flux ϕ is an integer multiple of ϕ_0 , no current flows. In all other cases, a compensation current flows. This current needs to be measured to deduce the applied flux. For this, two Josephson junctions are inserted and a bias constant current is sent through the two parts of the loop (see Figure 2.4). The combination of the Josephson junctions and the bias current leads to a voltage drop across the superconducting loop, which can be measured. Any additional circulating current in the loop, which is generated by the external magnetic flux to be measured, generates an additional voltage drop. In consequence, the magnetic flux modulo ϕ_0 can be measured. The transfer function is well approximated by a sine. The dynamic range ΔB of such a SQUID with a loop radius $r = 1$ mm is $\frac{\phi_0}{r \cdot 2\pi} = 0.7$ nT. To linearize the system response and to increase the dynamic range, SQUID are operated in a feedback loop in practical realizations. Here, the flux inside the superconducting is always compensated via negative feedback (see ϕ_{FB} in Figure 2.4). This operation mode is called flux-locked loop (FLL) [Sch17a].

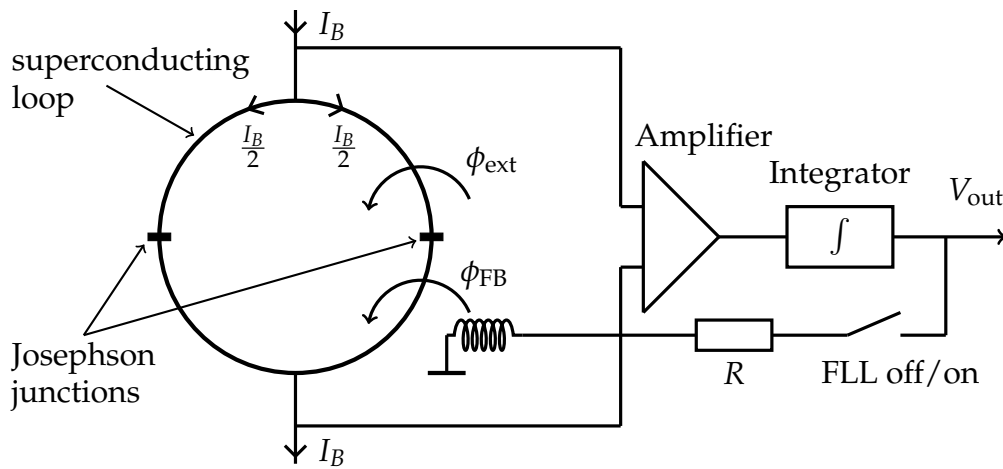


Figure 2.4: Basic operating principle of a SQUID magnetometer, measuring the external magnetic flux ϕ_{ext} . The SQUID signal is linearized using a flux locked loop (FLL), consisting of an amplifier, an integrator, a shunt resistor R and a coil, which feeds back a flux ϕ_{FB} , thus compensating ϕ_{ext} within the loop.

With respect to MRX(I), several issues might arise: In MRX(I), magnetic fields in the millitesla region are applied to MNP and nearby sensors. This might cause flux trapping in the superconducting loop and/or the Josephson junctions, rendering the SQUID unusable. It then needs to be degaussed or heated above the critical temperature [Mat17], which is time consuming and increases the dead time after switching off the external fields. Therefore, flux trapping needs to be avoided. Further, the MRX(I) excitation fields are switched off fast, i.e. in a few microseconds [Lie16, Jau21]. High temporal field gradients require fast SQUID electronics. Thus, wide bandwidth amplifiers and integrators are needed. Special care needs to be taken to avoid instability of the feedback loop. In MRX(I) this technical challenge is usually avoided by completely disabling the FLL during MNP magnetization. More details about SQUID-MRX(I) are presented in Section 3.2.

2.5 Optically Pumped Magnetometers (OPM)

2.5.1 Introduction

Optically pumped magnetometers, also called quantum magnetometers or atomic magnetometers are quantum sensors, which exploit (laser) light for the preparation and interrogation of collective atomic spin states. External magnetic fields, which are to be measured, alter the spin states, too. This combination allows for building today's most sensitive magnetometers, besides SQUID.

An OPM usually consists of a cell filled with alkali atoms, one or multiple lasers, which is/are shined through the cell, and a photodiode or polarimeter behind the cell to detect the absorption or polarization of the transmitted laser light.

To give a very rough idea of today's mostly used commercially available OPM, one can imagine a minimalistic setup consisting of a laser, which shines light through an alkali atom cell onto a photodiode. At nearly zero background magnetic field, the light intensity detected by the photodiode is indirectly proportional to the amplitude of the magnetic field to be measured.

In this section, the basic principles of OPM are described and several OPM operation modes are discussed.

2.5.2 Bloch equations

Bloch equations can be used to describe the macroscopic spin dynamics of an OPM. The spin polarization \vec{S} is built up using optical pumping, counteracted by spin relaxation. An applied magnetic field \vec{B} with field components perpendicular to \vec{S} will tilt the magnetization. If the amplitude of the applied field is high enough or the optical pumping is interrupted, the spin will precess. The Bloch equations are denoted:

$$\frac{d\vec{S}}{dt} = \gamma\vec{S} \times \vec{B} - \Gamma_R\vec{S} + \Gamma_P (S_{\max} \cdot \vec{e}_P - \vec{S}), \quad (2.15)$$

with the gyromagnetic ratio γ , the relaxation rate Γ_R , the pumping rate Γ_P , the maximum polarization S_{\max} and the pumping direction \vec{e}_P . Here, isotropic relaxation rates (spin coherence lifetimes) are assumed. Four steady state solutions of the Bloch equations are shown in Figure 2.5. An exemplary transient solution, namely free spin precession, is shown in Figure 2.6.

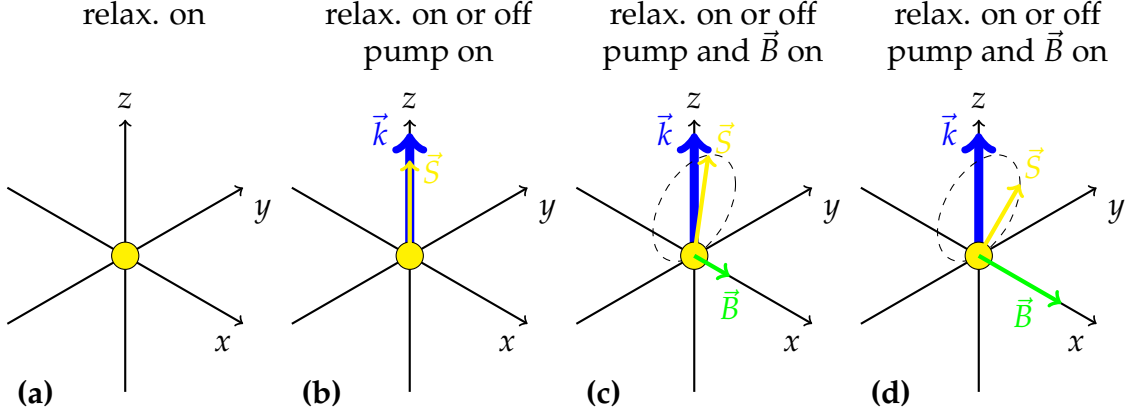


Figure 2.5: Exemplary steady state solutions of Bloch equations: **(a)** relaxed spin ensemble (yellow). **(b)** A circularly polarized pump laser (\vec{k}) is applied in z-direction, which polarizes individual spins, building up a collective spin \vec{S} (yellow). **(c)** In addition to optical pumping a small, constant magnetic field \vec{B} (green) is applied in x-direction. **(d)** Same as **(c)**, but with a larger \vec{B} .

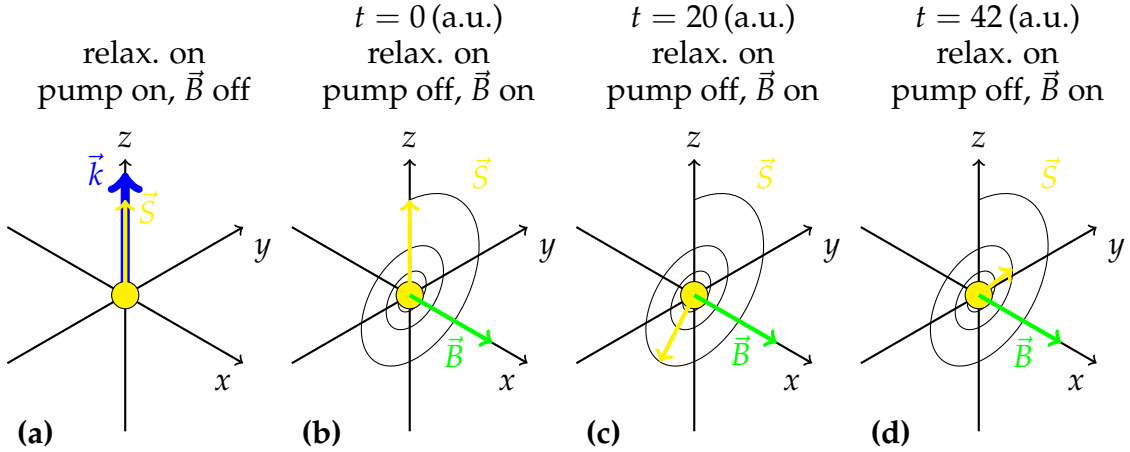


Figure 2.6: Exemplary transient solution of Bloch equations: **(a)** the spin ensemble (yellow) is polarized by optical pumping. **(b, c, d)** The pump laser is switched off and a moderate magnetic field \vec{B} (green) is applied, leading to spin precession over time. The macroscopic spin is exponentially damped (spin relaxation). **(b)** $t = 0$ (arbitrary unit), **(c)** $t = 20$ (a.u.), **(d)** $t = 42$ (a.u.).

Bloch equations offer a simple description of the basic OPM principle and can be well visualized. However, they are only valid for two-level systems and cannot describe fundamental effects like noise contribution due to spin exchange (relaxation), since only the collective spin is considered. This motivates the density matrix formalism, where

the population of each energy (sub)level is modeled, which will be described in the next sections.

2.5.3 Alkali atoms: ^{87}Rb and Cs

Commonly used atoms in OPM are the alkali atoms rubidium and cesium. The reason for using alkali atoms in OPM rather than other atoms is because of their single valence electron, which is optically probed.

^{87}Rb : In its natural abundance, rubidium consists mainly of the two isotopes ^{85}Rb and ^{87}Rb . While in theory both isotopes (and even a mixture) can be used for optical magnetometry, this work focuses on ^{87}Rb as it is used by commercially available OPM from QuSpin and Twinleaf. The D₁ line represents the transition from $5^2\text{S}_{1/2}$ to $5^2\text{P}_{1/2}$, while the D₂ line represents the transition from $5^2\text{S}_{1/2}$ to $5^2\text{P}_{3/2}$. The D₁ line energy difference is about $h/795\text{ nm}$, while the D₂ line energy difference is about $h/780\text{ nm}$, where h is the Planck constant. The excited states have a lifetime of $<30\text{ ns}$ [Ste01]. The $5^2\text{S}_{1/2}$ ground state energy level is split into two hyperfine levels with $F = 1$ and $F = 2$, and each hyperfine level has $2F + 1$ magnetic sublevels (Zeeman splitting) (Figure 2.7). The other states are split analogous.

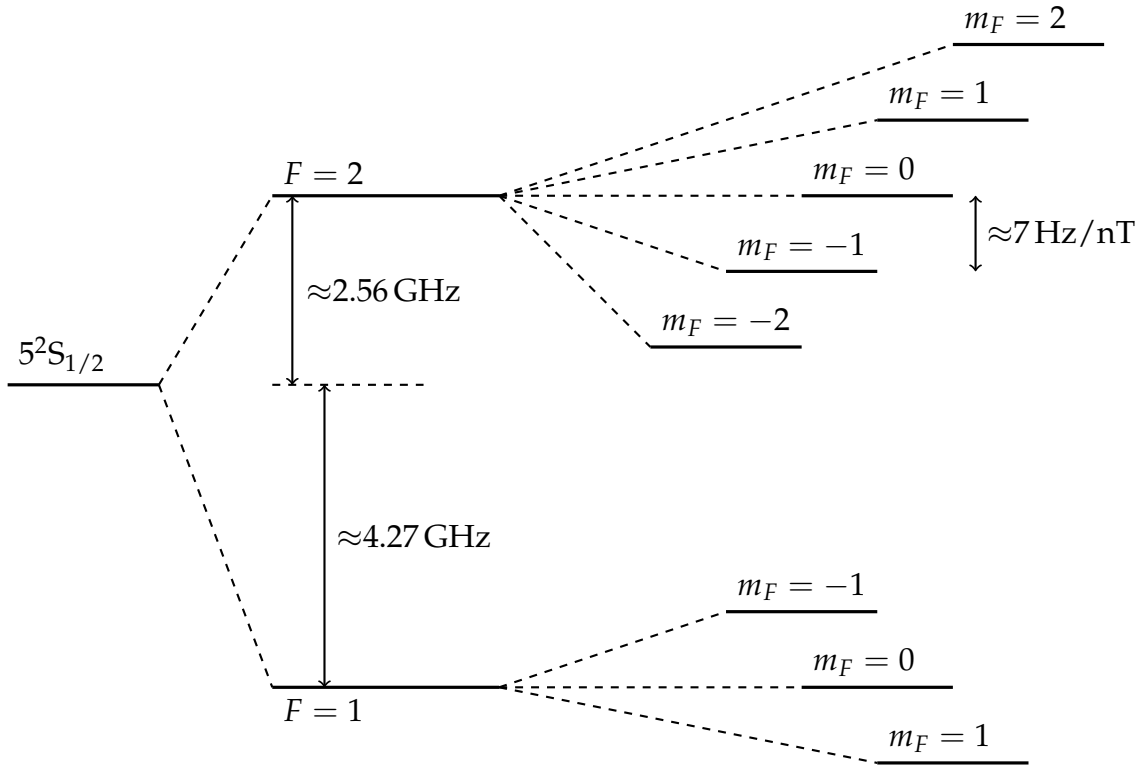


Figure 2.7: ^{87}Rb ground state hyperfine structure and Zeeman substates. Not to scale.

An external magnetic field B parallel to the (orbital \vec{L} , spin \vec{S} and total nuclear \vec{J}) angular momentum causes an energy shift of the sublevels. The energy splitting and corresponding frequency f (of any alkali metal's) ground state can be calculated using the Breit-Rabi formula [Bre31, Cor78, Ste01]:

$$f = \frac{-\Delta W}{2(2I+1)} + \frac{\mu_B g_I m_F B}{h} \pm \frac{-\Delta W}{2} \sqrt{1 + \frac{2m_F x}{I + \frac{1}{2}} + x^2} \quad (2.16)$$

with

$$g_J = g_l \frac{J(J+1) + L(L+1) - S(S+1)}{2J(J+1)} + g_s \frac{J(J+1) - L(L+1) + S(S+1)}{2J(J+1)}, \quad (2.17)$$

$$x = \mu_B B \frac{(g_J - g_I)}{h\Delta W}, \quad (2.18)$$

where μ_B is the Bohr magneton, h is the Planck constant and ΔW is the zero field hyperfine separation. For ^{87}Rb ground state, the spin angular momentum $S = 1/2$, the orbital angular momentum $L = 0$, resulting in $J = 1/2$. Still for the ground state $I = 3/2$, resulting in $F = 1$ and $F = 2$. The magnetic quantum number $m_F = \{-2, -1, 0, 1, 2\}$ for $F = I + J = 2$ or $m_F = \{-1, 0, 1\}$ for $F = |J - I| = 1$. The g -factors for ^{87}Rb are reported in literature [Ste01, Moh00, Ari77].

With no field applied, $F = 1$ and $F = 2$ differ by ≈ 6.8 GHz [Ste01]. When applying a field of $B = 50 \mu\text{T}$, the sublevels split by approx. 350 kHz (Figure 2.8). The sublevels are not split by exactly the same frequency, leading to beat notes at about 36 Hz, 72 Hz, 108 Hz and 1.4 kHz, as calculated using the Breit-Rabi formula (for $B = 50 \mu\text{T}$).

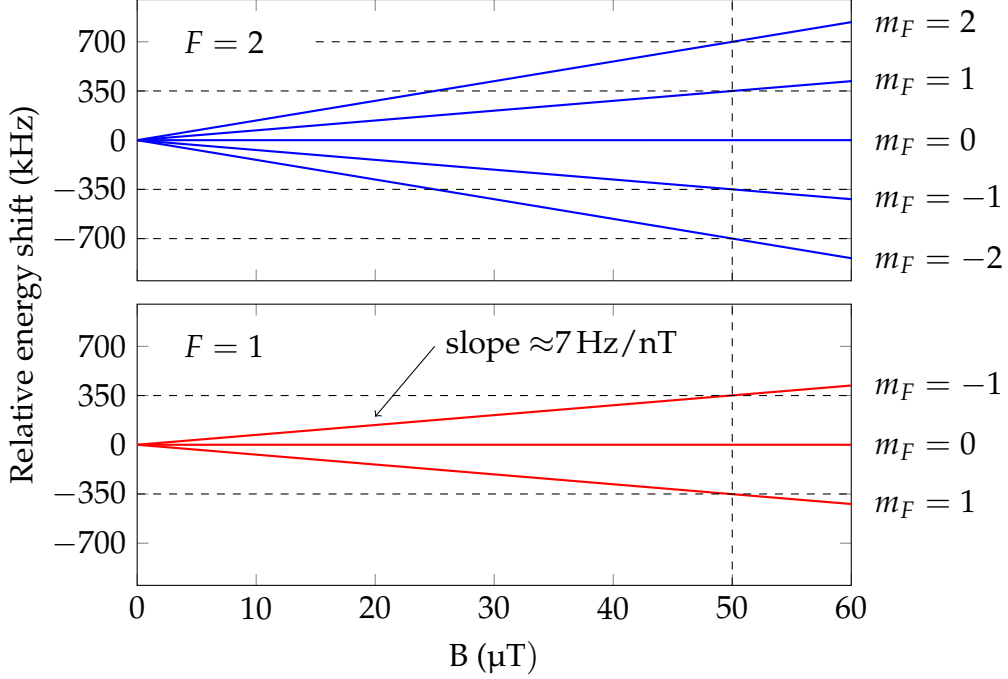


Figure 2.8: ^{87}Rb ground state hyperfine splitting energy shifts with respect to the applied magnetic field. The data points of the plot were calculated using the Breit-Rabi formula (Equation 2.16).

Cs: In contrast to rubidium, cesium has only one stable isotope. Further, a smaller temperature is needed for reaching the optimal atomic density for OPM operation, enabling even sensitive operation at room temperature, which might be useful for several biomedical applications. When compared to rubidium, cesium reacts less with glass cell walls (at the optimal operating temperature), leading to longer-living sensors [Sch15a].

2.5.4 Optical pumping, interaction with magnetic fields and optical probing

The Bloch equation model of an OPM is very easy to understand, however it lacks a lot of details, which are important for the operation of an OPM. Generally, Bloch equations are well suited to describe two-level quantum systems. A more profound approach is to model the quantum system by describing the energy levels and probabilities of the population occupying these levels. Formally, this is called the density matrix approach, where the diagonal elements of the density matrix represent the populations of the states, while the non-diagonal elements describe the coupling of the states. The time evolution of the system can then be estimated by solving a differential equation, the von Neumann equation, which is derived from the Schrödinger equation.

In this section, optical pumping, the interaction with magnetic fields and optical probing of ^{87}Rb will be described using the energy level structure. For an introduction and profound details of the density matrix formalism see [Sch15a, Roc10, Auz10].

Optical pumping

Without any external magnetic or electric fields (light) applied, all atoms will be in the ground state. It can be assumed, that all ground state levels are evenly populated, as visualized in Figure 2.9a. If light with a suitable wavelength, e.g., 795 nm for the ^{87}Rb D_1 transition, is shined onto an atom, the atom will absorb the photon. The photon's spin is also transferred to the atom. In the case of circularly polarized light σ^+ or σ^- , $\Delta m_F = \pm 1$. In the case of linearly polarized light, which is a superposition of σ^+ and σ^- , $\Delta m_F = 0$ [Cor78]. After a few nanoseconds, the atoms relax via spontaneous emission. Here, $\Delta m_F = 0, \pm 1$. As a result, the atoms are transferred towards the $F = 2, m_F = 2$ state when using σ^+ light. This state is also called dark state. This process is visualized in Figure 2.9b. As a side note it should be mentioned, that the hereby emitted photon is possibly re-absorbed by another atom (radiation trapping), which is usually undesired. In an OPM setup, this would translate to an increased noise, and is prevented by adding a quenching gas [Ros07, Rom10].

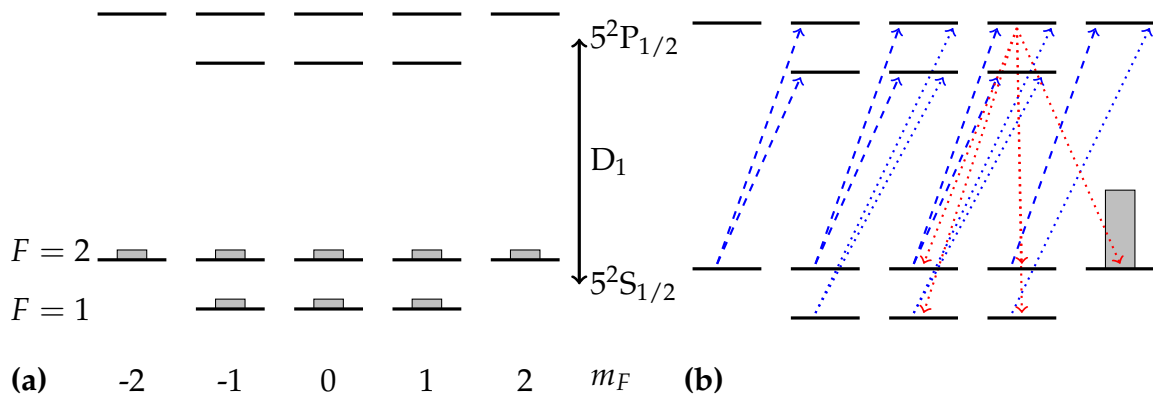


Figure 2.9: **(a)** Energy probability distribution of a cloud of ^{87}Rb atoms at zero magnetic field and without any electric field (light) applied. **(b)** D_1 optical pumping with σ^+ light (blue). The pump laser linewidth is broad, so $F = 1$ and $F = 2$ are pumped. The relaxation via spontaneous emission (red) is indicated for one excited sublevel only. The atoms are pumped towards $F = 2, m_F = 2$.

Interaction with magnetic fields

If no magnetic field is applied, the sublevels along m_F are degenerated (Figure 2.9). A magnetic field parallel to the pump beam's wave vector splits the magnetic sublevels (Figure 2.10a), like discussed before. The splitting is about $\approx 7 \text{ Hz/nT}$ for ^{87}Rb . A magnetic field perpendicular to the pump beam's wave vector couples the sublevels (Figure 2.10b). The total precession frequency is defined by the total magnetic field applied.

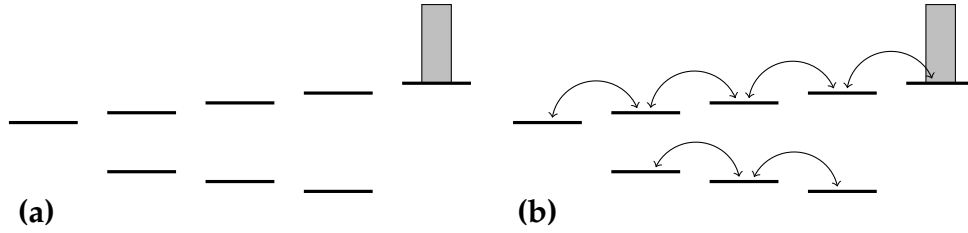


Figure 2.10: **(a)** Ground state energy levels split due to a magnetic field applied parallel to the quantization axis. **(b)** In addition to the parallel magnetic field, a field perpendicular to the quantization axis is applied, which couples the different energy levels.

Optical probing

In order to measure the magnetic field, the described interplay of atoms and optical pumping and magnetic field interaction needs to be monitored. Like mentioned before, different properties of the atoms can be probed. One possibility is called optically induced transparency, where the transmitted power of the pump probe is monitored using a photodiode. In the idealized case of a fully polarized atomic ensemble, where all atoms were transferred to a dark state, no more photons can be absorbed. The ensemble is therefore optically transparent and the photodiode measures a maximum intensity. As discussed, a magnetic field couples different sublevels, draining the dark state. Hence, these atoms can be polarized again by absorption and a followed scattered emission of photons. The transmitted light intensity measured by the photodiode was lowered. This method of optical probing is exploited by the commercially available zero field magnetometers from QuSpin, which are discussed in more detail in Section 2.6.2.

Another method of optical probing is to use a linearly polarized probe laser and a polarimeter as detector. This technique is often called polarization method or Faraday rotation method. Depending on the atomic state, the polarization of the light is rotated, allowing for monitoring a projection of the spin, referring to the Bloch equation model. Which detection scheme to prefer drastically depends on the geometrical properties of the OPM (number of lasers used, direction of lasers and magnetic field) and cost [Bud07].

2.6 Selected OPM operation modes

2.6.1 Introduction

To achieve a high sensitivity of the magnetometer, several techniques are well known. Spin exchange relaxation free (SERF) magnetometers are operated at very low background magnetic fields in the sub-nanotesla region, to prevent the largest source of noise, namely the spin exchange relaxation. In intensity modulated (IM) magnetometers, the spin precession is driven on resonance at the Larmor frequency. Another method to prevent spin exchange relaxation is to fully polarize the atoms as in free-spin-precession (FSP) magnetometers.

2.6.2 Spin Exchange Relaxation Free (SERF) magnetometer

To achieve femtotesla sensitivities at low frequencies (sub-kHz), spin exchange relaxation needs to be suppressed. In order to reduce spin exchange, one possibility is to use vapor cells with low atomic densities. A lower density results in a lower number of atom collisions per time and hence a lower spin exchange relaxation. However, large vapor cells with diameters in the range of tens of cm are required for sensitive OPM [Ale95, Bud00], limiting the practical application. Another method, discovered by [Hap73], is to drastically increase the spin exchange rate. The idea is, that due to the high number of collisions, the spin precession after each collision is averaged and thus eliminated. The condition is a low background magnetic field. At zero background field, the laser pumps nearly all the atoms into a dark state and the cell becomes nearly transparent for the laser light. If a weak magnetic field is applied perpendicular to the pump light's wave vector \vec{k} , some of the atoms in the dark state are redistributed to other states. Now a part of the laser light gets absorbed by the atoms and they are again transferred to the dark state via spontaneous decay of the excited state. An equilibrium of redistribution and repumping will settle, resulting in a reduction of the transmitted light through the cell. The transmitted light is monitored by a photodiode. The relation between the applied field and the transmitted light intensity is described by a Lorentzian function (see blue trace in Figure 2.17) [DR69b]. Alternatively, the operation principle can be explained by using the Bloch equations (see Section 2.5.2). The spins are polarized using a circularly polarized pump laser (Figure 2.5b). If no magnetic field is applied, the atomic vapor gets maximally transparent. A magnetic field perpendicular to the polarization acts like a momentum and tilts the polarization (Figure 2.5c), which is counteracted by the still running pump laser. Hence, less photons reach the photodiode detector. This setup (Figure 2.11b) is used by the QZFM sensors from QuSpin, with a few additions described in Section 2.6.6. A similar approach (Figure 2.11a) is used by Allred et al. [All02], which first demonstrated a $10 \text{ fT}/\sqrt{\text{Hz}}$ SERF magnetometer with a small vapor cell. The sensitivity was later improved to $\text{sub-fT}/\sqrt{\text{Hz}}$ [Kom03]. The difference to the previously described method is, that the polarization rotation of a linearly polarized, detuned probe laser is monitored instead of the transmission transmitted light. It should be noted, that SERF magnetometers belong to the group of Hanle or zero-field ground state level crossing magnetometers, introduced by [Leh].

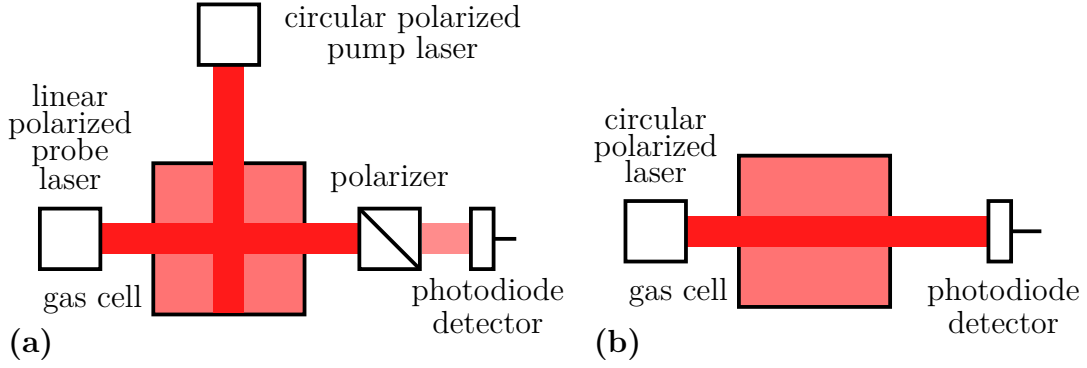


Figure 2.11: SERF OPM setups as used in [All02, Kom03] (a) and in the QuSpin QZFM sensors [Osb18] (b). Both setups also integrate a lock-in-amplifier together with an optical modulator or a magnetic modulation, which is not shown here.

To sum up, SERF magnetometers are the most sensitive OPM to date ($160 \text{ aT}/\sqrt{\text{Hz}}$ in a centimeter-sized cell [Dan10]), with the limitation of requiring almost zero magnetic field and magnetic field gradient for their operation. By applying a bias field along the pump-beam direction, the bandwidth of a few Hz can be increased [Kor07] to e.g., 135 Hz [Osb18] or more [Sav17].

A final caveat: The abbreviation SERF is used in literature and in this work for a magnetometer operating near zero magnetic field, thereby suppressing spin exchange relaxation. However, operating near zero field is not the only possibility to suppress spin exchange relaxation, which will be described in the next Sections. Those magnetometers are usually not denoted as SERF magnetometers.

2.6.3 Intensity Modulated (IM) magnetometer

Due to the small magnetic field applied in a SERF magnetometer, it can be considered as overdamped precession. If a larger magnetic field is applied, the spins do precess. However, two problems arise. First, the precessions are not coherent, meaning that each atomic spin is precessing on its own, since there is no process synchronizing them. Therefore no collective spin precession can be measured at all. The second problem is relaxation due to wall collisions and spin exchange, leading to a high amount of noise. One way to address the first problem is to modulate, i.e., synchronize the spin precessions. e.g., a small sinusoidal magnetic field can be applied to the OPM. The frequency must be tuned to the precession frequency. Such a magnetometer is also called ODMR (optically detected magnetic resonance) magnetometer in literature. First ODMR was demonstrated by Fermi et al. [Fer25] and Brossel et al. [Bro52]. An alternative to magnetic modulation is optical modulation, e.g., by chopping the pump laser, which was initially shown by Bell and Bloom [Bel61]. Even the pump laser frequency or polarization can be used for modulation [Gru13].

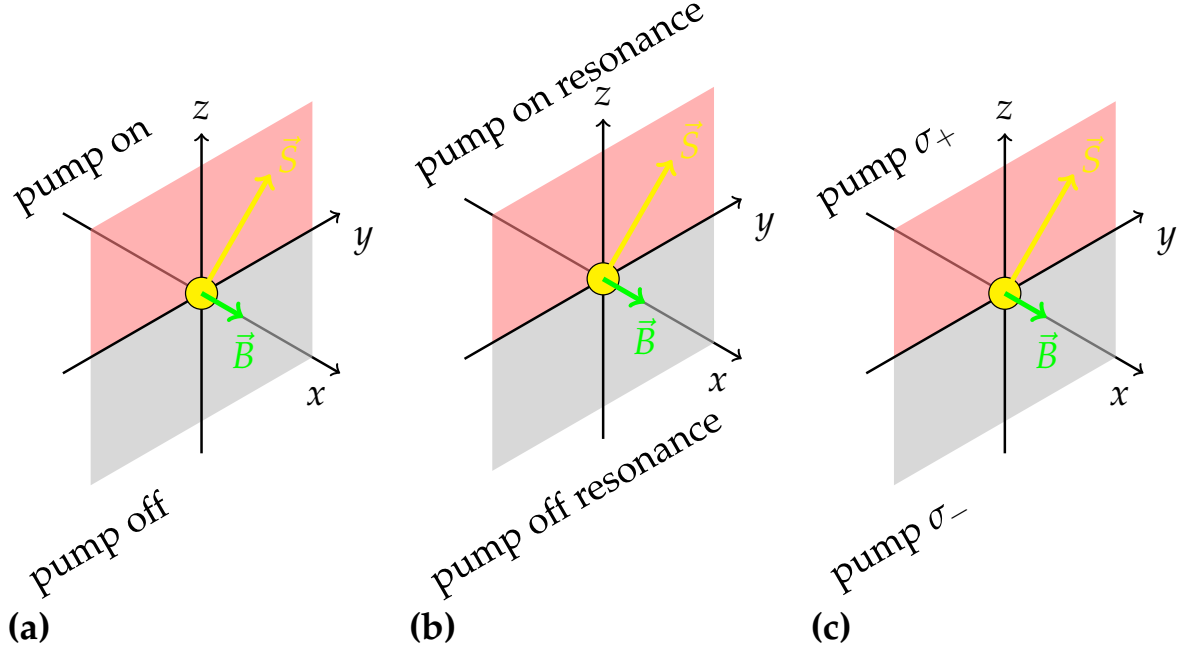


Figure 2.12: Spin polarization with amplitude modulated light (a), frequency modulated light (b) and polarization modulated light (c). Pump direction (\vec{k}) is \vec{z} . Figure based on [Wei17].

With this techniques, the first problem is solved and a collective spin can be monitored by monitoring light absorption or polarization rotation. Depending on whether the component perpendicular or parallel to the pump light (actually the pump light's wave vector \vec{k}) is probed, such OPM are called M_x or M_z magnetometers [Wei17].

To address the problem of wall relaxation, the vapor cells can be antirelaxation coated [Bud05] or the diffusion length of the atoms can be reduced by adding buffer gas [Hap72]. A solution to reduce spin exchange relaxation was presented by Scholtes et al. [Sch11, Sch16]. Usually, a narrow-band laser is used for optical pumping. In a Cs OPM, the laser is e.g., tuned to pump $F = 4$. The consequence is, that the $F = 4$ population is pumped to a dark state, like intended. However, a non-neglectable part of the atomic population will be distributed at sublevels of $F = 3$. They will not contribute to the measured signal, but instead cause spin exchange relaxation. If the pump light power would be increased and/or the pump laser would be made broader, more $F = 3$ population would be optically pumped and thus used. However, then the OPM would suffer from power broadening. A solution is to tune the pump laser to $F = 3$ instead of $F = 4$ and to increase the pump power. Therefore, $F = 3$ gets depleted and $F = 4$ is still pumped, while avoiding power broadening in $F = 4$. Since $F = 3$ is depleted, spin exchange relaxation is reduced and contemporaneous the whole population is contributing to the measured signal. Alternatively, two separate lasers can be used for pumping and repumping [Sch15b].

An exemplary OPM, where the pump light is on/off modulated to synchronize the spin

precession is depicted in Figure 2.13. Here, the pump laser transmission is measured. If the pumping frequency f_c is synchronized with the spin precession frequency f_L , the averaged transmission power is maximal (compare Figure 2.14a). To enhance the SNR, the photodiode signal is demodulated by a lock-in amplifier, which delivers a signal like shown in Figure 2.14b. The modulation frequency can either be kept stationary or fed back (see Section 2.6.5).

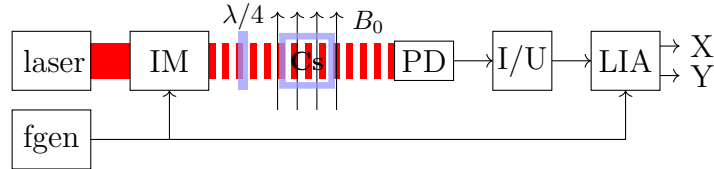


Figure 2.13: Schematic of an intensity modulated OPM configuration as used in [Sch12, Jau20b]. With a function generator (fgen) and intensity modulator (IM), the linearly polarized light from the laser is pulsed at the Larmor frequency of the alkali atoms and converted into circular polarization by a $\lambda/4$ waveplate. The transmitted laser light is detected by a photodiode (PD), amplified by a current voltage converter with integrated preamplifier (I/U) and phase-sensitively demodulated with a lock-in amplifier (LIA).

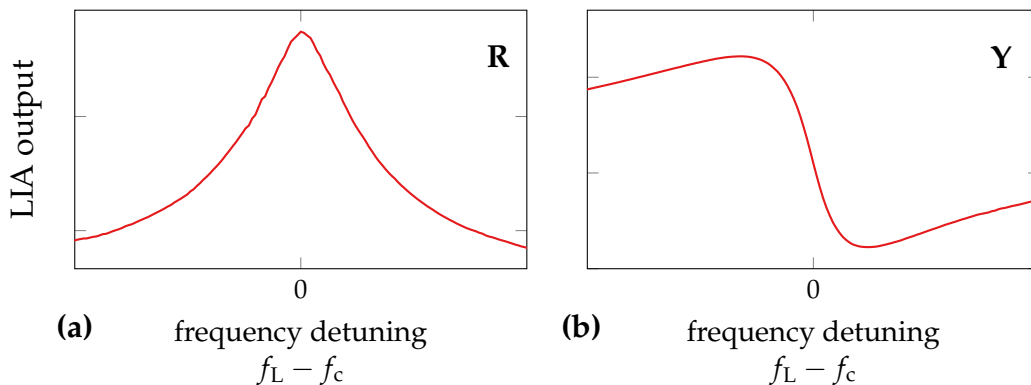


Figure 2.14: OPM resonances. (a) Magnitude (R) and (b) quadrature component (Y), as acquired with a lock-in amplifier.

2.6.4 Free-Spin-Precession (FSP) magnetometer

In Free-Spin-Precession (FSP) magnetometers, the spin ensemble is not continuously, or resonantly pumped. Instead, the atoms are polarized in one time interval, while probed in another interval. This leads to several advantages of these types of magnetometers. First of all, the magnetic field measurements are based on frequency counting, instead of a voltage or current measurement. Frequency counting offers an enormous dynamic range, which is hard to meet with analog-to-digital converters. Since the amplitude of the so-measured magnetic field is independent of the signal amplitude, there is no strict

need in balancing cell properties of magnetometer arrays. Obviously, the noise performance depends strongly on the signal amplitude. The precession measurement does not require any feedback like needed in resonantly pumped OPM. This eliminates instability issues, which can be found when applying high gain feedback loops for increased sensor bandwidth. Further, since there is in principle no need for lock-in-amplifiers, this operation mode would be well suited for a camera-like OPM, where the readout is a major challenge. The bandwidth of a FSP magnetometer will be discussed in Section 7.2, with the result of an instantaneous system response. The advantages of pulsed pumping are no pump noise and no lightshift of the pump laser, leaving only the effects of the comparatively low probe laser. Even this influence can be eliminated, making an FSP OPM an ideal candidate for accurate magnetic field measurements [Hun22].

In contrast to all the mentioned advantages, the separation in time of pumping and probing has one important disadvantage, namely the non-continuous readout of the magnetic field. In principle, a standard pump-probe-setup can be used to implement a FSP magnetometer (Figure 2.15).

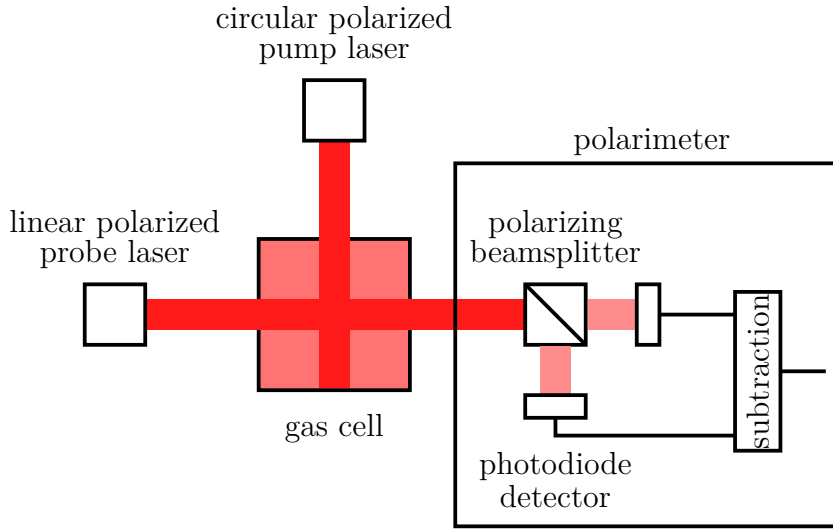


Figure 2.15: Schematic of a standard pump-probe-setup, which can be configured as a free-spin-precession magnetometer.

After polarizing the atoms, the pump laser is switched-off and the precession is monitored by a probe laser, which shines onto a polarimeter after passing the vapor cell.

A pure sinewave-like precession with a constant frequency and amplitude is expected in an idealized case, when only a DC-field is applied and no spin destruction takes place:

$$y(t) = A \cos(2\pi ft + \varphi_0) = A \cos(\gamma B_0 t + \varphi_0) = A \cos(\gamma B_0(t - t_0)), \quad (2.19)$$

with the time t , the initial amplitude A , the gyromagnetic ratio γ , the precession frequency f , the applied magnetic field B_0 and the arbitrary initial phase φ_0 . In a real magnetometer, spin destruction will lead to a decay of the detected relaxation amplitude. The parameters of this decay depend on the applied magnetic field, e.g., a stronger field

leads to a faster spin destruction. Stray light or analog amplifiers in the system might generate a signal offset O . The precession signal can be modeled as:

$$y(t) = Ae^{-t/\beta} \cos(2\pi f(t - t_0)) + O = Ae^{-t/\beta} \cos(\gamma B_0(t - t_0)) + O, \quad (2.20)$$

with the damping parameter β . In many practical applications, it is desired to measure time-varying magnetic fields. The magnetic fields modulate the frequency of the precession. Therefore a frequency demodulation has to be carried out. Further, β will be a function of time, depending on the history of the magnetic field since the last pump pulse.

$$y(t) = Ae^{-t/\beta} \cos\left(\omega_0 \cdot t + \varphi_0 + \gamma \int_0^t B(\tilde{t}) d\tilde{t}\right) + O = Ae^{-t/\beta} \cos(\varphi(t)) + O \quad (2.21)$$

The instantaneous frequency is defined as the derivative of the instantaneous phase $\varphi(t)$:

$$f_{\text{inst}}(t) = \frac{1}{2\pi} \frac{d\varphi(t)}{dt} = \frac{\gamma}{2\pi} (B_0 + B(t)). \quad (2.22)$$

If the frequency of the magnetic field to be measured changes slowly compared to the precession frequency, an average precession frequency might be extracted from the photodiode signal. Possible methods include zero crossing detection and curve fitting [Gru15]. Alternatively, high frequency information about the magnetic field can be extracted e.g., using Hilbert Transform [Wil20], while the Nyquist theorem still needs to be satisfied. Further details will be elaborated in Section 7.2.2.

2.6.5 Feedback-controlled OPM

Feedback control of an OPM shouldn't be considered as a separate operation mode. Instead, nearly any OPM might be operated in a closed loop mode, with the advantage of increasing the magnetometer bandwidth. A bandwidth increase up to 1.8 kHz while maintaining a sensitivity of 20 fT/ $\sqrt{\text{Hz}}$ has been demonstrated for SERF magnetometers [Tan21b]. A nonlinear magneto-optical rotation (NMOR) magnetometer has been tuned to a bandwidth of 1 kHz [Sch05]. Even 56 kHz bandwidth could be achieved with a M_x type OPM [Leb20]. Mostly, the bandwidth of such magnetometers is solely technically limited by the instrumentation of the feedback loop [Ale92, Leb20]. Besides, the key lies in the design of the feedback loop to keep the magnetometer stable [Leb20]. Finally it should be stated that bandwidth must be traded off with sensitivity [Sch05, Jau21]. For higher frequencies, a pickup-coil might be a reasonable choice [Tum07].

2.6.6 Vectorizing a scalar OPM

A scalar OPM, like the SERF magnetometer, has the drawback that no vectorial information about the magnetic field is obtained. A magnetic field modulation technique can be applied to extract directional information.

A SERF magnetometer is considered first. Like stated before, the relation of the applied field and the transmitted light intensity is a Lorentzian function (blue trace in Figure 2.17). In a first simplified case it is assumed, that the direction of the field to be measured is known, but not the orientation, i.e., a 1D case is assumed. The amplitude of the magnetic field can be extracted from the transmitted light intensity. As it can be seen in the blue trace in Figure 2.17, the lineshape is symmetrical, not allowing for the estimation of the orientation of the applied field. To overcome this limit, a small magnetic field with the same direction can be applied and the change in transmitted light intensity can be monitored. This allows estimating the orientation of the field to be measured.

In a practical realization (see Figure 2.16), a lock-in amplifier (LIA) can be exploited. Here, the magnetic field is modulated and in-phase detected, leading to an output signal in the form of the derivative of the Lorentzian (red trace in Figure 2.17). In literature, it is also called the dispersive signal [Sch12]. To understand the process of lock-in detection, a simple example is presented.

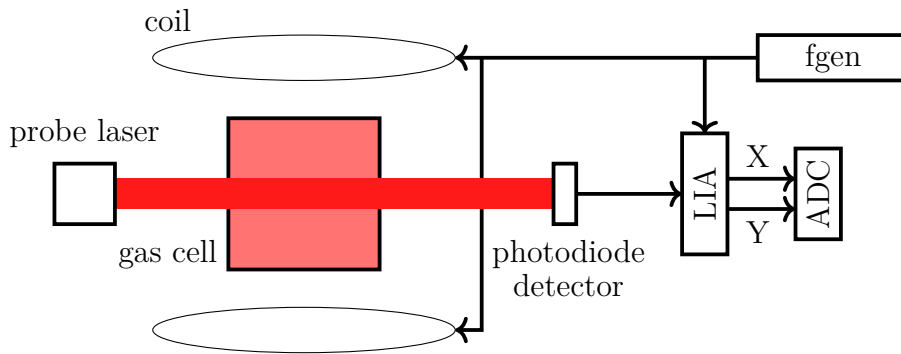


Figure 2.16: Vectorization of a scalar magnetometer using a lock-in-amplifier.

The external magnetic field $B(t)$ (which is to be measured) is modulated, i.e., a sinusoidal signal with known angular frequency ω_m and constant, not necessarily known amplitude B_1 is superimposed. Therefore, the magnetic field seen by the magnetometer is

$$B_{\text{mag}}(t) = B(t) + B_1 \cdot \sin(\omega_m t). \quad (2.23)$$

In a simple case and without loss of generality, the Lorentzian absorption transfer function of the magnetometer is approximated by an arbitrary quadratic function a (with $|B_{\text{mag}}| < 2$):

$$a(B_{\text{mag}}(t)) = -B_{\text{mag}}^2(t) + 4 \quad (2.24)$$

$$= -B^2(t) - B(t)B_1 \sin(\omega_m t) - B_1^2 \sin^2(\omega_m t) + 4. \quad (2.25)$$

$a(B_{\text{mag}}(t))$ is the output of the OPM's photodiode, which is fed into the LIA, together with the reference signal $\sin(\omega_m t)$. The LIA performs a mathematical multiplication of

both signals using a product mixer:

$$a(B_{\text{mag}}(t)) \sin(\omega_m t) = \left[-B^2(t) - B(t)B_1 \sin(\omega_m t) - B_1^2 \sin^2(\omega_m t) + 4 \right] \sin(\omega_m t) \quad (2.26)$$

$$= -B^2(t) \sin(\omega_m t) - B(t)B_1 \sin^2(\omega_m t) - B_1^2 \sin^3(\omega_m t) + 4 \sin(\omega_m t). \quad (2.27)$$

With

$$\sin^2(\omega_m t) = \frac{1}{2} (1 - \cos(2\omega_m t)), \quad (2.28)$$

Equation 2.26 leads to

$$-B^2(t) \sin(\omega_m t) - \left[\frac{1}{2} B(t)B_1 - \frac{1}{2} B(t)B_1 \cos(2\omega_m t) \right] - B_1^2 \sin^3(\omega_m t) + 4 \sin(\omega_m t), \quad (2.29)$$

which is lowpass filtered (with a filter stop frequency smaller than ω_m), leaving only $-\frac{1}{2}B(t)B_1$, which is the output of the lock-in amplifier, which corresponds to the cross correlation between input signal and reference signal. To conclude, the sign of $B(t)$ is recovered, which was not available in the pure photodiode signal (see e.g. Equation 2.25). In Figure 2.17 this steps are repeated for a Lorentzian waveform (blue trace). The obtained dispersive signal is shown in red. It should be noted, that an OPM is usually operated in the linear region of the dispersive signal. An interesting fact is, that the LIA also reduces the $1/f$ noise of the signal of interest [Kas73], which often dominates low frequency measurements. Like the name says, $1/f$ noise decreases with increased frequency. Therefore it would be beneficial for the signal of interest to lie in the high frequency range. However, e.g., the absorptive signal of interest of a classical SREF magnetometer covers the frequency band from DC to about 100 Hz. To transfer the signal to a higher frequency range, it can be externally modulated, e.g., by modulating the laser or the magnetic field (which was described above). The modulated signal can then be synchronously detected (demodulated) by the LIA [Li06].

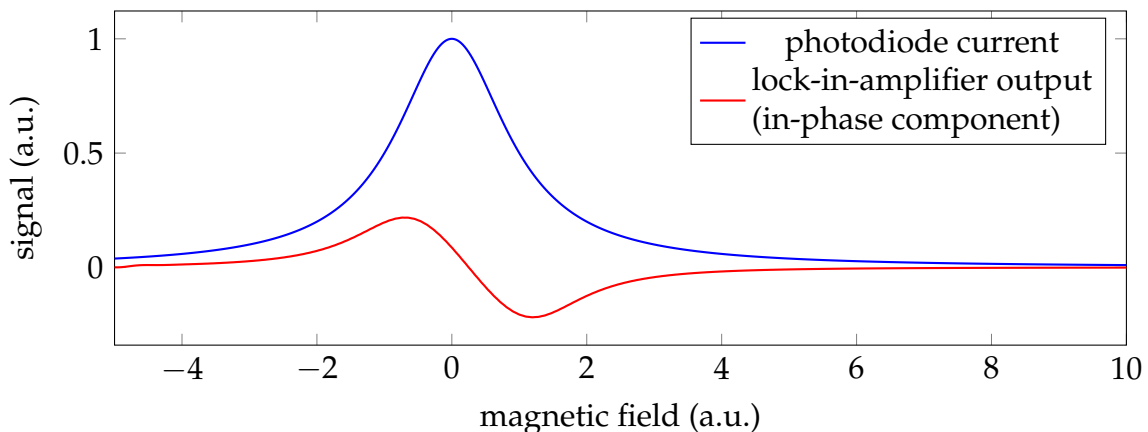


Figure 2.17: Simulation of the lock-in amplifier response (red) to a Lorentzian magnetometer transfer function (blue).

The presented steps can be repeated for a vectorial system, demonstrating that the direction of the applied modulation field determines the projection axis of the field to be measured:

$$\vec{B}_{\text{mag}}(t) = \begin{pmatrix} B_x(t) + B_1 \sin(\omega_m t) \\ B_y(t) \\ B_z(t) \end{pmatrix} \quad (2.30)$$

$$a(\vec{B}_{\text{mag}}(t)) = -(B_x(t) + B_1 \sin(\omega_m t))^2 - B_y^2(t) - B_z^2(t) + 4 \quad (2.31)$$

$$\text{LP-filter} [a(\vec{B}_{\text{mag}}(t)) \sin(\omega_m t)] = -\frac{1}{2} B_x(t) B_1. \quad (2.32)$$

In order to extend this principle to a second axis (while both axis are perpendicular to the light beam, i.e., both axis lie in the sensitive plane of the magnetometer), a second modulation field can be applied. To distinguish between them, different frequencies of the modulation signals, or a 90° phase shift between them can be selected. The commercially available SERF OPM (QZFM) by QuSpin (QuSpin Inc., Louisville, Colorado, USA) operates on this principle, allowing for measurement of two vectorial components of the applied magnetic field [Osb18].

In case of a scalar magnetometer operated at a background magnetic field \vec{B}_0 , several other methods for vectorization are presented in literature: In the simplest case, if the background field \vec{B}_0 is large compared to the signal of interest \vec{B} , the magnetometer can be assumed as a vectorial sensor with its sensitive direction along the background field [Zhe20]. This is simply explained by considering Equation (2.33):

$$|\vec{B}_{\text{mag}}| = B_{\text{mag}} = \sqrt{(B_0 + B_{\parallel})^2 + B_{\perp}^2}, \quad (2.33)$$

where $|\vec{B}_{\text{mag}}|$ is the output of the scalar magnetometer, and B_{\parallel} resp. B_{\perp} is the component of \vec{B} parallel resp. perpendicular to \vec{B}_0 . It is obvious, that in the case $B_{\perp} \ll (B_0 + B_{\parallel})$ or $|B| \ll B_0$ it follows that $|\vec{B}_{\text{mag}}| \approx B_0 + B_{\parallel}$. The prerequisite for using this method is, that the direction of B_0 needs to be known.

A not very popular, but promising way of obtaining vectorial information is by applying a rotating magnetic field to the magnetometer. In this case, several systematic effects need to be considered [Wan20].

The magnitude and one of the polar angles of the magnetic field can be extracted from an OPM in Bell-Bloom-configuration, by investigating not only the AC component of the probe signal, but also the DC signal [Zha21]. Further, in a free-spin-precession magnetometer, the amplitude ratio of the signal at Larmor frequency and its first harmonic can be exploited to extract one polar angle of the field [Len14, Lee21]. When combining both techniques, full vectorial information can be obtained, as it was shown using a Double-Resonance magnetometer [Ing18].

Alternatively, if the spins of an OPM are readout with multiple probe lasers, i.e., if multiple projections are measured, complete vectorial information can be reconstructed [Afa15].

3 State of the art

3.1 Optically pumped magnetometers: sensitivity and other parameters with respect to MRX(I)

OPM have a long history, dating back to the work of [Kas50a, Bel57, Bel61, DR69b, Kas73, Hap73] and others. Later work improved their sensitivity to the level of SQUID [Bud00, Kom03], which enabled their use in biomedical applications [Sha13, Kna16]. OPM proved to be especially advantageous for magnetoencephalography (MEG) [Mar22], allowing small sensor-target distances [Iiv17] and patient movements during measurements [Bot18]. Over the last years, several OPM were commercialized, targeting mainly MEG and geophysical applications. Generally, for MRX(I), a high sensitivity, low sensing volume, wide bandwidth, short dead time and a possibly high immunity against magnetic field pulses are desired. Since these requirements partially match the ones for MEG and geophysical applications, MRX(I) benefits from the developments and commercialization of OPM for these fields.

Various total field OPM from Gem Systems, Geometrics and Scintrex are commercially available with sensitivities ranging from about $200 \text{ fT}/\sqrt{\text{Hz}}$ to about $25 \text{ pT}/\sqrt{\text{Hz}}$. These magnetometers are mostly intended for geophysical applications and offer a bandwidth of $\leq 10 \text{ Hz}$ [Oel20]. Due to the low bandwidth, these sensors are not considered in this work. Three other companies, namely QuSpin, Twinleaf and Fieldline sell research grade OPM. The parameters of the available sensors are summarized in Table 3.1.

Table 3.1: Summary of commercially available, research grade OPM. Values reported here are taken from the manufacturer’s datasheet or homepage.

company	sensor	noise ($\text{pT}/\sqrt{\text{Hz}}$)	bandwidth (Hz)	dynamic range (nT)	operation mode
QuSpin	QTFM	< 1	100	$1\text{e}3 - 100\text{e}3$	Mz
Twinleaf	microSAM	20	100	$1\text{e}3 - 100\text{e}3$	Mz
Twinleaf	OMG	< 0.2	1000	$1\text{e}3 - 100\text{e}3$	FSP
QuSpin	QZFM Gen-3	< 0.015	135	± 5	SERF
Twinleaf	microSERF	< 0.03	150	± 10	SERF

QTFM, microSAM and OMG are scalar magnetometers, while QZFM and microSERF provide vectorial field information. In addition to the sensors listed above, Fieldline lately started selling their SERF magnetometers. While no official specifications are available,

similar specifications as the QZFM or microSERF can be expected. A major difference expected from the Fieldline sensors is the possibility of an active field compensation, thus enabling slight movements of the sensors in moderately shielded environments. However this has not been published yet. All the sensors summarized in Table 3.1 employ miniaturized vapor cells and are therefore operating with a low sensing volume. It should be noted, that the sensor dead time after applying magnetic field pulses is not vendor-specified and only reported in literature for the QZFM [Baf19].

The best sensitivities reported in literature are $160 \text{ aT}/\sqrt{\text{Hz}}$ for a gradiometric potassium SERF OPM with a bandwidth of several Hz [Dan10] and $540 \text{ aT}/\sqrt{\text{Hz}}$ for a gradiometric rubidium total field OPM employing two 42-pass vapor cells, achieving a bandwidth of 60 Hz [She13]. It should be noted, that these sensitivities were realized using large (cm^3 scale) sensing volumes under idealized conditions, especially at low background magnetic field gradients. In terms of high channel count, a setup with 432 SERF OPM channels was demonstrated for magnetoencephalography [Pra21].

3.2 Magnetorelaxometry using different magnetometers

To date, MRX of MNP has been demonstrated using various magnetometers, e.g., using fluxgate magnetometers [Lud05b, Lud09], SQUID [Cha83, Köt95, Lan02, Jur06, Wie12a], OPM [Kna10, Joh12, Dol15, Baf19], giant magnetoresistive sensors (GMR) [Den10], nitrogen-vacancies (NV) [SL15, Kuw20] and hall-effect-sensors (HE) [Liu11, Das21]. MRX setups in literature exhibit very different properties in terms of geometry, like sample volume, sensor volume, and especially sample-to-sensor-distance. Further, excitation field, excitation method (e.g., in-place or remote magnetization), sensor noise and especially the properties of the MNP samples used during the experiment contribute significantly to MRX parameters like mass detection limit and detectable diameter distribution. It is therefore hard to compare MRX setups. However, to get an overview of the state of the art experiments, a few values are reported here.

Generally, it can be stated that SQUID-MRX is among the most sensitive ones. In [Wie12a], a 200 ng iron detection limit was reached for a 150 μL sample. A SQUID noise level of $1.5 \text{ fT}/\sqrt{\text{Hz}}$ was reported. For an excitation field of up to 4 mT, dead times in the range of 200 μs to 400 μs were reached. Depending on the MNP type, the data sampling rate was selected between 250 Hz and 1 MHz.

In [Lud05a], a fluxgate with a noise level of $3 \text{ pT}/\sqrt{\text{Hz}}$ was investigated for MRX. With a selected bandwidth of 3 kHz and an excitation field of 0.72 mT, 1 μmol of iron was detected after averaging for 50 times. This corresponds to an iron amount of 55 μg .

First proof of concept MRX measurements with OPM were performed by Knappe et al. [Kna10], where the focus relied on general OPM development. Later, Dolgovskiy et al. [Dol15] investigating particle size effects of immobilized samples. In 2019, Baffa et al. [Baf19] published first results of OPM-MRX using a commercially available QZFM OPM (generation 1). In [Baf19], a system noise level of $30 \text{ fT}/\sqrt{\text{Hz}}$ and an excitation field of up to 9 mT was indicated. The iron detection limit was reported to be a few μg (not exactly specified), while for other MNP measured with the same setup, the detec-

tion limit is 50 times worse. This confirms our statement, that the iron detection limit of OPM must not be chosen as sole parameter for comparison of different MRX systems. With respect to hall-effect-sensors, Das et al. [Das21] demonstrated a 1.6 mg/mL iron detection limit for a sample volume of 14 μ L. This corresponds to an iron amount of 22.6 μ g. Unfortunately, neither the sensor noise, nor the excitation field, nor the sensor-sample distance are reported. A striking 64 ns dead time was demonstrated using a hall effect sensor, even though applying a 3 mT excitation field [Liu11].

It should be highlighted, that NV offer very close proximity to the MNP target. For example, the magnetization of single MNP was studied in [SL15].

To sum up, SQUID offer very high sensitivity, high bandwidth, low dead time and cm scale sensor-target-distances, while requiring cryogenic cooling. This qualifies them as reference technique in MRX(I). Fluxgates, GMR, NV and HE exhibit very high noise compared to SQUID. Therefore, on the one hand, these sensors might not be well suited for MRXI. On the other hand, they potentially offer close proximity to the MNP target, being of interest for very specific MRX applications.

As SQUID can be considered the state of the art magnetometers for MRX(I), it is important, that their limitations are well understood. In MRX(I), pulsed fields in the millitesla region are applied to the MNP and therefore also to closeby magnetometers. This leads to several problems in SQUID. First, the FLL electronics needs to be fast enough to track the steep magnetic field changes, while still being stable. This is possible with state of the art FLL electronics [Sch09]. However, the dynamic range of the integrator within the FLL is mostly limited to a few nT [Kob11]. This requires to reset the integrator after having applied the field pulse [Lie16, Dru07]. The second issue is called flux trapping. If magnetic fields in the mT region are applied to a SQUID, magnetic flux will be stored i.e., trapped inside the superconducting loop, making the sensor unusable. In order to remove trapped flux, the SQUID needs to be heated above the critical temperature, or it needs to be degaussed e.g., using decaying AC magnetic fields [Mat17, Sto16]. In order to avoid flux trapping, the SQUID might be surrounded by a superconducting shield, while feeding the flux through a flux transformer with an integrated current limiter [Sto16, AD18]. A general drawback of SQUID with respect to other magnetometer types is the need for liquid helium or liquid nitrogen for cooling the sensor below the critical temperature, being expensive and requiring a special infrastructure. Further, the thermal insulation (dewar) limits the target-sensor-distance. The dewar also prevents flexible positioning of the single sensors, and as the SQUID loops always need to be submerged in liquid helium, only measurements *from above* are feasible.

Like elaborated before, OPM with sensitivities comparable to those of SQUID were demonstrated in literature. This motivates the investigation of OPM for MRX(I), potentially offering several advantages over established magnetometers.

3.3 Magnetorelaxometry imaging: experiments in literature

In order to obtain quantitative spatial information about an MNP distribution, the target region is exposed to spatially different pulsed excitation fields and the relaxation signals are measured. The extracted relaxation parameters are then used to solve an (ill-posed) inverse problem like described in Section 2.3. In the case of a small sensor-target-distance it might be sufficient to apply a scanning approach while omitting the inverse problem. The MNP distribution is therefore gathered by simple spatial mapping of the relaxation amplitudes. This was demonstrated using fluxgate magnetometers [Rüh09] and magnetoelectric sensors [Fri19]. In other studies, the magnetic field map acquired by SQUID was used to localize MNP by selecting the highest field amplitude [War99, Rom02] or by fitting a single magnetic dipole [Wie09, Ric10]. A MNP magnetic field pattern imaging has also been demonstrated using OPM [Dol16], where the whole MNP sample was homogeneously magnetized, and the relaxation was monitored by an OPM camera with a $20 \times 20 \text{ mm}^2$ field of view. In order to improve the results obtained by the basic magnetic field map, deblurring or deconvolution methods can be applied. In [Vie20], deconvolution using the point spread function was demonstrated successfully. Also a magnetic field gradient can be used to increase spatial selectivity [Sar09a, Vie20].

MRXI as defined in this work, where each voxel within the region of interest is modeled as dipole, was demonstrated using SQUID [Bau09, Lie14, Lie16, Sch19b] and coils [Bia21]. In these references, temporal relaxation information was not included in the reconstruction. In contrast, the spatial imaging model can be extended to a spatio-temporal model to significantly improve reconstruction quality, at the cost of computation time [Bau10]. Alternatively, the temporal information can be used to distinguish between different MNP species, resulting in multi-color imaging [Coe17].

It should be noted, that the spatial resolution of recent MRXI experiments in literature [Bau09, Lie15, Sch19a, Bia21] is on the centimeter scale. It is claimed, that the achieved resolution is sufficient for the principal applicability to the targeted biomedical applications.

The following list highlights directions of possible investigations for improving MRXI, indicating also references where specific challenges were already partially addressed.

- Optimization of the excitation fields, i.e., placement and shape of excitation coils, optimization of the excitation sequences for improved imaging quality and data acquisition time [Sch19b, Sch21].
- Optimization of magnetometer placement, especially exploiting the flexible positioning of OPM.
- Optimization of magnetometer sensitivity, bandwidth and dead time (see Section 7.2).
- Optimization of current source noise, stability and switching speed (see Section 5.3).

- Exploiting prior knowledge about MNP distribution and anatomy structure, e.g., from CT or MRI measurements (which usually only delivers qualitative information about the MNP distribution). This incorporates advanced regularization of the inverse problem and optimal region of interest selection and discretization (e.g., the use of sensitivity based non-homogeneous grids).
- Accurate modeling of the system parameters, e.g., sensor noise density distribution [Coe14], MNP diameter distribution [Dol15] and nonlinear MNP magnetization dynamics.
- Adaptive and real time reconstruction of MNP distributions [Coe12].
- Minimization of geometrical and physical model uncertainties.
- Development of noise reduction methods to facilitate unshielded or moderately shielded measurements.
- Extension of the MRXI model to allow for MNP movement during the measurements, e.g., for in-flow imaging.

3.4 Other selected MNP imaging techniques

Several other techniques to non-invasively image MNP distributions are reported in literature:

- Magnetic resonance imaging (MRI) is a widely used technique to image MNP [Loe09], e.g., when MNP are deployed as contrast agents [Mot11]. In MRI, anatomical and physiological images are directly available, without any need of co-registration. The limitations are, that the MNP are measured indirectly, possibly leading to artifacts. Further, quantitative imaging is usually not possible, but is subject of current research [dR10].
- Magnetic particle imaging relies on the nonlinear magnetization dynamics of MNP. The MNP distort an applied sinusoidal magnetic field. These distortions, which appear as harmonic magnetic fields, are detected by coils. MPI offers high temporal (approx. ms) and spatial (sub mm) resolution [Wei07, vG20] of MNP distribution, but is limited to a relatively small region of interest (several cm³) due to the necessity of large magnetic field gradients to saturate the MNP. Chandrasekharan et al. [Cha20] demonstrated MPI guided magnetic hyperthermia. Work towards MPI using OPM was demonstrated by Colombo et al. [Col19].
- Magnetic remanence imaging relies on the method of detecting the magnetic remanence field of a previously magnetized MNP sample [Bau08]. Ideal (superparamagnetic) MNP do not exhibit any remanence. However, real samples often exhibit aggregates and small fractions of large (and therefore not superparamagnetic) MNP. The inverse problem is similar to the one of MRXI. In contrast to

MRXI, this method doesn't need short sensor dead times after switching off the excitation field, simplifying the operation. In contrast, no particle dynamics can be extracted from the measured signals.

For a comprehensive comparison of this and other MNP imaging methods like ultrasonic imaging, fluorescence imaging and positron emission tomography see [Shi15].

4 Objective and scope of the thesis

The aim of this thesis is to investigate the potential of commercial and non-commercial OPM for MRX and MRXI, especially considering biomedical applications and real world scenarios. The detailed main objectives of this work are:

- The investigation of the principal applicability of OPM for MRX. Part of it is the measurement of different key parameters, especially dead time, bandwidth and sensitivity. The goal is achieved, if relaxation signals of MNP can be acquired and the key parameters are identified and quantified.
- The development of a single channel OPM-MRX measurement system for the characterization and quantification of MNP. This includes the development and characterization of pulsed current sources for MRX. The formulation of suitable data analysis procedures for the extraction of relaxation parameters from OPM-MRX measurements needs to be done. The range of detectable MNP diameters must be estimated as well as the iron detection limit. The setup will be validated by comparison with SQUID measurements or simulations. Finally, the current limitations of the OPM-MRX setup have to be identified.
- The optimization of dead time, bandwidth, sensitivity and other selected parameters. The bandwidth needs to be high enough to detect immobilized or liquid suspended, clinically relevant MNP. The dead time must be neglectable at the achieved bandwidth. A sufficient sensitivity to quantify clinically relevant iron amounts is required.
- The investigation of robustness against strong magnetic fields of OPM for the possible future combination with magnetic hyperthermia.
- The realization and investigation of a multichannel OPM-MRX system using a single OPM and multiple excitation coils. Therefore, a multichannel current source needs to be developed. The mathematical inverse problem needs to be formulated and the geometrical parameters of the problem must be estimated, e.g. the excitation coils need to be localized precisely. To finally obtain a 1D reconstruction of an MNP distribution, the inverse problem needs to be solved and the uncertainties have to be quantified.
- Translation of the 1D reconstruction setup to an imaging system. For this challenge, the sensor crosstalk needs to be investigated and eventually eliminated. Further, the OPM need to be precisely localized, as the inverse problem will be

ill-posed. In this step, the flexibility of OPM sensor positioning should be exploited for the specific target.

- The realization of suitable MNP phantoms for investigating imaging key imaging parameters like separability of point-like sources, resolution, precision and accuracy.
- The validation of the developed MRXI setup. This goal is reached, if clinically relevant iron concentrations can be reconstructed with centimeter scale resolution in a sub-cubic decimeter region of interest. Further, the setup needs to be compared with state of the art experiments e.g., SQUID-MRXI.
- The realization of an OPM-MRX measurement system for unshielded or weakly shielded environments, implying the investigation of environmental noise suppression techniques. Clinically relevant iron concentrations should be quantifiable.
- The investigation of OPM-MRX system properties in unshielded or weakly shielded environments, including MNP response behavior.

5 Materials and methods

5.1 Optically pumped magnetometers

In this work, three different magnetometers were selected to investigate the potential and limitations of current OPM for MRX(I). Commercially available OPM were selected as well as experimental OPM, to cover established and innovative sensors. The selected sensors were the commercially available QZFM from QuSpin, a laboratory OPM from Leibniz-IPHT and the OMG from Twinleaf, which was luckily made commercially available by the company during course of thesis. These OPM exhibit very different properties, which were studied and exploited in experiments. The QZFM is used as reference in this work, as it is currently (2022) the most referenced OPM in literature, due to its use in magnetoencephalography (MEG) research.

5.1.1 QZFM from QuSpin

One of the first commercially available OPM was used for proof of principle MRX experiments in this work, as well as for MRXI experiments. The OPM named QZFM (generation 1) was produced by QuSpin (QuSpin Inc., Louisville, Colorado, USA). This sensor operates in the spin exchange relaxation-free (SERF) regime (see Section 2.6.2) and must be operated at very low background magnetic fields. The OPM is specified with a dynamic range of ± 5 nT, a bandwidth of 135 Hz and a sensitivity of about 15 fT/ $\sqrt{\text{Hz}}$ [Osb18]. The OPM offers two-axial vectorial magnetic field information. The gas cell has a volume of 27 mm³ and the center of the sensitive volume is located 6 mm behind the sensor front. A schematic of the OPM components is depicted in Figure 2.16.

5.1.2 Intensity modulated OPM from Leibniz-IPHT

An intensity modulated OPM (see Section 2.6.3) was used for investigating the background field dependent relaxation of MNP. The OPM setup was especially developed for this experiment at the Leibniz Institute of Photonic Technology (Leibniz-IPHT) in Jena, to allow for a small sensor-MNP distance. The magnetometer employs a microfabricated Cs vapor cell with nitrogen buffer gas (38 mbar) and a sensing volume of approx. 50 mm³. The cell consists of a 4 mm thick silicon body with a cylindrical cavity, closed by anodically bonded glass faces [Woe11]. The vapor cell is operated at 70 °C by electrical thin-film heaters glued to the side faces of the Si body and driven by a 10 kHz ac current. Circularly polarized light from a distributed Bragg reflector (DBR) laser diode at the Cs D1 transition (895 nm) is intensity-modulated at the chopping frequency f_c

resonantly tuned to the Larmor frequency f_L of the Cs atoms. It should be noted that f_c is not feedback-controlled to avoid an increased settling time and transient signals after switching-off the MNP's excitation field. In this all-optical Bell-Bloom configuration, the magnetometer sensitivity is optimized, when operated in static magnetic fields oriented perpendicular to the laser beam propagation direction [Bel61, Sch12]. The laser light transmitted through the vapor cell is detected by a Si photodiode. The photodiode current is passed through a current voltage converter (I/U) and amplifier. The signal is then mixed with the OPM laser chopping frequency f_c by a lock-in amplifier (LIA). The resulting in-phase component (LIA-X) and quadrature component (LIA-Y) are directly digitized by the LIA after 4th order lowpass filtering with a -3 dB bandwidth of 10 kHz. The OPM can be operated in background fields up to approx. 100 μ T. A schematic of the OPM components is depicted in Figure 2.13, while a photo of the OPM is shown in Figure 7.9.

5.1.3 OMG from Twinleaf

Yet another OPM with very different properties compared to the two other sensors is the pulsed OPM from Twinleaf (Twinleaf LLC, Plainsboro Township, NJ, USA). It is called OMG, which stands for Optical Magnetic Gradiometer, because it houses two single magnetometers, which are intended to form a software gradiometer. The sensor is operated in free spin precession mode, which was exploited in experiments investigating OPM bandwidth and dead time. The key to a very short OPM dead time is the use of a high intensity, 1 W pump beam laser to rapidly polarize alkali metal atoms in the sensor. The sensor employs two 27 mm³ vapor cells with a vapor of rubidium atoms (enriched ⁸⁷Rb). After pumping, the atoms freely precess and their projection is monitored by optical rotation of a linearly polarized probe beam light. The off-resonance 100 μ W probe beam light is generated by a single mode, polarization stable vertical-cavity surface-emitting laser (VCSEL). Both, the pump and probe laser are tuned near the 795 nm rubidium resonance manually. The rubidium polarization relaxation rate is dominated by spin-exchange relaxation. With the pump beam shut off for the duration of the measurement a class of systematic errors from pump lightshift to pointing noise are completely eliminated, resulting in a very clean and high precision frequency-based magnetic field measurement. The high power optical pumping substantially resets and erases the time history of the alkali polarization, rendering an independent magnetic field measurement each ms. It should be noted that there is no frequency feedback or resonance tracking as used in other types of self-oscillating magnetometers. This also enhances OPM bandwidth. The different elements of the commercially available sensor are sketched in Figure 5.1. The sensor is composed of two magnetometers; i.e., it houses two vapor cells. The pump beam and probe beam are split and distributed to the two cells, enabling a future common laser noise reduction as in [Sch10]. The two amplified photodiode signals are available as analog outputs of the OPM control electronics. Additionally, the signals are filtered with a passband between 100 and 500 kHz and are fed into an FPGA inside the OMG control electronics, which measures the frequency and sends the result via USB connection.

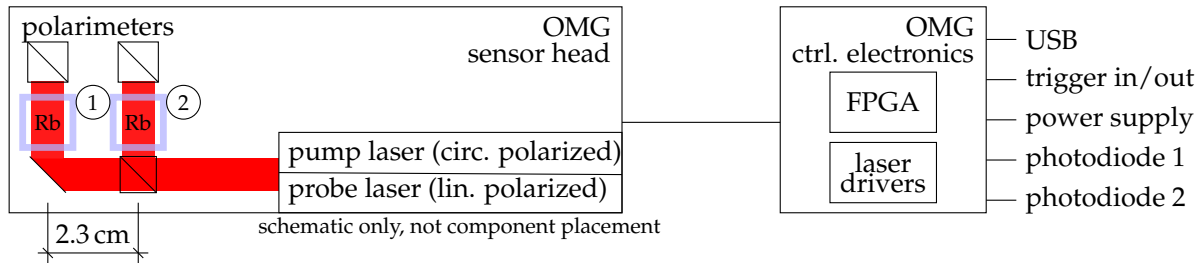


Figure 5.1: Schematic drawing of the pulsed optically pumped magnetometers (OPM), consisting of two pulsed magnetometers enclosed in a compact sensor head. Figure from [Jau21].

5.2 Magnetic nanoparticles

Various MNP in liquid suspension, as well as immobilized samples were selected for the experiments presented in this work. An important prerequisite for any MRX(I) experiment is the knowledge of the MNP's properties, since there is a large variability e.g., in terms of relaxation time. It is essential that the parameters of MNP and OPM match.

5.2.1 Resovist

A well known and well characterized particle system is Resovist[®] from Schering, Berlin, Germany. Resovist alias Ferucarbotran was clinically approved in 2002 as contrast agent for contrast-enhanced MRI of the liver [Rei03], but was later withdrawn from the market as result of safety concerns [Wan15]. The MNP with a hydrodynamic diameter of 45 nm show a bimodal core size distribution with peaks at 5 nm and 24 nm [Ebe11].

5.2.2 Bionized NanoFerrite (BNF)

Bionized NanoFerrite (BNF) MNP are widely used in hyperthermia studies for cancer treatment [Den09, Att15] (although commercial MNP with higher loss power are available [Kal09]). The MNP are available from Micromod (Micromod Partikeltechnologie GmbH, Rostock, Germany) and can be ordered with or without a functionalized surface. In this work, plain BNF MNP with two different diameters were used. The selected MNP were based on dextran. The MNP with a hydrodynamic diameter of 100 nm are water suspended and their iron-oxide core with a diameter of 45 nm consists of multiple 15–20 nm iron-oxide crystallites [Hed18]. The undiluted iron concentration is about 15 mg/mL. The MNP with a hydrodynamic diameter of 80 nm are also suspended in water. The iron concentration of the factory supplied MNP suspension is specified as 13.7 mg/mL.

5.2.3 Perimag

Perimag[®] MNP from Micromod exhibit a relatively large hydrodynamic diameter of 130 nm and are well suited as MRI and MPI contrast agents [Ebe13]. The MNP are multi-core particles, consisting of a cluster of iron oxide crystals with diameters ranging from 3 nm to 8 nm [Ebe13]. The iron concentration of the factory supplied MNP suspension is specified as 8.5 mg/mL.

5.2.4 Berlin Heart

Berlin Heart MNP (Berlin Heart GmbH, Berlin, Germany) with a mean core diameter of 10 nm to 20 nm were selected for the imaging experiments here, with the aim to compare the results with MRXI results in literature using the same MNP [Lud06, Lie15].

5.2.5 Which MNP sizes contribute to the measured MRX signal?

Given the magnetometer bandwidth, the size range of MNP contributing to the MRX signal can be estimated. When considering Néel relaxation only, which is appropriate for immobilized particles, Equation 2.1 may be used to calculate the detectable diameters. τ_0 is usually in the range of 10^{-8} s to 10^{-12} s [Wie12a]. A spherical magnetite particle with a typical anisotropy of 10^4 J/m³, a temperature of 295 K and $\tau_0 = 10^{-9}$ s is assumed. In the case of suspended MNP, Brownian and Néel relaxation occur in parallel, resulting in an effective relaxation time, see Equation 2.4. As approximation, both relaxation processes are considered separately (eventually neglecting a factor of two, when $\tau_N = \tau_B$).

With a bandwidth of 135 Hz, which is the bandwidth of QuSpin magnetometers (QZFM), detectable time constants in the range of $\frac{1}{135}$ s to e.g., 2 s are feasible. The upper limit is selected due to practical reasons. Measurement times longer than 2 s are principally possible using QZFM sensors and might be of interest for MNP characterization. Also, the long-term stability of a OPM is high, see e.g [Os18] for the long term stability of the QZFM. However, a well shielded environment like the BMSR-2 at the PTB Berlin, an actively shielded environment [San21] or a gradiometric arrangement is required to suppress background field drift. The main limit, however, is the data acquisition time itself. In an MRXI system with multiple coil excitations, a long measurement time per excitation might lead to an unsuitably long acquisition time for a patient. With the values given above, the immobilized MNP contributing to an MRX signal are calculated:

QZFM: It is calculated, that MNP with core diameters ranging from 23 nm to 26 nm can be detected with a QZFM from QuSpin. In the case of liquid MNP with a sample viscosity equal to that of water (10 mPa·s), the core diameter needs to be in the previously mentioned range. Then the detectable hydrodynamic diameter is between 124 nm and 800 nm.

IM-OPM: With a bandwidth of 500 Hz, which can be obtained with the intensity modulated OPM from Leibniz-IPHT, the lower detectable MNP core diameter limit is 22 nm,

while the lower detectable hydrodynamic diameter is 80 nm.

OMG: For a selected bandwidth of 100 kHz of the OMG from Twinleaf, the lower detectable MNP core diameter limit is 19 nm, while the detectable hydrodynamic diameter just needs to be larger than the core diameter.

It should be mentioned again, that the numbers calculated above are intended as rough estimates, not only due to possibly large parameter variation within a MNP sample. Ultimately, given a real MNP sample, only those MNP from the size distribution within the limits given above are detected. This has two important consequences: For a maximum SNR, the MNP should be designed to be within the detectable window [Dol15]. On the other hand, since all MNP samples exhibit a distribution of diameters, principally all MNP samples can be detected, hence the MNP may be designed especially for the biomedical application, and not for the imaging.

5.3 Pulsed current sources for MRX

The pulsed current source is, in conjunction with the excitation coil(s), one of the key components of an MRX(I) setup. The main requirements of both are:

- low noise when switched off
- fast switch-off with minimal ringing
- reproducible current, startup and switch-off
- reproducible timing and moderate noise when active

While for MRX a single coil is sufficient, usually more than one excitation coil is present in MRX imaging setups [Lie16]. There's therefore a need for multiple individual current sources or a multiplexing of the excitation coils.

In the following sections, two self-developed current sources are presented and analyzed in terms of the defined requirements. The first current source is digitally programmable, while the second has a fixed current setting. The main reasons for custom current sources instead of off-the-shelf ones are numerous. Many cheap power supplies use switching regulators, which very likely introduce strong noise. The switch-off-time is mostly slow and the transient behavior is not controllable. Therefore many current sources oscillate when the load is inductive. One would need to add external components and treat the current source as black box. Nonetheless, on the market exist several well designed fast and low noise current sources (e.g. from Stanford Research Systems, Twinleaf, Koheron, Sisyph), but they are usually very costly. With such current sources, the compliance voltage still needs to be considered. To anticipate, it should be noted that the current source is currently not the limiting factor for MRXI, but rather geometrical uncertainties of the mathematical model.

Programmable current source

The basic principle of a simple current source is depicted in Figure 5.2. In the schematic, R3 is the current sense resistor. The operational amplifier LF411 regulates the current by piloting the MOSFET M1. The capacitor C1 and the resistor R2 are essential for the stability of the circuit and reduce the bandwidth of the analog feedback loop. The inductance of the used excitation coil needs to be considered as well as the desired settling time of the current source when determining the values of R1, R2 and C1. The current is set by the voltage applied to the positive input of the operational amplifier and equals the dropped voltage over R3 in the steady state. A digital-to-analog converter can be used to set the reference voltage, resulting in a programmable current source.

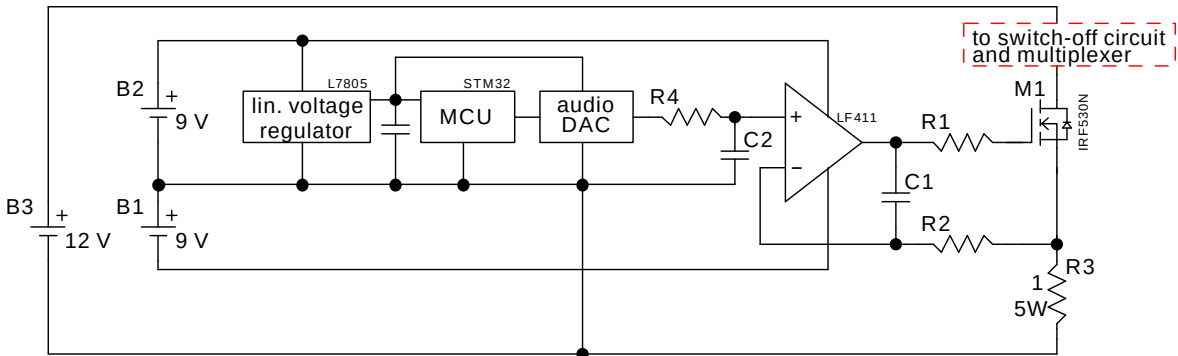


Figure 5.2: Schematic of a programmable, battery-powered current source. This device was used for experiments with the QZFM sensors and the intensity modulated OPM.

Multiplexing is simple and robust (see Figure 5.3), but has limited flexibility. Using an array of current sources, each coil can be energized individually, allowing for improved imaging results compared to sequential coil excitation using multiplexing [Sch19b]. Complexity arises in terms of minimizing crosstalk and channel-to-channel matching. The use of digital-to-analog converters (e.g., DAC53608RTET) with a common external voltage reference (e.g., MAX6071BAUT25) proved to be beneficial for the channel matching issue.

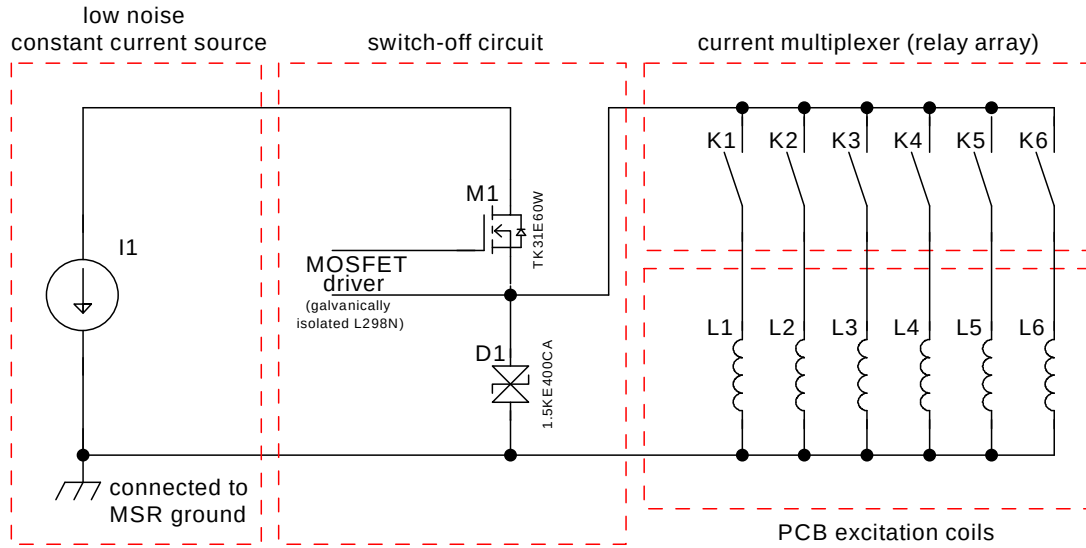


Figure 5.3: Schematic of a battery-powered current multiplexer and switch-off circuit. This device was used for experiments with the QZFM sensors. Figure from [Jau20a].

Current source with fixed current setting

A robust, cheap and simple constant current source is depicted in Figure 5.4. The current source is based on the integrated circuit LM317, which is a linear voltage regulator. The analog control loop within the LM317 regulates its output to obtain 1.25 V at the adj-pin. The resistor R2 has a resistance of 1.2 Ω , resulting in a steady state current of 1.04 A. The lowpass-filter composed of C1 and R1 stabilizes the feedback-loop. The diode D1 protects the LM317 from reverse current injection. A microcontroller (Atmega328P) manages the duration and timing of the current pulses. The switch-off of the excitation field can be synchronized with the OPM to minimize the magnetometer dead time (see Section 7.2). The OPM and the current source are electrically decoupled using an optocoupler.

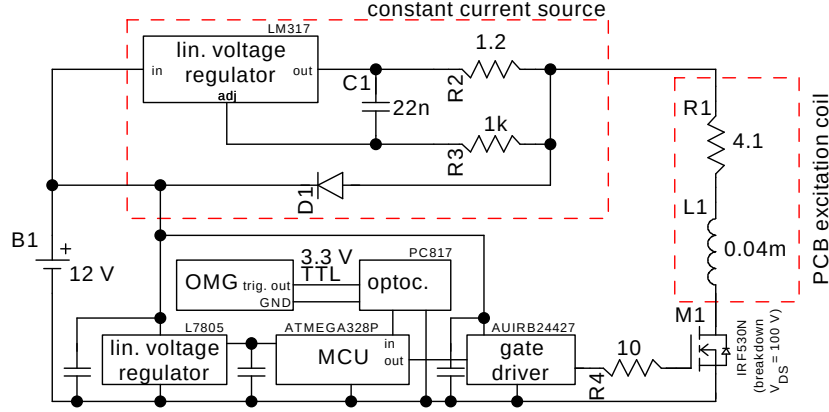


Figure 5.4: Schematic of a battery-powered excitation-coil driver with fixed current setting. The coil driver was used for experiments with the OMG (see Section 7.2). Figure from [Jau21].

Current source requirements for MRX

To transform the previously presented qualitative MRX current source requirements to quantitative requirements, several assumptions need to be made and the complete MRX setup needs to be considered.

Low noise when switched off: Considering e.g., the setup for MNP quantification using a QZFM sensor from Section 6.2, the maximum tolerable current noise in the off-state is estimated. The OPM is characterized in the BMSR-2 to show a noise density of $15 \text{ fT}/\sqrt{\text{Hz}}$ within the 135 Hz bandwidth, giving an approximate RMS noise of 174 fT. A current of 1 A in the excitation coil generates a magnetic flux density of $52 \text{ } \mu\text{T}$ at the OPM's location. Therefore, a current of one nanoampere corresponds to 52 fT at the OPM's location.

It should be kept in mind, that the leakage current of a MOSFET can be as high as $1 \text{ } \mu\text{A}$, possibly generating a field offset in the picotesla range.

The excitation circuit and the coil should be grounded with care, or be galvanically isolated from the rest of the system. In all cases, the specific particularities of a measurement environment need to be considered. It can be beneficial to operate the battery-powered current source floating, or mains-grounded, or grounded to the MSR-ground. Depending on the magnetometer-fragility on HF-noise, the use of shielded cables might be considered. This is crucial for SQUID systems, but less important for OPM systems. To avoid ground loops, it is a good practice to electrically decouple different systems using optocouplers. One caveat is the propagation delay, which needs to be kept in mind for the timing. It can be on the order of several μs for standard PC817 optocouplers [SHA03].

Fast switch-off with minimal ringing: Reference designs for fast-switching current sources can be found in [Lie16, Ded01, Zho17, Bia20]. In the case a pulsed current source and excitation coil are operated in a shielded environment, eddy currents can prevent the fast shut-off of the coil [Ded01].

Generally, for a fast switch-off, the energy stored in the coil has to be dissipated rapidly. The use of a free wheeling diode, often used to protect electronics from voltage spikes of switched inductive loads, is not recommended for this purpose. The clamping voltage of a standard diode is low, e.g., 0.7 V and so is the dissipated power, leading to a slow shut-off of the magnetic field. An increased clamping voltage can be obtained by the use of a transient voltage suppression (TVS) diode and is limited by the maximum allowed drain-source-voltage of the MOSFET which needs to be protected. Alternatively, an avalanche rated MOSFET can be used [Ded01, Zho17].

Further, the inductance of the coil and the cables from the coil to the current source need to be minimized to reduce the switch-off time [Zho17]. Small PCB coils like used in the experiments here have shown to be advantageous with an inductance in the sub-100 μH region. With a current of e.g., 1 A, the stored energy is well within the avalanche limits of the IRF530 or TK31E60W-MOSFET used and no additional TVS-diode is required. To reduce the ringing during switch-off, the parasitic capacitances of the coil, cables, and the switch-off circuit need to be minimized. The PCB design of the circuit is essential here and general considerations for switched-mode-power-supply-design can be applied. Finally, it should be noted, that when trying to measure fast transients, the bandwidth of the oscilloscope and the parasitic capacitance of the probe need not to be underrated. For the coils used in this work, switch-off times of less than 20 μs , including ringing, can be easily achieved (see Figure 7.6). After this time, a reproducible exponential decay with low nanotesla amplitude can be observed. This drift can be compensated by subtracting an empty measurement.

Reproducible current, startup and switch-off: To make reproducible measurements, the current of the excitation field needs to be reproducible, as it directly translates to the magnetization of the MNP. Not only the steady state current, but also the current profile when switching-on and off might significantly alter the magnetization of the MNP. Obviously, the specific MNP used in an experiment need to be considered for this requirements. Therefore, the on-time of the current source should be selected based on the startup time of the current source and the alignment time of the MNP. With the commonly applied fields in the low millitesla-region, the alignment time is similar to the relaxation time (details are described in Section 2.2). In doubt, the on-time should be selected long enough, with the price of a prolonged data acquisition time. The generation of a reproducible and stable current is more challenging, because current-sensing is non trivial. DC current measurements in the single digit ampere range can be achieved by measuring the voltage drop over a shunt resistor. The voltage drop and heat generation needs to be tradeoff. A shunt resistor with a low temperature coefficient should be selected. Integrated magnetic current sensors are an attractive alternative, but often exhibit nonlinearities and are mostly available with higher current ranges.

Moderate noise when active: An Ultra low noise current source can be found in [Cio98]. A second, very popular one, can be found in [Lib93], which is extended in [Sec16, Eri08]. It should be noted that, in general, the design of low-noise current sources for currents in the low milliampere region is easier than for higher currents in the single-digit ampere region [Dud17].

The presented custom current sources offer sufficient noise levels for the MRX(I) measurements presented in this work. However, it should be noted that they don't exhibit very low noise when sourcing current.

6 From quantification to imaging

6.1 Introduction

A long time has passed since the discovery and exploitation of the basic OPM techniques [Han24, Kas50b, Deh57, Bel57, DR69a, Hap72, Hap73] and the development of OPM with sensitivities comparable to SQUID [Bud00, Kom03, Gro06]. At the beginning of the work for this thesis in November 2016, QuSpin just released their first commercial version of the QZFM OPM [QuS]. It was therefore unknown how this sensor would respond to pulsed magnetic fields and if it would be suitable for MRX and MRXI. A study investigating these fundamental questions will be presented in this section. It should be noted, that the work from [Jau20a] is reported with partial modification.

6.2 Quantification of MNP with QZFM from QuSpin

6.2.1 Objectives

The first step towards MRXI with OPM is to show that OPM are in principle suitable for MRX, which is not obvious. It needs to be shown, that OPM generally withstand the millitesla excitation fields and that they are not extensively magnetized during MRX, making the measurements with different excitation fields irreproducible. Further requirements which need to be investigated are the dead time after switching-off the excitation field, the bandwidth and the sensitivity. Like stated in Section 2.2 and Section 5.2.5, the relaxation behavior of a MNP sample may strongly vary, deducing that the sensor parameters are not to be considered isolated, but need to be matched to the whole application. Slowly relaxing MNP may require different magnetometer properties than fast relaxing ones.

In this section, after showing the principal applicability of OPM for MRX of MNP, a precise quantification of MNP with clinically relevant iron concentrations will be shown and the detection limit will be investigated.

6.2.2 Materials and Methods

Setup overview The MRX setup, composed of a single QZFM OPM and an excitation coil, was operated within the BMSR-2 at the PTB in Berlin [Thi07]. The OPM electronics and the excitation coil electronics (Section 5.3) were operated outside the shielded room, but within the *rf*-shield of the MSR.

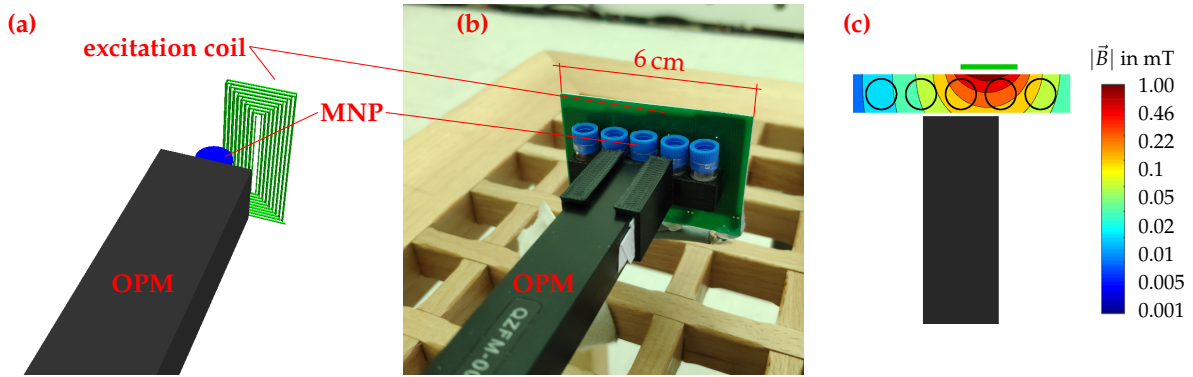


Figure 6.1: (a) Schematic and (b) photography OPM-MRX setup for MNP quantification using a commercially available OPM within a well shielded environment (BMSR-2 at the PTB in Berlin). (c) Simulated magnetic flux density map of the planar excitation coil when supplied with a current of 1 A. Please note the logarithmic scaling of the axis. Figure adapted from [Jau20a].

MNP A dilution series of immobilized Resovist[®] MNP was prepared for these experiments. Eight MNP samples with a sample volume of 140 μL and an iron amount ranging from 139.2 μg ($\approx 1 \text{ mg}/\text{cm}^3$ iron concentration) down to 5.8 μg ($\approx 41 \mu\text{g}/\text{cm}^3$ iron concentration) were freeze dried in Mannitol.

Excitation field The MRX setup is equipped with four excitation coils (see Figure 6.1b), but only one of them (see Figure 6.1a) was used in this experiment. The complete coil set is used later for 1D reconstruction (see Section 6.3). The excitation coil produces an inhomogeneous field in the sub-millitesla range. A field map of the generated field is shown in Figure 6.1c.

Data acquisition and processing The raw OPM data was acquired by digitizing its analog output at a sample rate of 1 kHz. Simultaneously, the coil current was recorded to allow for time-alignment of the MRX sequences. Five consequent MRX signals were averaged to enhance the SNR. The data was then fitted to the stretched exponential relaxation model (Equation 2.8) using the Trust-Region-Reflective Least Squares algorithm [Byr88] provided by Matlab[®] (R2017b).

MRX procedure For the MRX measurements, a single MNP sample was positioned between the OPM and the excitation coil. Then, the excitation coil was pulsed with 1 A for one second and the relaxation signal was acquired for two seconds. This was repeated five times. Then the procedure was carried out for all the other samples of the dilution series, while maintaining the same sample position. It should be stressed, that only one MNP sample is in the sample holder at any time (unlike seen in Fig. 6.1b). The distance from the center of the sample to the center of coil was about 9 mm (6 mm perpendicular

distance). The center of the MNP sample was located at a distance of 5.5 mm from the OPM’s front surface. The vapor cell center of the OPM was located 6 mm behind the surface.

6.2.3 Results

The observed noise floor in the measurements was about $15 \text{ fT}/\sqrt{\text{Hz}}$ and was dominated by sensor noise. The results from a dead time measurement are depicted in Figure 6.2. At timestamp zero, the excitation field was switched off. A 28 Hz, 22 pT magnetic field was applied to the sensor to make it possible to judge for the recovery of sensitivity of the OPM. It can be observed, that the OPM exhibits a dead time of about 20 ms, while the time to regain the full sensitivity is ≥ 35 ms.

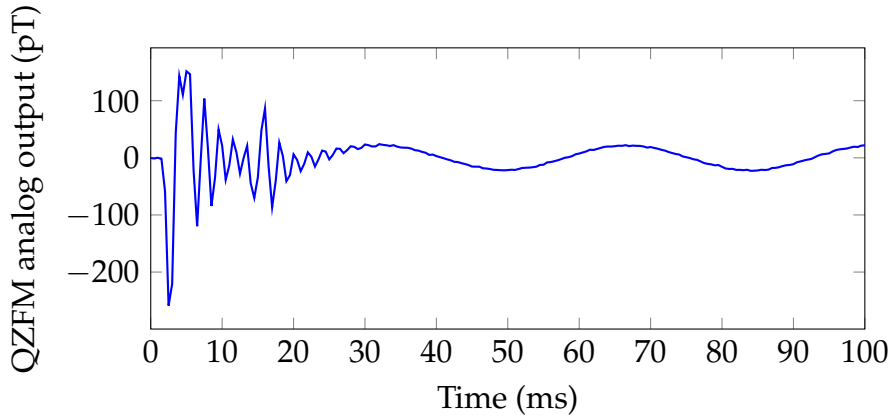


Figure 6.2: Switch-off behavior of the zero field OPM (QZFM) from QuSpin. The excitation coil is switched off at timestamp zero. A small, approx. 22 pT magnetic field with a frequency of 28 Hz is constantly applied to the OPM.

The relative (offset subtracted), unfiltered, but five-times averaged relaxation signals of each sample from the dilution series is shown in Figure 6.3a. The fitted relaxation amplitudes are shown in Figure 6.3b. Each fit matches with R_{adj}^2 of ≥ 0.99 . The fit parameters are summarized in Tab. 6.1. The linear fit of the relaxation amplitude vs. the iron concentration shows a R_{adj}^2 of 0.987. Further, the relation between fit offset value O and iron amount is also linear, and fits with $R_{\text{adj}}^2 = 0.984$.

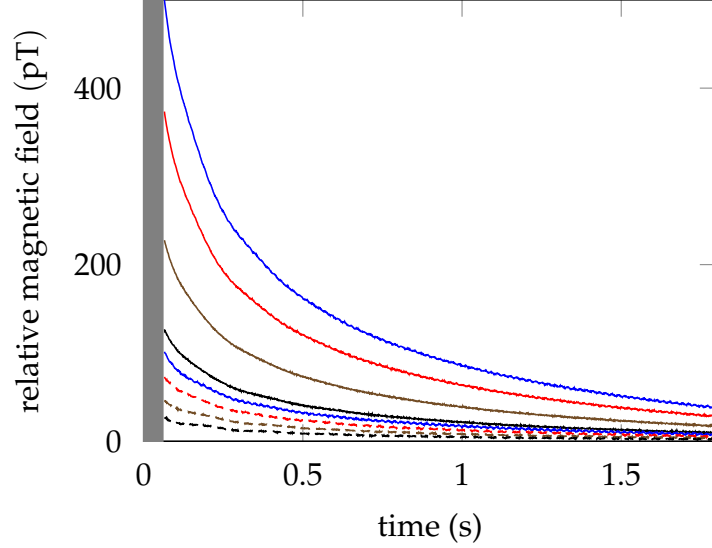


Figure 6.3: (a) Raw relaxation data, measured with a single OPM for the dilution series. The data within the sensor dead time (gray) is not shown. (b) Relaxation amplitude fits with linear regression of iron concentration vs. relaxation amplitude. Figure from [Jau20a].

Table 6.1: Estimated fit parameters for stretched exponential fits (Equation 2.8) to relaxation curves of freeze dried Resovist[®] MNP.

dilution factor	Fe (μg)	B_{relax} (pT)	τ_{eff} (s)	β	O (pT)	R_{adj}^2
1:62.5	139.2	505.1	0.31	0.66	19.2	1.00
1:83.3	87.8	375.5	0.31	0.66	14.4	1.00
1:125	58.5	228.4	0.30	0.66	9.1	1.00
1:250	29.2	127.4	0.31	0.66	4.7	1.00
1:312	23.4	100.2	0.31	0.66	3.8	1.00
1:417	17.5	73.0	0.31	0.66	2.6	1.00
1:625	11.7	46.2	0.33	0.66	1.4	1.00
1:1250	5.8	26.4	0.35	0.66	0.7	0.99

6.2.4 Discussion

The feasibility of a commercially available OPM for MRX of MNP was investigated in this study. It can be stated, that only particles with a core diameter of ≈ 23 nm to ≈ 26 nm contributed to the measured MRX signals (compare Section 5.2). Although the calculations are straight forward, it should be noted that these values should be considered as rough estimates, since parameters like the anisotropy constant K and the damping time τ_0 have a large impact and are not known precisely. For more information on τ_0 , the reader is referred to [Lel14]. Besides, the magnetometer dead time, which

leads to an increase of the lower limit of the detectable diameter range, was not included in the estimation. The upper limit of the detectable diameter range can be easily increased by prolonging the measurement time, since the QZFM has very low long-term drift (<2 pT/h according to [Osb18]). Summing up, due to the dead time in the range of 20 ms, the bandwidth of 135 Hz and the sensitivity of 15 fT/ $\sqrt{\text{Hz}}$, the QZFM (generation 1) sensor from QuSpin is well suited for MRX of slowly relaxing MNP. Similar results for the dead time were observed in [Baf19]. The recorded transient dynamics of the OPM were determined to be dominated by the internal PID loop of the electrical heater, and are ultimately governed by spin dynamics [Tan21a]. Linear quantification of the iron amount was demonstrated, with a detection limit of ≤ 5.8 μg iron. It is presumed, that the amplitude deviations from the theoretical linear response relation arise mainly from positioning inaccuracy of the MNP samples. The detection limit can be improved by increasing the excitation coil current, limited by the linear magnetization range of the MNP. Otherwise, the nonlinear magnetization needs to be taken into account in the relaxation model, which is nontrivial for real particle systems. The dead time and bandwidth of the OPM not only limit the detection limit, but also the detectable range of MNP, i.e., fast relaxing MNP cannot be detected with this setup. This issue is addressed in Section 7.2.

One important aspect is the excitation-field-generation using the PCB coil. The magnetic field produced by the coil is inhomogeneous. This has several advantages, but also disadvantages over a homogeneous excitation. In the homogeneous case, the whole sample is magnetized equally, increasing the signal amplitude and excluding unpredictable effects due to inhomogeneous magnetization. On the other hand, the inhomogeneous excitation using a PCB coil drastically reduces the complexity of the system, especially in MRXI, when multiple excitation fields are needed for spatial encoding. Moreover, inhomogeneous fields improve the condition of the associated inverse problem in MRXI [Cre12]. In this experiment, the inhomogeneity of the excitation field affected all samples in the same manner, allowing the comparison of the measurements. Minute differences might arise due to interparticle effects, but they seem to be below the detection threshold.

It should be noted, that the background magnetic field within the well shielded BMSR-2 is so low, that the OPM can be operated without the integrated magnetic field cancellation coils. However, the integrated field zeroing procedure also applies a bias field in the insensitive direction of the OPM. This field with an amplitude in the sub-nT region results in a reduced sensor noise. Similar MRX measurements were also performed within a moderately shielded room at the PTB (VACOSHIELD Advanced, former called Ak3b from Vacuumschmelze, Hanau, Germany). The shielded room is composed of two Mu-metal shells and one aluminum shell. The residual magnetic field was compensated by the OPM at the sensor startup. However, the magnetic field drifts within the MSR exceeded the dynamic range of the sensor already after a few minutes, requiring an active field compensation of the MSR, or repeated field zeroing by the OPM, which is also reported in literature [San21]. Further, the drifts compromised the relaxation signals, worsening the iron detection limit. Here, a same-oriented reference OPM, forming a software gradiometer, is recommended. The 50 Hz noise can be reduced by supplying

the OPM using a linearly regulated power supply or a battery, instead of using the factory-supplied switched-mode power supply.

With this measurements it was further shown, that OPM are suitable for remanence measurements of MNP (see the offsets in Table 6.1). While remanence measurements are in principle possible with SQUID, they are complex [Bau08]. This is due to the working principle of *rf*-SQUID, which is basically an induction loop and therefore measures only field changes and not the absolute field. The necessity of disabling the SQUID electronics during the excitation of the MNP prevents from performing simple remanence measurements, like it is possible with OPM. With SQUID, the MNP e.g., need to be remote-magnetized and then transferred to the magnetometer. Alternatively, a DC-SQUID can be used.

6.3 1D reconstruction of MNP distributions

6.3.1 Objectives

The previous Section described MRX with a single magnetometer and a single excitation coil. MRX imaging extends the quantification of MRX with spatial information. Like described in Section 2.3, multiple excitation coils and/or multiple magnetometers are used together with a mathematical model to reconstruct an MNP distribution spatially and quantitatively. It should be well noted that for the translation from quantification to (2D) imaging, the intermediate step to 1D reconstruction with a single OPM is important. Since the translation is not straight forward, it is crucial to minimize the number of uncertainties, like sensor crosstalk, and to implement a well controllable setup. After the characterization of the 1D setup and the estimation of limitations, the setup can develop further.

In this section, accurate quantitative 1D reconstruction of MNP distributions using a single OPM will be demonstrated.

6.3.2 Materials and Methods

Setup overview The setup developed for quantitative 1D reconstruction is shown in Figure 6.4 and consists of a single QZFM-OPM, four excitation coils, and a 3D printed sample holder for up to five vials, filled with MNP. This setup basically extends the quantification setup presented in Section 6.2 with multiple excitation coils (Section 5.3), while using the same freeze-dried MNP samples. The study was performed within the BMSR-2 at the PTB in Berlin.

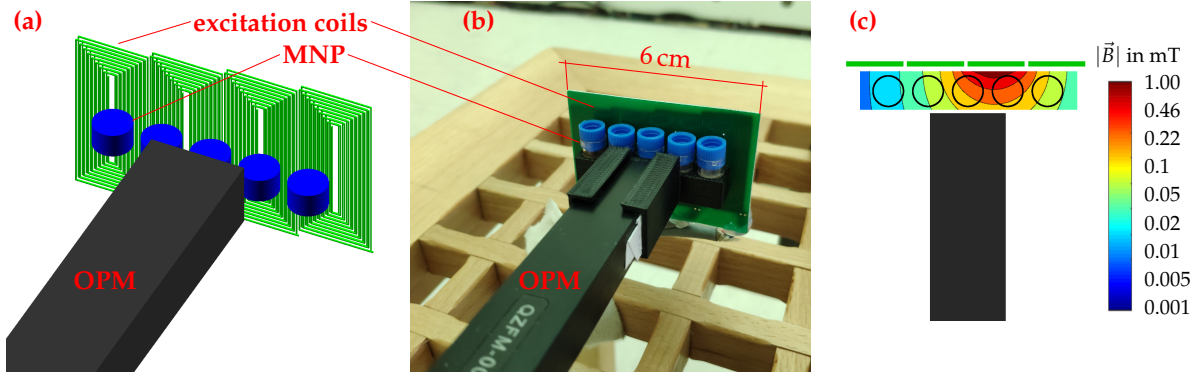


Figure 6.4: Setup for MNP quantification and quantitative 1D reconstruction. Schematic representation (a) and photo (b). Simulated magnetic field map (c) for the third (from left to right) activated excitation coil. Figure from [Jau20a].

MRX sequence and data preprocessing An MNP pattern composed of samples from the dilution series was inserted into the 3D printed sample holder. Then, the four excitation coils were pulsed consecutively for one second each, while in between the relaxation signal was recorded for 10 s. This procedure was repeated for different MNP patterns. The acquired data for each excitation pulse was time-aligned using the coil current slope and averaged five times. The data was then fitted to the stretched exponential relaxation model (Equation 2.8) using the Trust-Region-Reflective Least Squares algorithm [Byr88] provided by Matlab[®] (R2017b).

System Model and Reconstruction The general MRXI model is described in Section 2.3. In this experiment, $N_s = 1$, $N_e = 4$, and $N_v = 5$, where N_s is the number of sensors, N_e is the number of activations, and N_v is the number of voxels. Each voxel is divided into $11 \times 11 \times 11$ subvoxels. The reconstructions of the MNP distributions were realized by solving the inverse problem using an iterative Tikhonov regularization [Eng96] with added non-negativity constraint. Pearson’s rank correlation coefficient is used as a measure for reconstruction precision. It should be noted that the condition number of this setup is low (< 10), indicating that the inverse problem is well conditioned.

6.3.3 Results

The ground truth and the reconstructed MNP distribution for various phantom configurations are shown in Figure 6.5. The regularization parameter α was set manually and left fixed for all phantoms. First, a point-like MNP phantom ($139.2 \mu\text{g}$ iron amount) was placed on one end of the sample grid (Figure 6.5a) and then shifted to the other end of the grid (Figure 6.5b–e). It can be seen that point-like phantoms are reconstructed with high spatial precision and quantitative accuracy. Then a dilution series composed of five MNP vials in a descending iron concentration order was placed in the 3D printed sample holder. The well reconstructed phantom is depicted in Figure 6.5f. Finally, the order

of the samples was shuffled and then the distribution jwas reconstructed (Figure 6.5g), still with a high correlation.

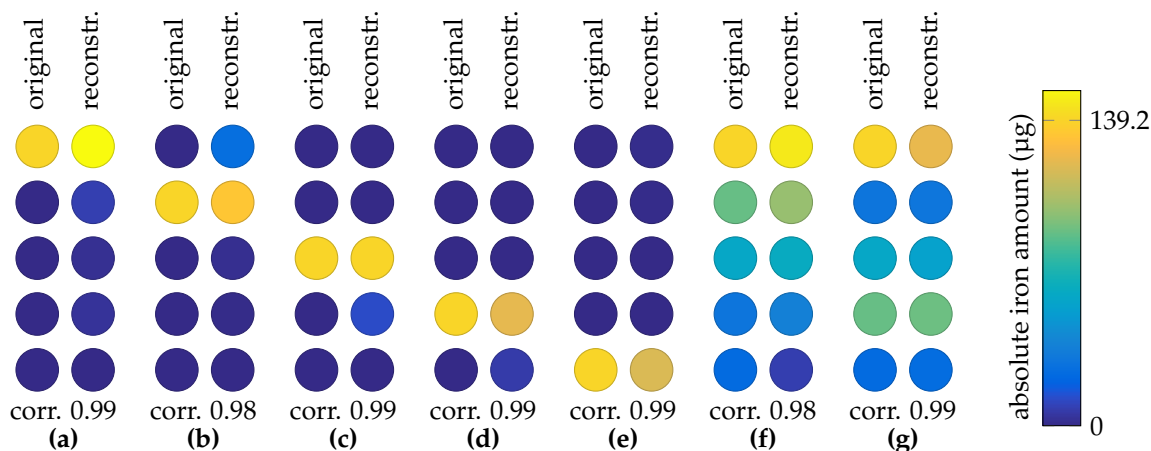


Figure 6.5: 1D reconstruction: ground truth and reconstruction for each magnetic nanoparticle (MNP) phantom. Point-like MNP phantoms in (a)–(e) and dilution series phantoms in (f) and (g). Figure from [Jau20a].

6.3.4 Discussion

In the quantification experiments (Section 6.2), the gradient produced by the excitation coil is disregarded, with the statement, that all samples are placed in the same place and are therefore affected by the magnetic gradient in the same manner. For the current experiment, neglecting the gradients and modeling the MNP samples as point-like-sources results in much worse or failed reconstruction. Therefore each voxel needs to be divided into subvoxels.

With this experiment it is shown, that OPM-MRX can be extended to quantitative 1D reconstruction.

6.4 2D imaging of MNP with OPM-MRXI

6.4.1 Objectives

At the first glance, the translation from quantitative 1D reconstruction to quantitative 2D or even 3D imaging might seem straight forward. However, this is not the case as e.g., the inverse problem gets ill-conditioned, geometrical uncertainties increase due to the increased number of sensors and/or coils and due to possible crosstalk of OPM. In this section, the challenges, caveats and possible solutions are investigated and discussed.

6.4.2 Materials and Methods

Setup and Procedure for 2D Imaging The setup developed for quantitative 2D-MRX imaging (Figure 6.6 a,b) consists of six OPM, six excitation coils, and a 3D printed 12 cm by 8 cm sample holder for MNP cubes. The excitation coils and OPM were positioned on four sides of the sample holder. The current source and multiplexer described in Section 5.3 was used. This experiment was performed within the magnetically shielded room BMSR-2 at the PTB in Berlin [Thi07].

For this experiment, Berlin Heart MNP (Berlin Heart GmbH, Berlin, Germany) with a mean core diameter of 20 nm were immobilized in gypsum cubes with edge length of 12 mm. Each cube was loaded with an iron concentration of 3.7 mg/cm^3 [Lie15].

An MNP pattern composed of MNP enriched gypsum cubes was inserted into the 3D printed sample holder. Then, the excitation coils were pulsed consecutively for one second each, while in between the relaxation signal was recorded for 10 s. The simulated magnetic field map of a single excitation field is shown in Figure 6.6c. After the extraction of the relaxation amplitudes for each OPM for each excitation pulse (fit to the stretched exponential relaxation model (Equation 2.8)), the mathematical inverse problem was solved for the 2D quantitative spatial MNP concentration. This procedure was repeated for different MNP patterns.

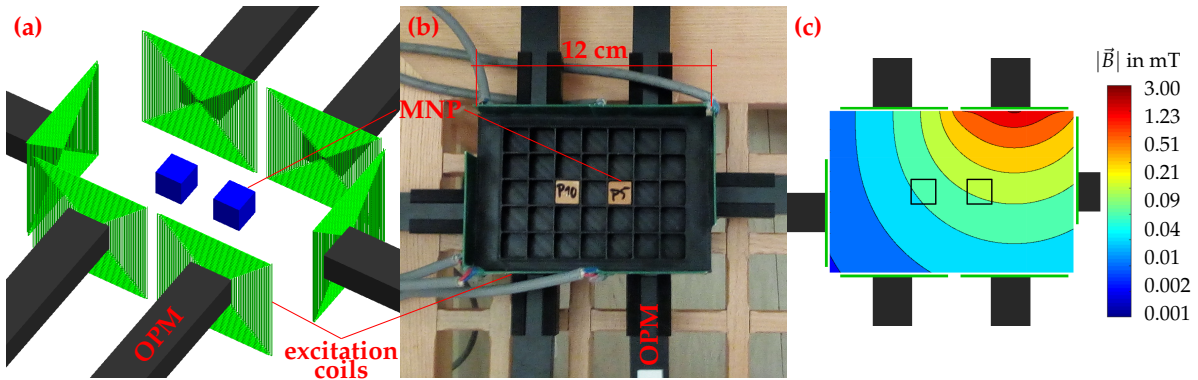


Figure 6.6: Setup for 2D MRX imaging. Schematic representation (a) and photo (b). Simulated magnetic field map (c) for the activated top-right excitation coil. Please note the logarithmic scaling of the axis. Figure from [Jau20a].

6.4.3 Results

The inverse problem associated to this 2D-MRXI setup is ill-conditioned with a condition number of $\approx 4 \cdot 10^4$. The singular values are depicted in Figure 6.7. The ground truth and the reconstructed MNP distribution for various phantom configurations are shown in Figure 6.8. It should be noted that the regularization parameter α was set once and left fixed for all reconstructions.

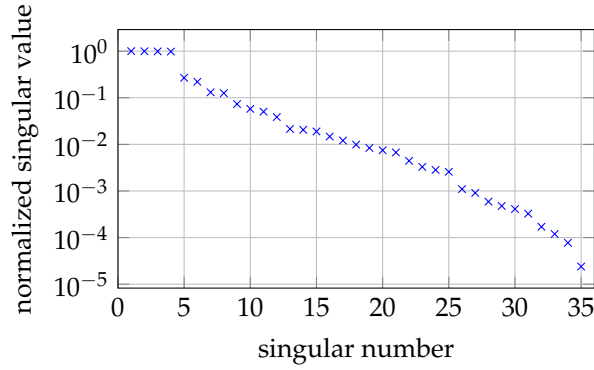


Figure 6.7: Singular values of the inverse problem of our 2D imaging setup. Figure from [Jau20a].

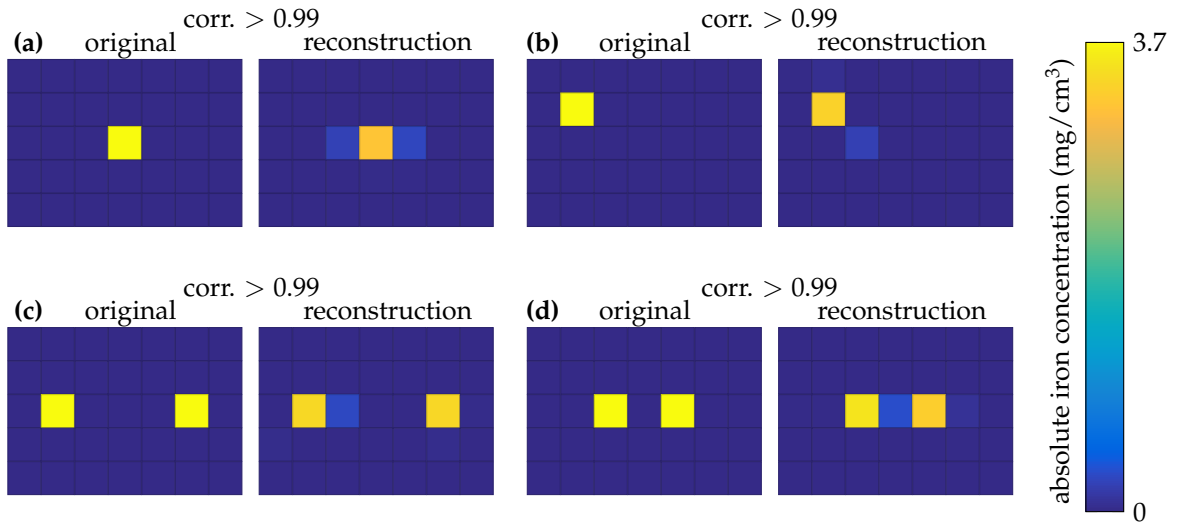


Figure 6.8: 2D imaging: ground truth and reconstruction for each magnetic nanoparticle phantom. Figure from [Jau20a].

6.4.4 Discussion

In this Section 2D imaging of MNP by employing commercially available OPM for MRXI was demonstrated. It was found in a side-study, that OPM crosstalk due to the internal modulation coils is reduced to a non-significant level if the OPM are spatially separated by approximately 3 cm, measured from case to case. An accurate system model is an important prerequisite for an accurate reconstruction of MNP distributions. This issue might be small for well posed systems like the presented 1D reconstruction experiment, however, this is one of the major aspects for ill-posed systems. The inverse problem of the 2D imaging setup is ill-conditioned with a condition number of $\approx 4 \cdot 10^4$. It is well known, that geometrical inaccuracies are a large source of error in classical SQUID-MRXI [Hö15]. It should be well noted, that a coil and sensor placement on all sides

of the phantom holder instead of lateral placement only would drastically improve the conditioning of the inverse problem. The setup geometry was selected on purpose to allow for slicewise, i.e., tomography styled imaging in the future.

To sum up, the use of multiple OPM for MRXI in a setup with 12 cm by 8 cm field of view was demonstrated. Point-like MNP distributions with iron concentrations of clinical relevance could be reconstructed precisely. Due to the simple composition of the imaging setup, it may also be adopted to operate in a small sized magnetic shielding, leading to a portable MRX imaging system. Here, care has to be taken about the static and dynamic magnetization of the magnetic shield.

6.5 Summary

In this chapter, the principal suitability of OPM for MRX was shown and then translated to 2D-OPM-MRXI. It can be stated that the commercially available QZFM (generation 1) sensors from QuSpin offer high sensitivity below $20 \text{ fT}/\sqrt{\text{Hz}}$, a bandwidth of 135 Hz and a dead time after switching off the excitation field of about 20 ms, which is confirmed by the findings of Baffa et al. [Baf19]. This OPM is well suited for operation in well shielded environments and slowly relaxing MNP can be detected and quantified. The detection limit of our setup was $5.8 \mu\text{g}$ iron of immobilized Resovist MNP and can be improved quite easily. The translation to 1D reconstruction and 2D imaging was successful. The flexibility of OPM sensor positioning was exploited for the tomography-style 2D imaging setup. Geometrical uncertainties are the dominant model errors. Gypsum cubes loaded with clinically relevant MNP concentrations could be well reconstructed within the field of view of 12 cm by 8 cm.

7 Investigation and optimization of selected parameters

7.1 Introduction

After having shown the principal usability of OPM, many follow-up questions arised in terms of current limits with respect to MRX(I) and possible optimizations. They include the reduction of dead time and the increase of bandwidth to detect smaller or suspended MNP. Further, with a higher excitation field, the detection limit could be increased. , thereby eventually also exploiting nonlinear magnetization of the MNP. QZFM have a limited dynamic range of ± 5 nT, requiring sophisticated magnetic shields or compensation techniques. How can this limitation be loosened and does an increase in background field have an impact on the relaxation of the MNP?

This chapter will elaborate on these questions, reporting work from [Jau20b, Jau21] with partial modifications.

7.2 Investigating OPM bandwidth and dead time with a pulsed free-spin-precession magnetometer

7.2.1 Objectives

Current OPM-MRX in literature and the OPM-MRX setups presented in previous sections are very well suitable for the quantification of slowly relaxing MNP. However, the detection of MNP with relaxation times in the low millisecond and sub-millisecond region, and thus the detection of particle fractions with small diameters, is prevented by a high dead time after switching-off the excitation field and low bandwidth of the OPM. In this section, a novel, commercially available, pulsed free-spin-precession magnetometer will be investigated with the goal of improving the current dead time and bandwidth limits in OPM-MRX, enabling the detection of fast relaxing MNP. The sensor presented here is named Optical Magnetic Gradiometer (OMG) and is distributed by Twinleaf LLC, Plainsboro Township, NJ, USA. It is worth noting that we had access to the sensor already at an early development stage in 2018 and that our group was the first one receiving the commercial version in 2020.

7.2.2 Materials and Methods

Setup overview The setup (Figure 7.1) consists of a single commercially available sensor package containing two separate total field pulsed OPM, and an excitation system (Section 5.3) for MNP alignment. The schematic of the current source used in this experiment is shown in Figure 5.4. The experiment was performed in an unshielded laboratory environment, with the Earth’s field as background magnetic field. The oscilloscope was USB-powered by a battery-powered notebook to prevent injecting 50 Hz noise into the system. The current source was battery-powered, too.

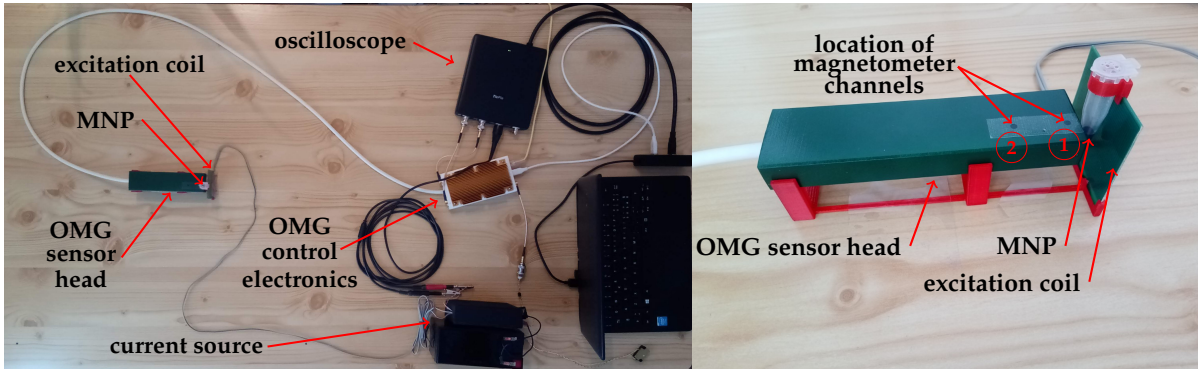


Figure 7.1: Portable tabletop OPM-MRX setup in unshielded laboratory environment. Figure from [Jau21].

OPM In the experiments presented here, the two analog photodiode outputs were digitized by a 16 Bit USB oscilloscope (Handyscope HS6 DIFF from TiePie engineering, The Netherlands) with a sample rate of 6.25 MS/s. The input range was set to ± 200 mV. The oscilloscope was USB-powered by a battery-powered notebook to prevent injecting 50 Hz noise into the system. The OMG itself was powered from an off-the-shelf 5 V switching-mode power supply. The OMG was configured to pump the system at a rate of 1 kHz, which means that the pump laser was activated every millisecond. The pump duration in each cycle is configurable. Generally, optical pumping time is optimized to offer large polarization of the atoms, rendering each cycle an independent measurement. On the other hand, pumping time must be low as it directly influences the dead time of the system. The probe laser was constantly running during the measurement. The electrical heaters, used to heat the Rb cells, were operated in non-continuous mode to minimize the magnetic disturbances during the precession measurement. After pumping the atoms for e.g., 22 μ s, the precession signal can be measured. In an idealized case there is only one exponentially damped precession frequency present in the signal. Therefore, precise and accurate frequency extraction is an essential task when developing a free-spin-precession magnetometer, as it directly translates to the magnetic field units. While in a real system the signal composition is much more complex, the simple model is considered first.

FSP frequency estimation Various frequency estimation methods are now introduced and compared. The lower boundary of the statistical precision of an unbiased frequency estimator can be calculated mathematically and is known as the Cramér-Rao lower bound (CRLB). Assuming a constant frequency and an additive white Gaussian noise, the lower boundary of the frequency estimator’s standard deviation σ_f can be calculated

$$\sigma_f \geq \frac{\sqrt{12}}{2\pi(A/\rho_A)T_s^{3/2}}, \quad (7.1)$$

with the signal amplitude A , the signal’s spectral noise density at the precession frequency ρ_A and the sampling time T_s . It should be noted that the CRLB is a mathematical fact and that it cannot be overcome. It is important to point out, that the CRLB does not depend on the sampling rate of the equipment. In the case of a damped precession, Equation 7.1 needs to be multiplied by a correction factor C , which is calculated as

$$C = \frac{N^3(1 - z^2)^3(1 - z^{2N})}{12(z^2(1 - z^{2N})^2 - N^2z^{2N}(1 - z^2)^2)}, \quad z = e^{-T_s/(N\beta)}, \quad (7.2)$$

where N is the number of samples and β is the time constant of the decay (compare Equation 2.20). The standard deviation σ_f corresponds to a magnetic noise density of $\rho_{B_0} = \sigma_f\sqrt{2T_r}2\pi/\gamma$, with the repetition time T_r [Cra46, Rao92, Gem10]. A quite simple, yet well working method is the detection and timestamping of zero crossings [Lim20, Lee21]. A clean signal without a DC offset, no ripples around the zero crossings and steep slopes at the zero crossing are a requirement. Another intuitive way for frequency extraction is by transforming the precession signal from the time domain to the frequency domain, e.g., by FFT. However, attention to the frequency binning of the FFT has to be paid, as it limits the frequency resolution. Algorithms like “Zoom FFT” aim to reduce this drawback. Alternatively, a model of the precession signal, e.g., Equation 2.20 can be fitted to the acquired signal. In this case, the model needs to be selected carefully, as well as the initial fit parameters. In the case of large noise and distortions of the signal, advanced methods can be applied to separate the precession signal from the rest, e.g., using empirical mode decomposition [Ril03, SG13]. All the mentioned algorithms have in common, that an average frequency is estimated. Hence they may be used for analyzing the precession signal of an FSP-magnetometer where the magnetic field change is slow in contrast to the precession frequency.

Another well known approach is the instantaneous frequency estimation via Hilbert transform. The Hilbert transform \mathcal{H} can be interpreted as a 90° phase shifter. The instantaneous phase can therefore be calculated by unwrapping $\arctan\left(\frac{\mathcal{H}(y(t))}{y(t)}\right)$. The derivative of the instantaneous phase is the instantaneous frequency, which can be converted to magnetic field units by scaling with the gyromagnetic ratio γ . In this study, the Hilbert transform implementation provided by SciPy is used. In this implementation, the Hilbert transform is computed by calculating the FFT of the signal, discarding the negative frequency components, and calculating the inverse FFT.

Like mentioned before, the connection between magnetic field and precession frequency in a FSP-magnetometer might seem simple and straight forward, however it is not. At least the following aspects need to be considered:

1. At a constant, homogeneous magnetic field, multiple frequencies are present in the precession signal. These frequencies are governed by the Breit–Rabi formula (hyperfine and Zeeman splitting).
2. If a constant magnetic field gradient is applied, parts of the atomic species are exposed to higher magnetic fields than other parts of the species, assuming a short diffusion length of the atoms. Therefore they exhibit different frequencies, which is the analogon of a broadened linewidth in resonant magnetometers. To counteract this problem, small vapor cells can be employed. Additionally, the diffusion length can be increased by lowering the buffer gas pressure, leading to an averaging effect over the volume. However, both measures might lead to a decrease in sensitivity. A more detailed discussion is found in Section 2.5.
3. A non-constant magnetic field yields a frequency modulation of the precession frequency.

7.2.3 Results

Rawdata analysis, 1 kHz sample rate frequency extraction and spectral noise density

One of the OMG's analog outputs (the amplified photodiode signal), captured by an oscilloscope, is depicted in Figure 7.2a. The OMG was exposed to environmental noise only. The current source was unpowered during this measurement.

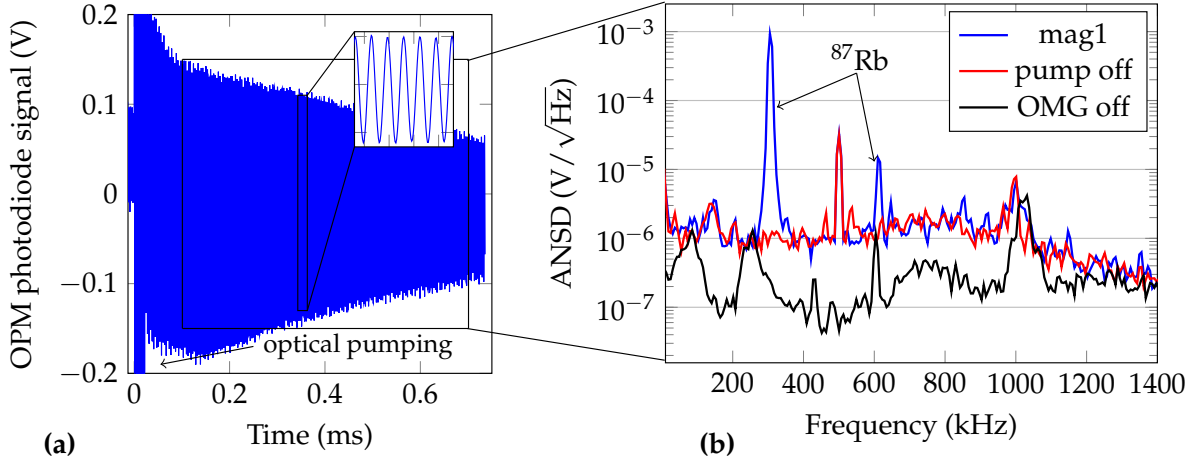


Figure 7.2: **(a)** Unshielded raw OMG photodiode signal as output by the OPM electronics and recorded using an oscilloscope. **(b)** Amplitude noise spectral densities (ANSD) of the raw OMG analog output: normal operation (blue); pump laser always off (red); OMG unpowered (black). The data used for the calculation of the ANSD are recorded 100 μ s to 700 μ s after the pump pulse. Figure from [Jau21].

The signal corresponds to the free spin precession of the alkali atoms. At timestamp 0 s, the pump laser was activated, saturating the photodiode amplifier. The amplitude spectral density of the precession signal is shown in Figure 7.2b. Three spectral densities are shown: OMG in normal operation mode; with deactivated pump laser and therefore with no visible polarization rotation; with the OMG completely unpowered. The noise spike at 500 kHz arises from the OPM electronics and not from the switched mode power supply. This was verified using a linearly regulated power supply. The 305 kHz signal component is the free-precession signal of ^{87}Rb and corresponds to the Earth's magnetic field of 43.6 μ T. The peak's width is determined, among other reasons, by the energy splitting and the gradient applied to the vapor cell. The harmonic at 610 kHz may arise due to orientation-to-alignment conversion due to the linearly polarized probe laser or due to a background magnetic field with a vector component parallel to the pump beam [Roc12, Len14].

Next, a several second long data stream was recorded using the oscilloscope. Simultaneously, the magnetic field magnitudes, as obtained from the OMG's FPGA were recorded. The data stream was split into snippets of 1 ms length, and the average precession frequency within each snippet was extracted by fitting a free-precession model (Equation 2.20) to the data. The precession frequency was then converted to magnetic flux density units. This procedure was repeated for the second magnetometer channel. A software gradiometer was formed by subtracting the results of both channels. Next, the magnetometer and software gradiometer spectral noise density using the FPGA data and using the fit data was calculated and shown in Figure 7.3. The noise level of the FPGA data and fit data was about 5 pT/ $\sqrt{\text{Hz}}$ at 500 Hz for the magnetometers. The software gradiometer noise floor of the FPGA data was about 600 fT/cm/ $\sqrt{\text{Hz}}$, and it was

1.3 pT/cm/ $\sqrt{\text{Hz}}$ for the fit data. The observed suppression ratio of the environmental 50 Hz noise by the software gradiometer was about 176.

The noise floor of the fits is now compared to the CRLB. $\beta = 0.80$ ms results from a fit of the filtered free precession decay signal to the theoretical model (Equation 2.20). Together with the sampling time $T_s = 600 \mu\text{s}$, this results in $C \approx 2.15$. The amplitude $A = 0.16$ V, the spectral noise density $\rho_A = 0.85 \times 10^{-6} \text{ V}/\sqrt{\text{Hz}}$ and the repetition time $T_r = 1$ ms result in a theoretical lower bound of the magnetic noise density of $\rho_{B_0} = 1.9 \text{ pT}/\sqrt{\text{Hz}}$ for the fit data. The theoretical gradiometric noise floor for the fit data scales with $\sqrt{2}$, which gives $1.1 \text{ pT/cm}/\sqrt{\text{Hz}}$. As it can be observed in Figure 7.3, the gradiometric noise floor obtained by the FPGA is lower than the one obtained by curve fitting. The reason is that the curve fitting results are limited by quantization noise of the oscilloscope, while the FPGA readings are of higher precision. An analysis of the FPGA performance can be found in the appendix of [Lim20], while attention has to be paid to the larger baseline and the lower sampling rate used in [Lim20].

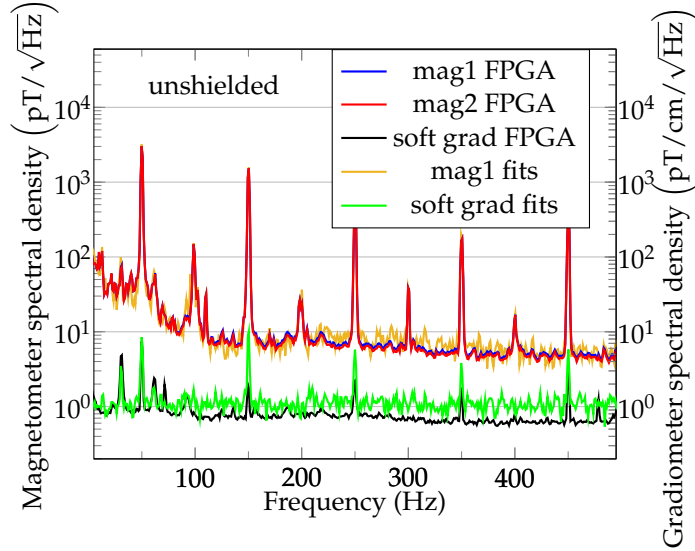


Figure 7.3: Amplitude noise spectral density (ANSD) of the unshielded OPM in a laboratory environment. The OMG is configured to pump for 22 μs . The software gradiometer baseline is 2.3 cm. Figure from [Jau21].

Bandwidth The bandwidth of the OMG in an unshielded environment was estimated by applying a sinusoidally modulated magnetic field with an amplitude 300 nT in the same direction as the background magnetic field. From the bandpass-filtered photodiode signal, the instantaneous magnetic field was calculated using Hilbert transform and the result was 100 kHz lowpass-filtered. Then, a sine wave with fixed frequency (but unknown amplitude and phase) was fitted. The estimated amplitude response is shown in Figure 7.4 and the estimated bandwidth is 100 kHz, limited by the applied lowpass-filter. The filter’s stop frequency was selected arbitrary and can be increased or decreased, depending on the application (compare also [Wil20]). However, like elaborated before,

the increase of the noise floor proportional to the frequency needs to be considered in practical applications.

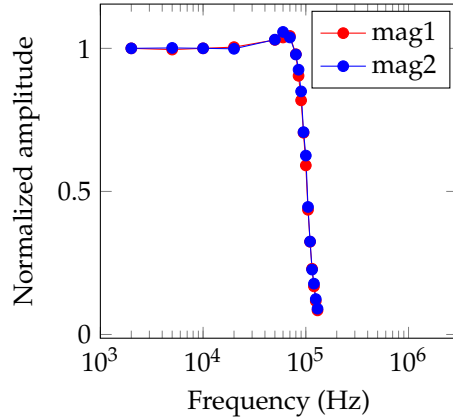


Figure 7.4: Magnetometer amplitude response over OMG bandwidth for both magnetometer channels using Hilbert transform. Figure from [Jau21].

High frequency noise investigation The shot-to-shot repetition rate of the pump laser defines the white-noise-floor bandwidth of the magnetometer, which is 1 kHz in this case. Further, it is shown here, that it is possible to acquire magnetic fields with frequency components of up to 100 kHz, without observing any lowpass-effects. However, in the frequency regime between 1 kHz and 100 kHz the sensitivity degrades linearly with detection frequency. This linear noise increase is typical for free precession decay magnetometers [Wil20], but can also be found in Mx-magnetometers [Ver20]. This can be explained considering Equation 2.21). The varying magnetic field, e.g., $B(t) = \sin(2\pi f_1 t)$, contributes with its integral to the phase $\varphi(t)$. Therefore, the amplitude of the oscillating part of the phase decreases with f_1 . This decrease is reverted when calculating the phase derivative for obtaining the instantaneous frequency. However, the general system phase noise is white, which is converted to a linearly increasing magnetic field noise floor due to the derivative [Wil20, Li20]. The results obtained from measurements match the theory, as it can be observed in Figure 7.5. Note that the magnetometer noise approaches the gradiometer noise for high frequency data, in part due to the decreasing ambient magnetic noise for high frequencies. The observed magnetometer noise floor for unshielded measurements at $B_0 = 43.6 \mu\text{T}$ with a magnetic field sample rate of 100 kHz is about $80 \text{ pT}/\sqrt{\text{Hz}}$, while $\approx 80 \text{ pT}/\text{cm}/\sqrt{\text{Hz}}$ is obtained for the gradiometer.

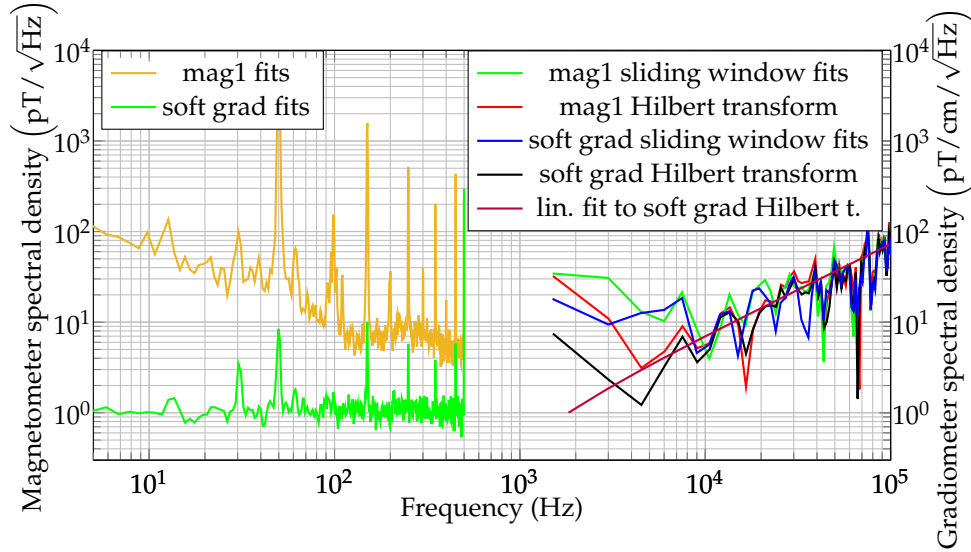


Figure 7.5: Unshielded magnetometer noise spectral densities using free-precession decay fits (brown), sliding window fits (green) and Hilbert transform (red). Unshielded gradiometer noise spectral densities using free-precession decay fits (green), sliding window fits (blue), Hilbert transform (black) and linear fit to the Hilbert transform (purple). Figure from [Jau21].

Dead time In MRX, the sensor dead time after switching-off of the excitation coil is a critical parameter. Figure 7.6 shows the coil current and the photodiode signal of the magnetometer channel close to the excitation coil. It takes approximately 50 μ s from the start of the coil switch-off to the end of the OMG's pumping period. Together with 15 μ s of data discarded during data analysis this results in a system dead time of 65 μ s. To conclude, both, the switch-off and ringing-time of the excitation coil, and the data analysis limit the current dead time of the system.

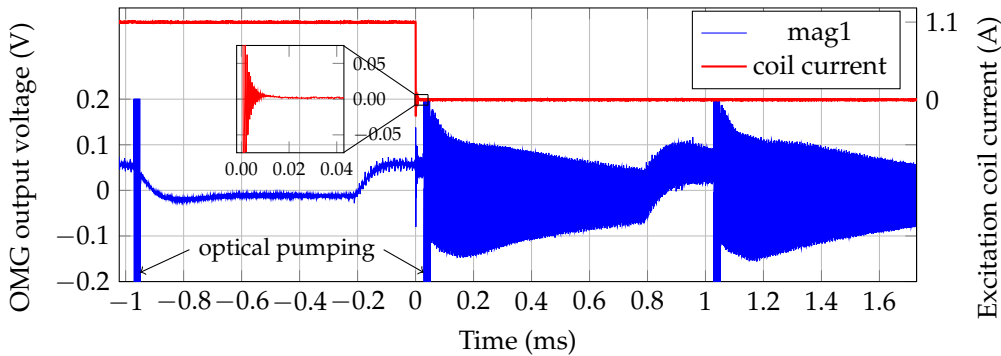


Figure 7.6: Coil current and OPM photodiode output. The optical pumping starts 28 μ s after initiating the coil shut-off. The signal distortion prior the pump pulses (i.e., periods -0.2 ms to 0 ms and 0.8 ms to 1 ms) is caused by the electrical heater of the OMG. Figure from [Jau21].

7.2.4 Discussion

The OMG offers a gradiometer sensitivity of about $600 \text{ fT/cm}/\sqrt{\text{Hz}}$, as it is acquired in an unshielded environment and using the internal FPGA. In combination with the 1 kHz bandwidth, it is in principle suited for MRX measurements. A high sensor bandwidth is essential for MRX, and for the formation of software gradiometers. Using the Hilbert transform approach, a bandwidth of $\geq 100 \text{ kHz}$ can be achieved, with the drawback of a linearly increasing noise. Therefore, additional care must be taken when trading off the bandwidth and sensitivity in practical applications. When calculating the Hilbert transform numerically, some limitations have to be known: The modulation frequency must be smaller than the precession frequency at B_0 , otherwise generated frequency sidebands are discarded. By separate treatment they still can be demodulated [Wil20]. Typically, the Hilbert transform is realized as digital filter or incorporates a Fourier transform. Therefore, distortions of the estimated phase near the data-boundaries arise. There are several ways to account for this, e.g., by padding/extrapolating the raw data with, e.g., a mirrored version of the raw signal. Here, no padding is used, but the first data points are discarded. This could be addressed in future improvements. A very promising alternative to the Hilbert transform was recently presented at the Hot Vapor Workshop 2021 [Per]. The idea is to extract the quadrature component of the precession signal directly from the OPM, and not to calculate it in post-processing. According to density matrix calculations and first experiments, the quadrature signal can be acquired when placing a second photodiode at the polarizing beamsplitter after the cell. In other words, the individual photocurrents of the balanced polarimeter are out of phase by 90° and can be used to estimate the instantaneous phase. A detailed investigation of the limitations of this approach are not yet published.

The achieved dead time of $65 \mu\text{s}$ is outstanding and can be further optimized by rather simple modifications of the excitation coil system and by integrating the optical instantaneous phase readout, like described above. The dead time will then be limited by the time needed for optical pumping, which is limited by the pump laser power. In future studies, transient effects due to the strong laser pulses need to be investigated. This includes effects on the photodiode amplifiers, as well as spin ringing.

7.3 High excitation fields in OPM-MRX

7.3.1 Objectives

The reduction in system dead time and the increase of sensor bandwidth leads to the follow-up question regarding the upper limit of the excitation field amplitude. This is investigated experimentally in this section.

7.3.2 Materials and Methods

Setup overview The setup (Figure 7.7) consists of an OMG and a hand-wound excitation coil and is operated in an unshielded laboratory environment. The OMG is placed

underneath the excitation coil and the MNP sample is placed on top of the OMG, at the position of one magnetometer channel (see Figure 7.7). The MNP sample with a clinically relevant iron concentration ($3.7 \text{ mg/cm}^3 \text{ Fe}$) consists of a gypsum cube of Berlin Heart MNP (see Section 6.4 and [Lie15]).

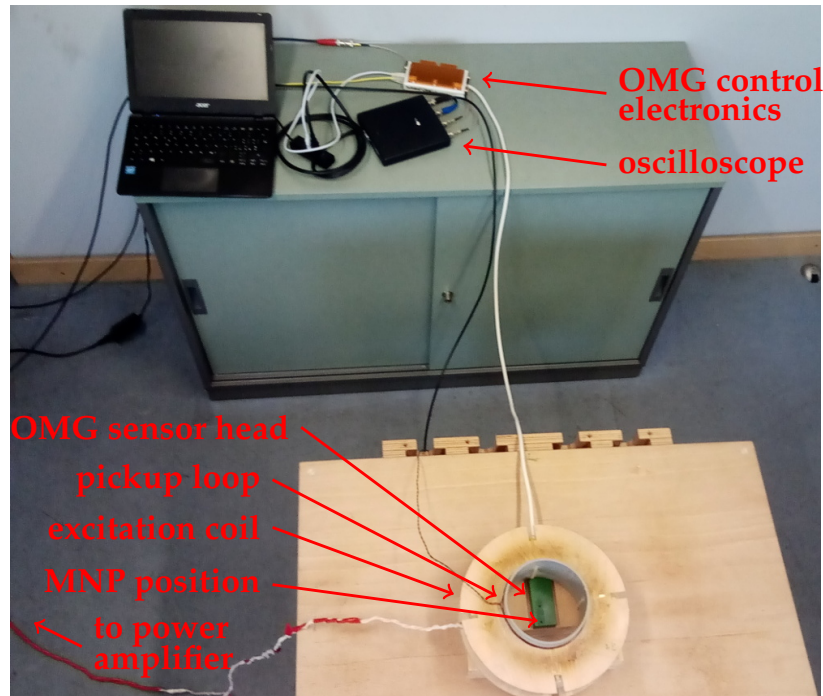


Figure 7.7: Unshielded OPM-MRX setup with possible MRX excitation fields of up to 100 mT. The battery powered notebook, the USB-oscilloscope and the OMG control electronics are visible on the upper part of the figure. The OMG’s sensor head and the MRX excitation-coil are visible in the lower part of the figure. The position where the MNP sample is placed later is indicated by an arrow. The power amplifier is not visible, as it is located at a distance of about 3 m. Figure from [Jau21].

Excitation coil and current source The excitation coil is a 304-turn hand-wound coil with an inner diameter of 125 mm, a resistance of 0.9Ω and an inductance of 16.2 mH. At its center the coil produces a magnetic flux density of 2.15 mT/A. The coil is powered using a precision power amplifier PA2032A (Rohrer GmbH, Munich, Germany), which is specified to output $\pm 75 \text{ V}$, $\pm 60 \text{ A}$. A fast shut-off of the coil is achieved using solid state switches and a network of TVS-diodes. The switch-off of the excitation coil is monitored by a pickup loop.

MRX procedure The hand-wound excitation coil (Figure 7.7) is loaded for 200 ms with currents from 0.5 A to 50 A, resulting in magnetic flux densities at the sample position in the range of 1 mT to 100 mT. The experiment is performed using the highest excitation

field first.

The magnetic field values at timestamps 2.44 ms and 120 s of the OMG's FPGA data are used to calculate the relaxation amplitude ΔB .

7.3.3 Results

During this experiment, the unshielded gradiometric noise floor is about $1 \text{ pT/cm}/\sqrt{\text{Hz}}$. The gradiometric FPGA data of MNP's embedded in gypsum is shown in Figure 7.8a. The FPGA data is not averaged or filtered. No empty measurements are subtracted, as the 50 Hz gradient is larger than the effects from the excitation coil. Therefore, subtracting non-mains-synchronized data would result in a slight degradation of the data. The first valid data point is 2.44 ms after initiating the excitation coil switch-off. The excitation coil ringing in the first gradiometer sample is less than 1 nT/cm . The visible static gradient of approx. -50 nT/cm corresponds to the superposition of the MNP sample's remanence magnetization and the static gradient in the laboratory environment of -11.56 nT/cm . On the large time-scale it can be observed that the MNP are saturated for excitation fields $\geq 10 \text{ mT}$, which was also observed in SQUID-MRX measurements of the same sample. The estimated relaxation parameters are summarized in Table 7.1.

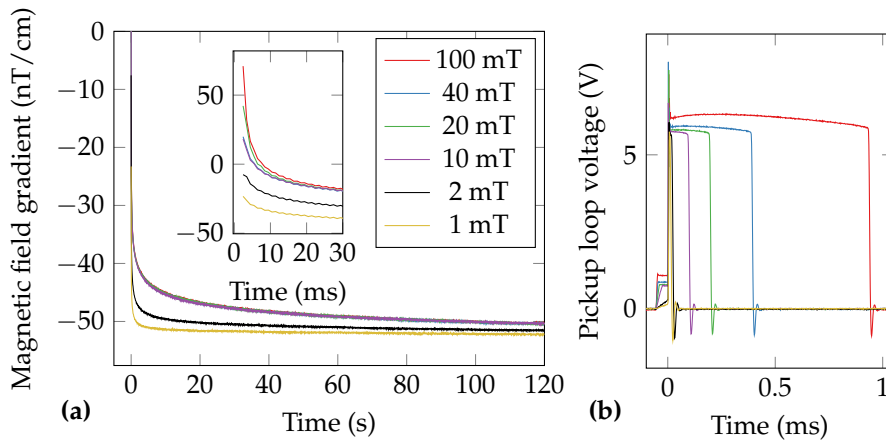


Figure 7.8: (a) FPGA-data of MRX of MNP embedded in gypsum at different excitation fields of up to 100 mT. The inset shows a zoom of the first 30 ms of the relaxations. Please note the different time scale of the figure and inset. The data were not averaged. (b) Pickup loop voltage during the shut-off of the different excitation fields. Figure from [Jau21].

Table 7.1: Estimated relaxation parameters ΔB , $t_{1/e}$ and offset O of relaxation curves with excitation fields ranging from 1 mT to 100 mT. The sample consists of gypsum-immobilized MNP with a total iron amount of 6.4 mg.

$B_{\text{excitation}}$ (mT)	ΔB (nT/cm)	$t_{1/e}$ (ms)	O (nT/cm)
100	120.98	6	-50.01
40	69.98	48	-50.09
20	92.34	16	-50.14
10	68.30	58	-50.07
2	43.66	58	-51.24
1	28.65	40	-51.94

7.3.4 Discussion

Special care has to be taken when observing the MRX results, as the coil-shut-off is not immediate and ranges between $\approx 10 \mu\text{s}$ for the 1 mT field and $\approx 1 \text{ ms}$ for the 100 mT field (Figure 7.8b). Therefore, the current decay slope's effect on the MNP's relaxation behavior might not be neglectable when analyzing the data on the short time scale (the first few ms). This was the reason for the selection of slowly relaxing MNP for this experiment. Besides this effect, it can be observed, that the extracted relaxation parameters are nonlinear, and non-monotonous with respect to the excitation field amplitude. This is not an effect of OPM measurements, as a similar behavior was observed in SQUID measurements of the same sample. Due to limitations, the 100 mT SQUID MRX measurements were not published. It is likely, that interparticle-effects, as well as the nonlinear magnetization of different diameter fractions contribute significantly to the signals at high excitation fields. It is mentioned, that a similar non-monotonous effect of the relaxation parameters was observed for Brownian relaxation in [Sar11].

It should be noted that the decision of performing this experiment in an unshielded environment is well reasoned. Generating such large fields within an MSR would cause the walls to be magnetized notably. While the generated offset field and field gradient of the walls might be tolerable, the magnetization of the MSR walls will also decay. This decay would be superimposed with the relaxation signal of the MNP, requiring the separation of both signals, e.g., by subtracting an empty measurement.

To sum up, OPM-MRX is not limited to small excitation fields. The current setup with excitation fields of up to 100 mT might be of interest for studying interparticle effects and offers the possibility to incorporate nonlinear relaxation behavior in MRXI. Further, the robustness of the magnetometer implies the possibility of combining magnetic hyperthermia and MRX in a single setup. Yet, this needs to be shown in future experiments.

7.4 OPM-MRX at DC background fields

7.4.1 Objectives

For biomedical applications, it is crucial to reduce or remove the magnetic shielding, as it is an important factor in terms of cost and flexibility. It was shown that while SERF magnetometers are limited to a relatively small dynamic range in the nanotesla range, total field OPM can be (and mostly need to be) operated at elevated background field in the microtesla range, operating also at Earth scale magnetic fields. To translate this to MRX, a prerequisite is the knowledge of the influence of background magnetic fields on the MNP's relaxation. In this section, an experimental OPM will be used to investigate the arising challenges for MRX at background magnetic fields like the Earth's field.

7.4.2 Materials and Methods

Setup overview An overview of the OPM-MRX setup is shown in Figure 7.9. An intensity modulated OPM designed by the Leibniz IPHT was used for this experiment. The Cs cell and photodiode of the OPM, and the MNP sample and excitation coil were positioned within a magnetically shielded barrel. The OPM electronics and excitation coil electronics (Section 5.3) were operated outside the shield.

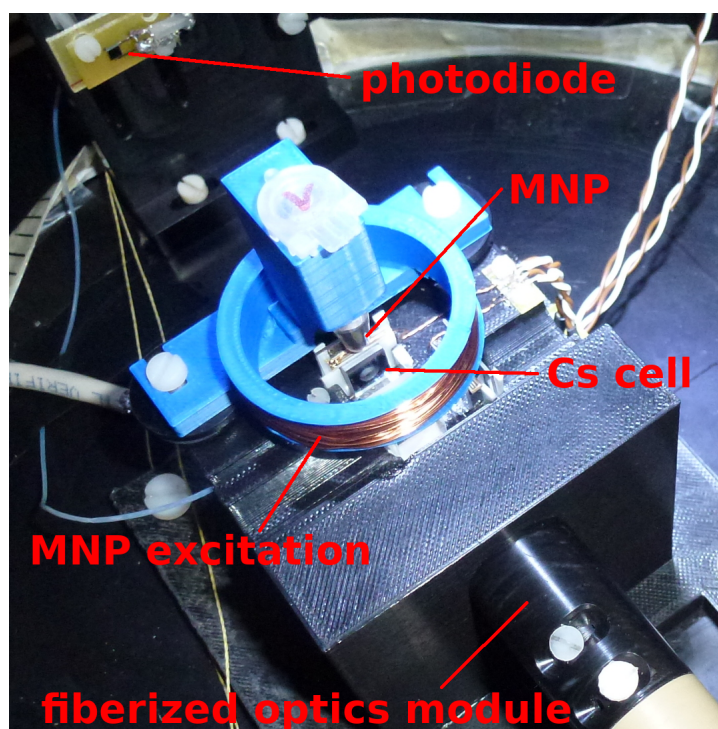


Figure 7.9: MRX setup with OPM, MNP sample and MNP excitation coil (blue). The setup is housed in a magnetically shielded barrel. A three-axis Helmholtz coil system (not visible) within the shielding is used to generate the background magnetic field. Figure from [Jau20b].

MNP Plain BNF-Dextran MNP were used in this experiment. Two samples of 140 μL were prepared. One sample was composed of 100 μL liquid (factory supplied) MNP and diluted in 40 μL distilled water, whereas the second sample consisted of 100 μL MNP, embedded and thus immobilized in gypsum, resulting in a total sample volume of 140 μL . The undiluted iron concentration was about 15 mg/mL, resulting in an iron amount of 1.5 mg in each sample.

Excitation field The excitation coil was a hand wound, 65-turn, 48 mm diameter coil, supported by a 3D printed structure (Figure 7.9). The coil driver was set to produce a magnetic field of about 1 mT at the center of the MNP sample.

Data acquisition and processing The in-phase component and quadrature component of the OPM were recorded by the LIA at a sample rate of 107.1 kHz. The auxiliary input of the LIA was used to synchronously acquire the MNP excitation coil current, which serves as trigger for the data processing. In order to remove spurious frequency components emerging from the electrical AC heating, the OPM data was preprocessed in software by lowpass filtering with a cutoff-frequency of 1 kHz for liquid MNP and 100 Hz for MNP immobilized in gypsum. The digital filter was realized as Bessel filter to preserve sharp edges in the data. It has also the important advantage of a constant group delay in the passband. Since the relaxation signal is of an exponential form, a high OPM bandwidth is desired to capture early parts of the relaxation. Latter parts of the relaxation, however, do not require high bandwidths, but would benefit from a high magnetometer sensitivity. To satisfy both requirements, adaptive filtering or resampling can be implemented [Ebe06]. With a similar effect, in this experiment, the data was weighted exponentially during curve fitting. The fits of the data to the relaxation model, which was selected as the sum of two stretched exponentials (Equation 2.8) (to account for bound and unbound MNP), were performed using the trust-region-reflective least squares algorithm [Byr88] provided by Matlab[®]. For the extraction of the relaxation amplitude and the integral relaxation time, time intervals were selected as [12 ms, 280 ms] for liquid MNP and [0.12 s, 6.5 s] for immobilized MNP, respectively. This data analysis was repeated for several subsequent MRX sequences at a fixed background magnetic field. Additionally, the analysis was performed on three or seven times averaged MRX data for immobilized or liquid MNP, respectively.

7.4.3 Results

OPM characterization Figure 7.10 shows the noise level of the OPM at different background magnetic fields, which was varied from 5 μT to 100 μT . The noise floor was around 200 fT/ $\sqrt{\text{Hz}}$ at 500 Hz for all configurations, limited by excess laser intensity noise, while the shot-noise limited OPM sensitivity level was 51 fT/ $\sqrt{\text{Hz}}$. Common visible spikes in the noise spectrum arised at the mains frequency and its harmonics, whereas the spikes occurring at a single background magnetic field only, e.g., the spike at 390 Hz at

$B_0 = 5 \mu\text{T}$, arising from LIA mixing (leakage) with the AC current driving the OPM heater.

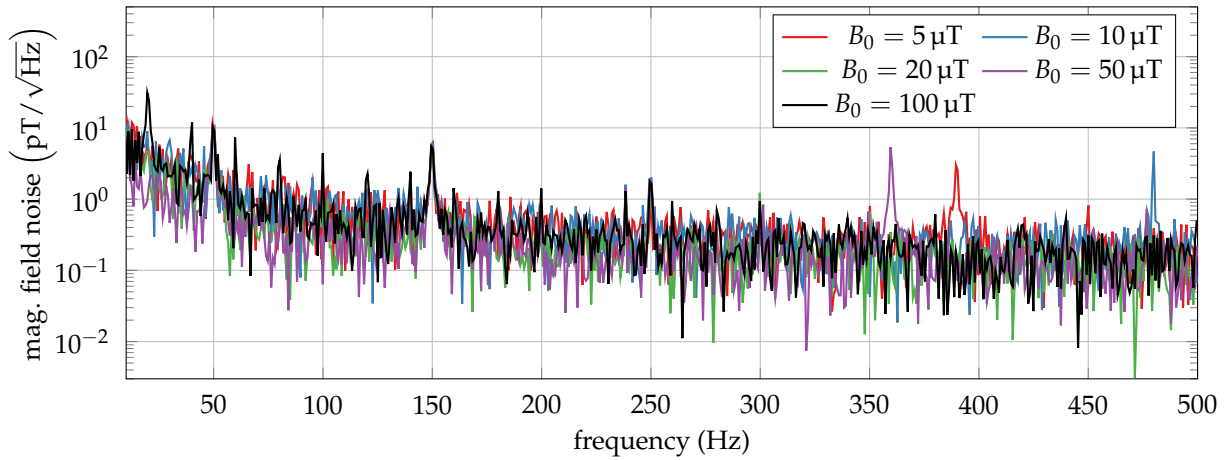


Figure 7.10: OPM noise spectrum. Base noise of the OPM at different background magnetic fields from $5 \mu\text{T}$ to $100 \mu\text{T}$, measured within a three layer magnetically shielded barrel. Figure adapted from [Jau20b].

The OPM frequency response was estimated using a spectrum analyzer (HP 35460A) and a random-noise-fed pancake coil, placed near the OPM (Figure 7.11). The OPM bandwidth was estimated to be about 500 Hz. It is noted, that the bandwidth did not significantly change at different background magnetic fields $\leq 100 \mu\text{T}$.

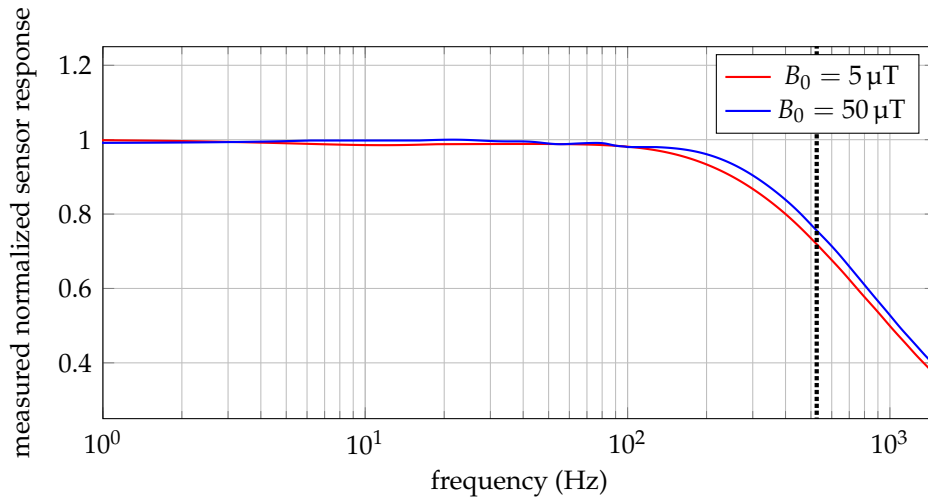


Figure 7.11: Measured OPM frequency response at $B_0 = 5 \mu\text{T}$ and $B_0 = 50 \mu\text{T}$. The dotted line indicates the -3 dB bandwidth at $\approx 500 \text{ Hz}$. The data is acquired using a spectrum analyzer and a random-noise-fed pancake coil. Figure adapted from [Jau20b].

Next, the region of linear OPM response was estimated. At a fixed background magnetic field B_0 , and thus at a fixed Larmor frequency f_L , the OPM laser chopping frequency was swept over a range of $f_L \pm 3.5$ kHz corresponding to $B_0 \pm 1$ μ T. The raw LIA-Y and LIA-magnitude (LIA-R) data are depicted in Figure 2.14. Each of the measured LIA-Y transfer functions was used to convert the LIA-output to an equivalent magnetic field. While the region of linear response depends on the background magnetic field, only sensor data within a region of ± 200 Hz or ± 57 nT, respectively, was used for the MNP relaxation fits, while still keeping in mind the sensor bandwidth.

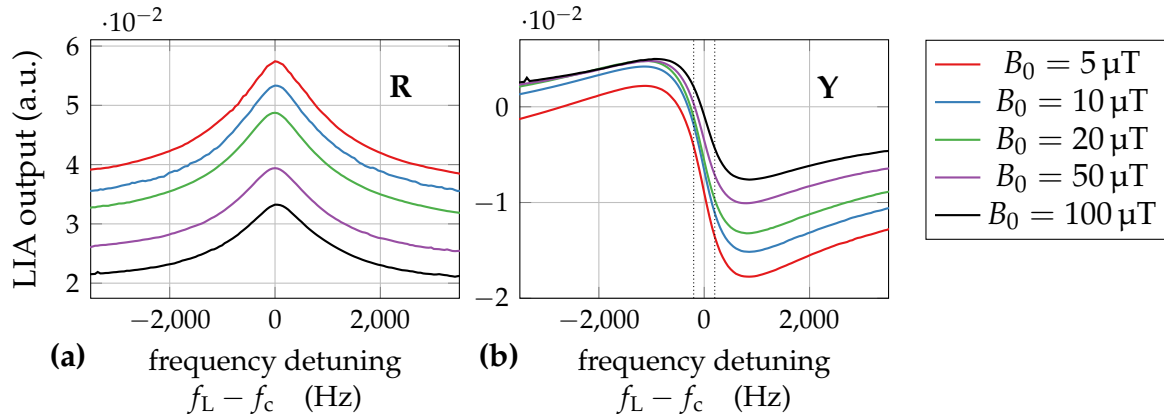


Figure 7.12: OPM resonances. Cesium resonances, acquired with the lock-in amplifier at different background magnetic fields. (a) Magnitude (LIA-R), (b) quadrature component (LIA-Y); The frequency axes are centered at the Larmor frequency. The region of linear Y-response used for data analysis is marked by black dotted lines. Figure adapted from [Jau20b].

Estimation of relaxation parameters: Dependence of liquid MNP's relaxation behavior on background magnetic fields First, the sample of liquid 100 nm MNP was positioned in the system. Then, the excitation coil was pulsed (200 ms, 1 mT) and the relaxation of the MNP was measured. This was repeated at different background magnetic field strengths. As it can be seen in Fig. 7.13a, the relaxation curve is changing in dependence of the B_0 field modulus. Regarding the excitation pulse direction with respect to the B_0 field, a parallel and an antiparallel configuration was investigated. It should be noted that the direction of the B_0 field was kept constant during the whole experiment, but instead the excitation pulse direction was flipped. When investigating the raw OPM signals, care must be taken of the nonlinear OPM response and the limited OPM bandwidth. Therefore, for this configuration the first 10 ms of data were clipped. The estimated relaxation parameters are shown in Fig. 7.14. It can be seen that for both, parallel and antiparallel excitation, the relaxation amplitude decreases with an increase of the background magnetic field. In contrast, the integral relaxation time decreases for antiparallel background magnetic fields, whereas it increases for parallel background magnetic fields. To emphasize the different relaxation-dynamics for parallel and antipar-

allel excitation, a selected set of amplitude-normalized relaxation signals is depicted in Fig. 7.13b.

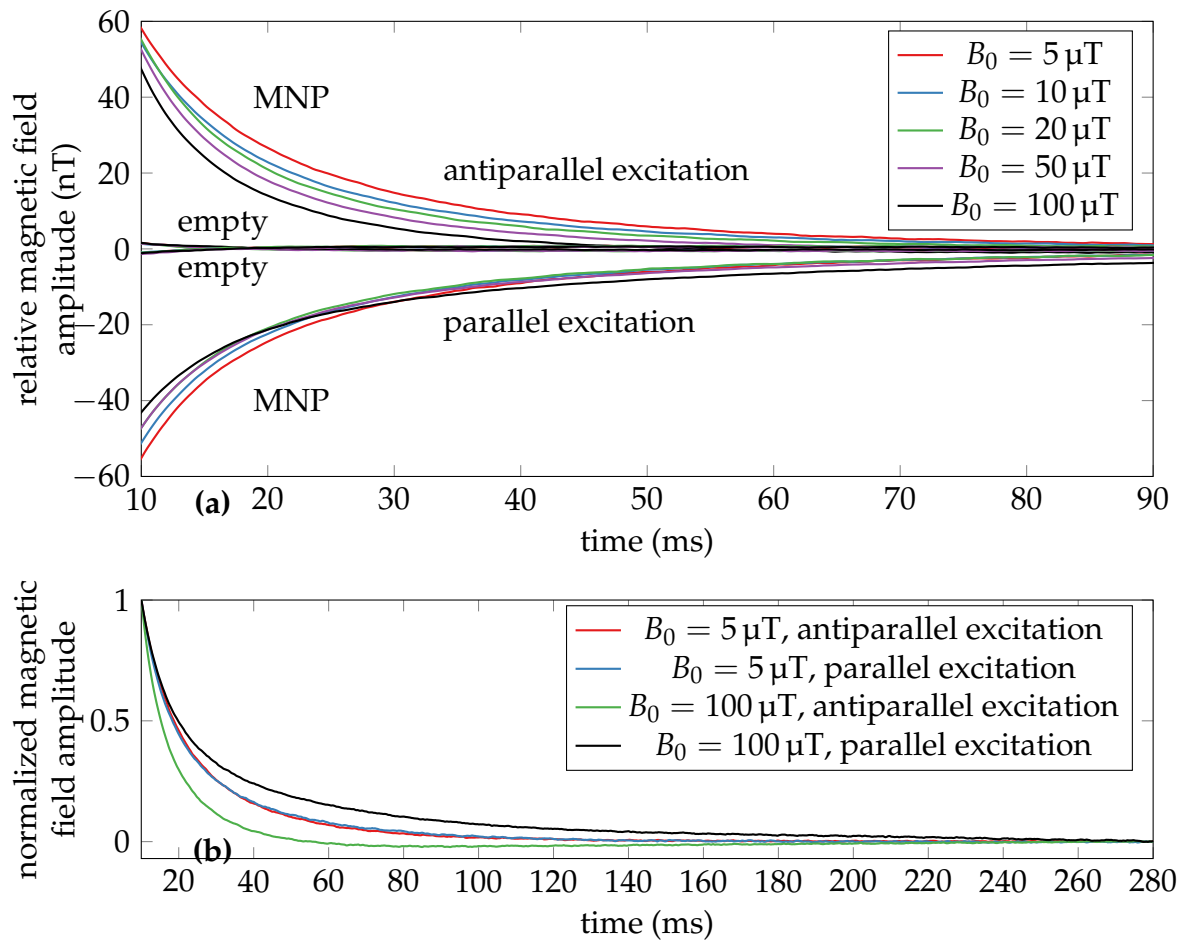


Figure 7.13: (a) MRX of liquid MNP with parallel and antiparallel excitation fields with respect to the background magnetic fields. The data is acquired with the OPM, 1 kHz lowpass filtered and seven-times averaged. (b) Amplitude-normalized relaxation signals. Figure adapted from [Jau20b].

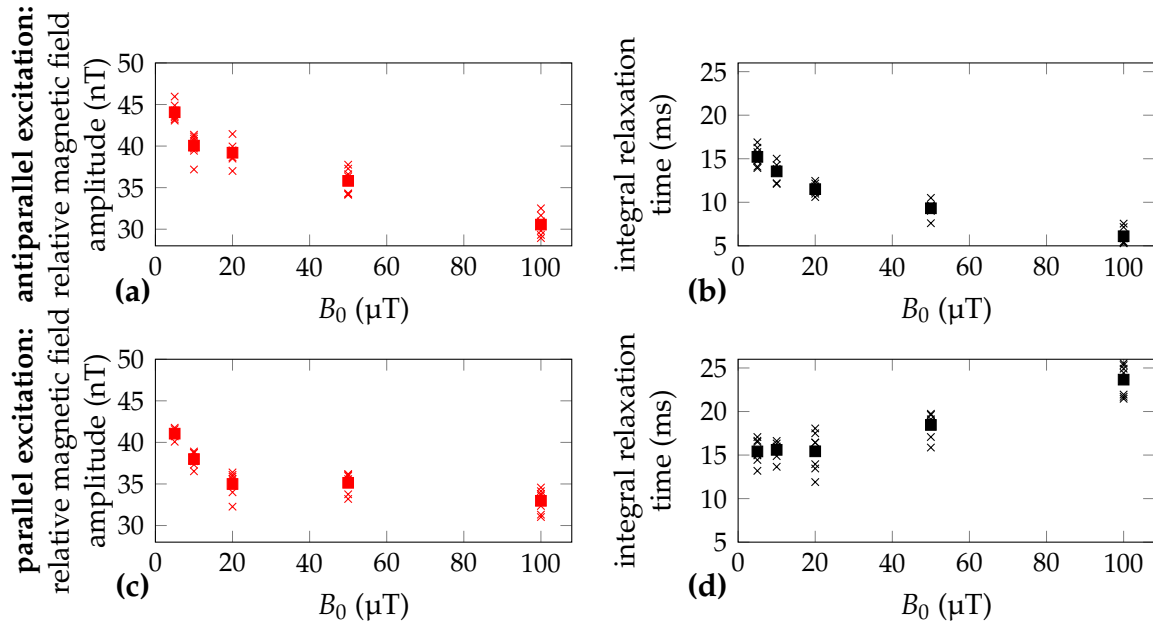


Figure 7.14: Relaxation amplitudes and integral relaxation times of liquid MNP at different background magnetic fields. Antiparallel excitation (a,b) and parallel excitation (c,d). Crosses indicate results for unaveraged data, squares indicate results for seven-times averaged data. Figure adapted from [Jau20b].

Estimation of relaxation parameters: Dependence of immobilized MNP's relaxation behavior on background magnetic fields

The immobilized MNP sample was positioned in the system and the MNP relaxation was measured after pulsing the excitation coil. This was repeated at different background magnetic field strengths. Fig. 7.15 shows data averaged from three measurement cycles and the estimated relaxation parameters are depicted in Fig. 7.16. It can be seen that the relaxation amplitude is decreased for parallel excitations, when increasing the background magnetic field. For antiparallel excitations, the amplitude varies only by a few percent. The integral relaxation time is increased and decreased for antiparallel and parallel excitations, respectively, when increasing the background field.

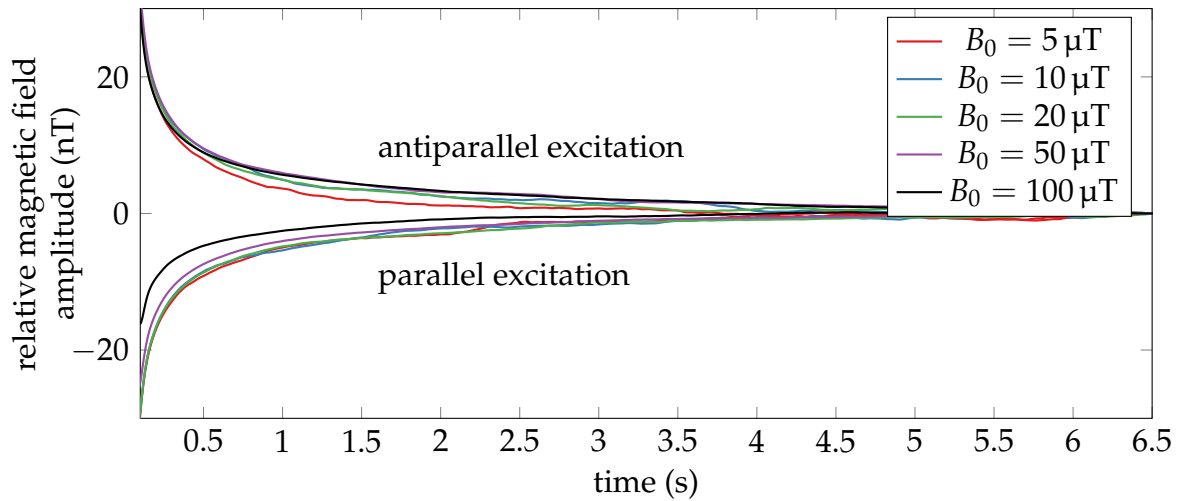


Figure 7.15: MRX of immobilized MNP at different background magnetic fields. The excitation field is applied parallel and antiparallel with respect to the background magnetic field. The data is acquired with the OPM, 100 Hz lowpass filtered and three-times averaged. Figure from [Jau20b].

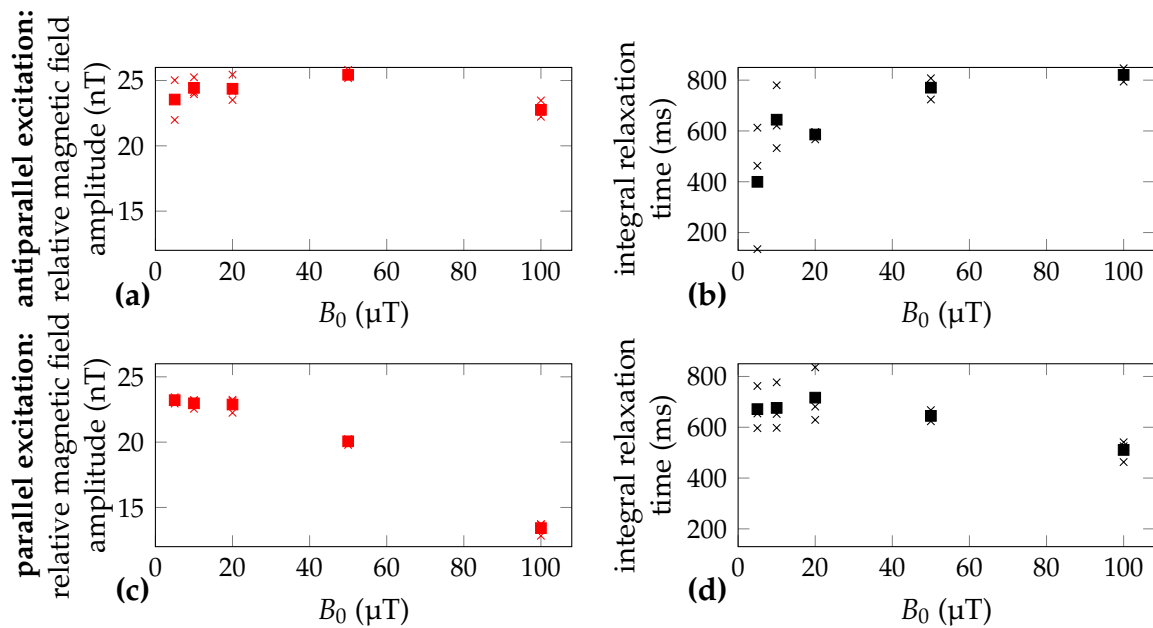


Figure 7.16: Relaxation amplitudes and integral relaxation times of immobilized MNP at different background magnetic fields. Antiparallel excitation (a,b) and parallel excitation (c,d). Crosses indicate results for unaveraged data, squares indicate results for three-times averaged data. Figure from [Jau20b].

7.4.4 Discussion

In this study it was shown, that MRX at DC background magnetic fields up to $100\ \mu\text{T}$ can be investigated with OPM. The current OPM showed a noise floor of $500\ \text{fT}/\sqrt{\text{Hz}}$ and was limited by excess laser intensity noise. In previous detailed studies by the Leibniz IPHT of a similar OPM, suppression of the excess intensity noise by a factor of 3 was achieved by subtraction of a reference photodiode signal [Sch12]. This could be implemented in the future. Regarding MRX parameters, it was observed that they alter significantly when applying background magnetic fields. By increasing the antiparallel background magnetic field from $5\ \mu\text{T}$ to $100\ \mu\text{T}$, the integral relaxation time decreased by 60 % (from 15.2 ms to 6.1 ms) in the liquid MNP sample. In the parallel configuration, the integral relaxation time increased from 15.4 ms to 23.7 ms, which corresponds to an increase of 54 %. This decrease of the integral relaxation time for antiparallel excitation and the increase of the integral relaxation time for parallel excitation are in good agreement with the literature: As calculated by Deissler et al. [Dei14], the magnetic energy density (for Néel and Brownian relaxation combined) of MNP for parallel fields decreases, while it increases for antiparallel fields, respectively. The magnetic energy density is proportional to the relaxation time [Dei14].

Regarding the relaxation amplitude, three counteracting effects have to be considered. Firstly, the effectively applied excitation field is increased or decreased by the background magnetic field. It is well known that the relaxation amplitude increases linearly with an increase of the excitation field (for excitation fields up to several mT) [Sar11]. Secondly, due to the extraction of the relaxation amplitude at two fixed time points, this parameter is coupled with the integral relaxation time. Thirdly and finally, the background magnetic field, if applied parallel to the excitation field, prevents some MNP from relaxing. In the liquid MNP sample, the absolute value of the relaxation amplitude decreases by 31 % or 20 % by increasing the background magnetic field for antiparallel or parallel excitation, respectively.

For the MNP response in the immobilized sample, the partially non-monotonical response of the extracted parameters to the background magnetic field may be explained by considering the non-homogeneous size distribution in the sample. As Coffey et al. [Cof95] emphasize, the influence of the parameter h (cp. Equation 2.2) depends strongly on the energy barrier height of the Néel relaxation. Therefore, by increasing the background magnetic fields, the different size fractions in the MNP sample behave differently. According to the previously mentioned particle size effect study it is likely that hereby the MNP relaxation shape and as a consequence thereof the integral relaxation time changes. The integral relaxation times of the liquid MNP sample were below 30 ms and the integral relaxation times of the immobilized MNP sample were in the region of several 100 ms. While the immobilized sample was governed by Néel relaxation only, in the liquid sample both Néel and Brownian relaxation occurred. In view of the different time scales for the two types of samples, one might be inclined to neglect Néel relaxation in the liquid samples. However, this is only reasonable if Brownian and Néel relaxation can be considered to be uncoupled phenomena, but different groups have shown that in fact they are not [Dei14, Shl94]. As a consequence, modeling and experimental characterization practice

has to take both effects into account in most cases. Improved understanding in mechanisms affecting Néel and Brownian relaxation in different ways, like, e.g., orientation and strength of static magnetic fields, may help to disentangle intricate MNP dynamics. The importance of the interplay of the relaxation mechanisms is substantiated, e.g., by the study of Dolgovskiy et al. [Dol15], where it has been shown that small variations in the MNP diameter distribution might have a big impact on the measurement results obtained by MRX.

To sum up, MRX at background fields is feasible and paves the way towards unshielded measurements. The background magnetic field has a significant influence on the relaxation of the MNP and needs to be considered thoroughly. With the current results, novel MRX imaging strategies, i.e., novel spatial encoding schemes where background magnetic fields are exploited as an additional parameter, are envisioned. This is the matter of future research.

7.5 MNP alignment measurement with an OPM

7.5.1 Introduction and Objectives

While MRX at different background magnetic fields is investigated in the previous section, also the alignment of the MNP’s magnetic moments with the excitation magnetic field may be of interest for various applications. Especially for MRX imaging, it is desired to measure both, the alignment and relaxation of the MNP’s magnetic moments, to reduce the data acquisition time or to improve the ill-posed inverse problem. In this section, a novel OPM operation mode will be developed and exploited to measure the relaxation, as well as the alignment of MNP’s magnetic moments. It should be noted, that the work from [Jau21] is reported here with partial modification.

7.5.2 Materials and Methods

For this experiment, the hardware presented in the previous Section (Section 7.4.2) was adapted, while the same liquid MNP sample was used. The background magnetic field was set at $5\ \mu\text{T}$. A $65\ \mu\text{T}$ magnetic field was switched periodically (at $0.1\ \text{Hz}$) using a commercially available current source (CS580 from Stanford Research Systems). It should be noted, that this current source was selected, because in contrast to conventional MRX measurements, here a current source with very low noise is required. The static field and the excitation field were applied antiparallel to each other, resulting in a field of $60\ \mu\text{T}$ for alignment, and $5\ \mu\text{T}$ for relaxation. A novel approach, the “bi-chromatic intensity modulation”, is presented here: The center of the sensitive range of the sensor is set by the laser chopping (and thus lock-in amplifier) frequency f_c , which corresponds to a Larmor frequency at a specific magnetic field amplitude. To obtain a sensitivity at both magnetic field levels, a bichromatic signal was applied to the intensity modulator, chopping the light at two frequencies corresponding to the Cs vapor Larmor frequency during alignment and relaxation of MNP’s magnetic moments, respectively. The pho-

todiode signal was demodulated with two time synchronized LIA at each individual reference frequency.

7.5.3 Results

In Figure 7.17 it can be seen that one of the LIA detects the relaxation (top of the figure), while the other one (bottom of the figure) detects the alignment of the MNP's magnetic moments. Both signals were analyzed separately in the time intervals ranging from 2 ms to 18 ms. The relaxation amplitude and the integral relaxation time were estimated as $B_R = 3.7$ nT and $T_R = 9.75$ ms, respectively, while the alignment amplitude and the integral alignment time were estimated as $B_A = 3.1$ nT and $T_A = 8.56$ ms, respectively. Thus, the integration time and the amplitude decreased with increased magnetic field.

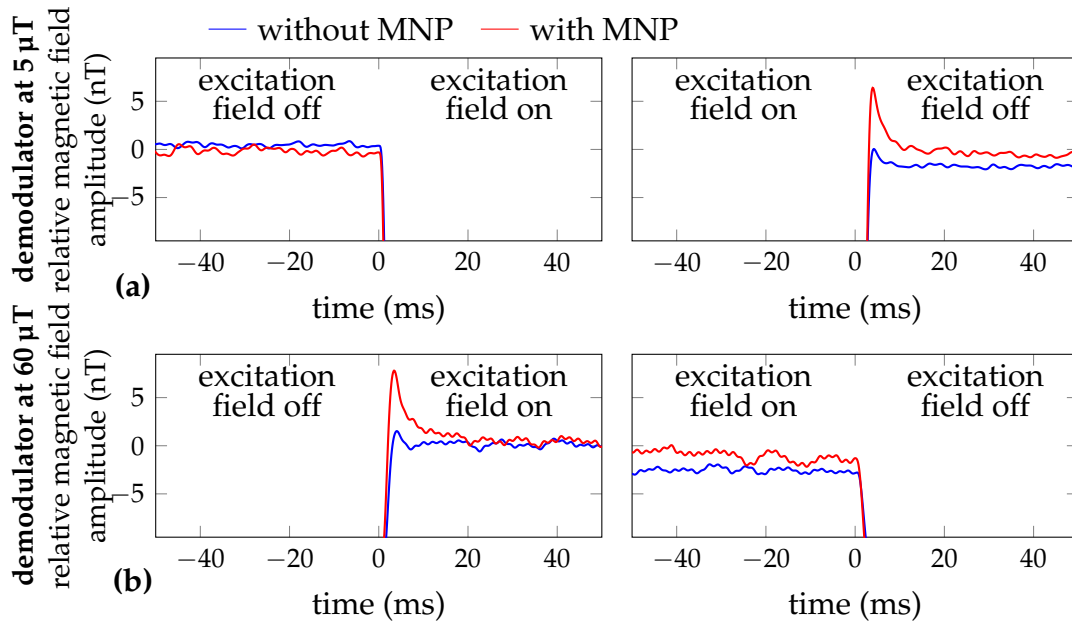


Figure 7.17: MRX and inverse MRX with bichromatic chopping and dual-demodulation OPM. Amplitude scaled raw data of (a) LIA1 at 18.8 kHz and (b) LIA2 at 216.8 kHz. Empty measurement in blue, measurement with MNP in red. The data is not averaged. Figure from [Jau20b].

7.5.4 Discussion

In principle, the intensity modulated OPM can be operated at background fields ranging from a few microtesla, up to at least 100 μ T. The dynamic range is limited to the resonance width (see Section 7.4.3 for details), resulting in a usable dynamic range of about 100 nT. The center of the dynamic range is defined by the chopping frequency, with which the laser is modulated. A well known method to extend the dynamic range is to integrate a feedback-loop of the chopping frequency, keeping it always on reso-

nance [Sch05, Leb20]. With this technique, the bandwidth of the system can be increased [Sch05], at the cost of linearly increasing noise with the frequency (see also Section 7.2). Applying a feedback-loop comes with the need of a careful fine-tuning, to guarantee system stability and sufficient speed. In MRX measurements, it might be challenging to disentangle the response, especially the transient signals after switching-off the excitation field, of such a sensor and the response of the MNP. This is the reason we came up with the solution prevented above, which is simple and very robust. With this novel setup, it is possible to monitor the relaxation and the alignment of the MNP's magnetic moments. The relaxation is measured at $5\ \mu\text{T}$ and the alignment is measured at $60\ \mu\text{T}$. The integral time and amplitude decrease with increased magnetic field. This is in accordance to the theory [Dei14, Die16] and the other measurement results for antiparallel excitation (see Section 7.4.4).

7.6 Summary

By using the OMG from Twinleaf, the bandwidth could be successfully increased to 100 kHz. Moreover, the OPM bandwidth can be controlled adaptively, enabling an efficient tradeoff with sensitivity. For the fast initial parts of a relaxation, a high bandwidth can be selected while for the latter parts of a relaxation, the sensitivity can be increased by selecting a smaller bandwidth. By exploiting synchronized pulsed optical pumping, the MRX system dead time could be reduced from more than 20 ms (see the QZFM measurements in Section 6.2) to $65\ \mu\text{s}$, which is composed of $28\ \mu\text{s}$ coil switch off time, $22\ \mu\text{s}$ pumping time and $15\ \mu\text{s}$ of data initially discarded during data analysis. These two achievements enable the detection of fast relaxing MNP with OPM-MRX (see next Chapter). The limit of the applied excitation field was also investigated using the OMG. It was found, that up to 100 mT fields, limited by the coil driver, can be applied without irreversible effects. With this setup it was possible to observe nonlinear MNP parameters, which allows for an improved characterization of MNP with MRX. The possibility to measure after strong magnetizing pulses also suggests, that OPM are robust enough to be combined with a magnetic hyperthermia setup, where AC magnetic fields in the 25 mT region are used (see Section 2.1). Still, this needs to be explicitly shown in future research. By using an intensity modulated OPM from Leibniz-IPHT Jena it was shown for the first time, that MRX at background magnetic fields from $5\ \mu\text{T}$ up to $100\ \mu\text{T}$ is possible. The relaxation parameters of MNP are significantly altered when applying background magnetic fields. This has two consequences: First, it possibly enables the development of novel spatial encoding techniques by applying background magnetic fields on purpose. Second, it is now known, that these effects need to be considered in unshielded measurements. With a modified OPM-MRX setup, by exploiting a novel, custom developed bi-chromatic intensity modulation, it was shown, that not only the relaxation, but also the magnetization of MNP can be monitored. For biomedical applications in clinics, this means a possible twofold reduction of examination time in MRXI. In consequence, this would increase patient comfort.

8 Unshielded OPM-MRX

8.1 Objectives

Given the reduction in OPM dead time after switching-off the excitation field, the detection of fast relaxing MNP might be possible. This enables MRX(I) to assist a broader range of biomedical applications, e.g. magnetic fluid hyperthermia. Practically, having a shorter dead time implicates not only, that fast particles can be detected at all, but also that a larger range of MNP diameters contributes to the measured MRX signal, improving the SNR. A high bandwidth and sample rate is not only a requirement for such measurements, but also justifies the formation of software gradiometers to reduce environmental noise. The possibility of performing unshielded measurements would drastically facilitate the use of MRX in real world scenarios. The requirement for an unshielded OPM-MRX setup is the quantification of MNP down to clinically relevant iron amounts of a few milligram, similar to the detection limit achieved in Section 6.2 for slowly relaxing MNP in a well shielded environment. Here, it is studied, if OPM-MRX of fast relaxing MNP in an unshielded environment is feasible, and which limitations arise.

8.2 Materials and Methods

Setup overview The setup again consists of an OMG from Twinleaf and an excitation coil. The MNP samples were placed - one at a time - between the excitation coil and the OMG (Figure 7.1). The center of the sample was located at a distance of 9.5 mm from the center of the first magnetometer channel.

MNP For this experiment BNF-Dextran MNP with a hydrodynamic diameter of 80 nm were used. A dilution series with a sample volume of 100 μL was prepared. The MNP were diluted with distilled water. The dilution factors ranged from 1:1 to 1:1000, resulting in iron amounts of 1.37 mg down to 1.37 μg (Table 8.1). Additionally, two liquid 100 μL samples filled with Perimag were prepared. The dilution factors were 1:1 and 1:10, resulting in iron amounts of 850 μg and 85 μg . While Brownian relaxation and Néel relaxation occur in parallel, for the liquid MNP used here, Brownian relaxation is dominant. In addition to the liquid samples, one immobilized sample was prepared. 50 μL BNF particles are immobilized by the addition of gypsum, resulting in a total sample volume of 100 μL .

MRX procedure, gradiometric measurement and Main's suppression For the MRX experiment, one sample was placed between the OPM and the coil. Then, the coil was

pulsed with a current of 1.1 A. To separate the MRX signals from the environmental magnetic field fluctuations, the two magnetometer channels of the OMG were used to form a software gradiometer. The baseline was 2.3 cm. To further reduce the influence of Main's noise, the MRX sequence length was selected as 30 ms, composed of 10 ms of excitation time and 20 ms of relaxation time. With this selection, two consecutive MRX sequences are exactly out of phase with respect to 50 Hz noise and odd harmonics. Since the Main's frequency is not exactly 50 Hz, the noise reduction would benefit from a continuous measurement of the current frequency. However, this was not implemented here. It should be noted, that with this averaging technique, even harmonics will constructively interfere. Usually, even harmonics are less pronounced than odd ones. To further increase the SNR, the MRX sequences are 100-times averaged. For the immobilized sample, a different MRX sequence was selected. The excitation time was 1 s, and the relaxation was measured for several seconds. The measurements were not phase-aligned with the Main's 50 Hz, but they were 88-times averaged.

8.3 Results

In Figure 8.1, the raw FPGA data of an unshielded MRX-measurement of BNF-MNP (sample with dilution factor 1:20) is shown. The 50 Hz and harmonics perturbations are clearly visible on the single magnetometer channels and are well suppressed with the gradiometric arrangement. A further suppression is reached by averaging. After 100-times averaging and subtracting the mean of 100 empty measurements, the resulting MNP relaxation signals were fitted to the double-exponential model (Equation 2.6). The FPGA data and the corresponding fits of the dilution series are depicted in Figure 8.2a. The first FPGA data point is at 0.466 ms after the switch-off of the excitation coil, which is the center of the usable free-precession decay signal. The obtained fit parameters are summarized in Table 8.1. It should be noted that the static gradient O corresponds to the remanence of the MNP [Bau08]. The relation between iron concentration and ΔB of the BNF particles can be described by a linear function with $R_{\text{adj}}^2 = 0.99$. The increase of the relaxation time $t_{1/e}$ for higher iron concentrations might be due to the resulting increase in viscosity in the samples and interparticle effects [Ebe06]. The increase of $t_{1/e}$ for the highly diluted samples might be due to a higher concentration of partially diluted dextran in the samples and therefore the formation of aggregates [Ebe06]. The presence of aggregates is supported by the amplitudes and relaxation times obtained by the double exponential fits (Table 8.1), where a considerably high second fraction of slower signal contributions is found.

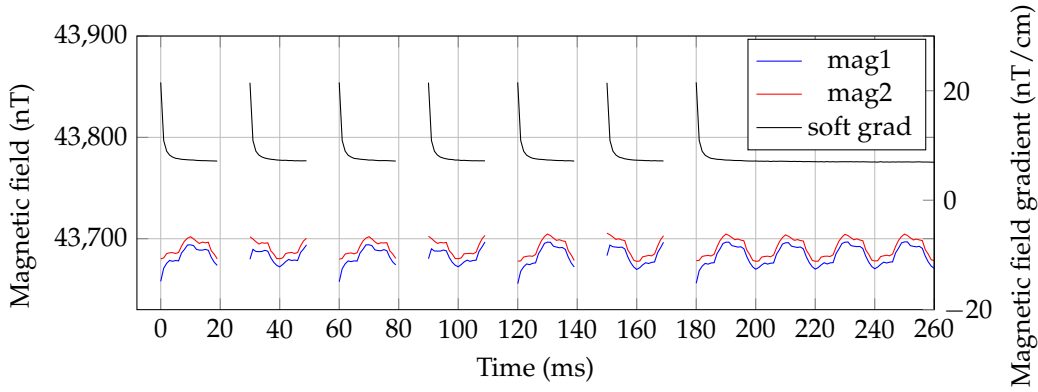


Figure 8.1: Unshielded OPM-MRX measurements of BNF-MNP (sample with dilution factor 1:20). The excitation coil is on when no FPGA data is available, e.g., in the time span from 20 ms to 30 ms. The FPGA data is not averaged. Figure from [Jau21].

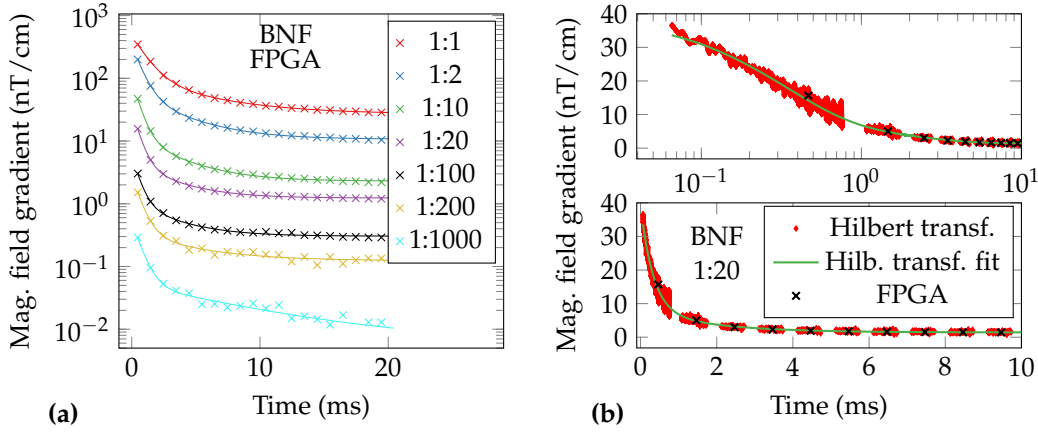


Figure 8.2: Unshielded gradiometric OPM-MRX measurements of a BNF-MNP dilution series. The excitation coil is switched off a few μs before the timestamp 0s. The gradiometric data is 100-times averaged and an averaged empty measurement is subtracted. Individual FPGA-data-points are indicated by crosses, solid lines are the corresponding exponential fits (compare Tab. 8.1). (a) FPGA data. (b) FPGA data and instantaneous magnetic field obtained via Hilbert transform of 1:20 BNF sample; top: logarithmical time axis, bottom: linear time-axis. Figure from [Jau21].

The estimated relaxation time $t_{1/e}$ can be used to calculate a theoretical monodisperse diameter of the MNP (Equation (2.3)). A sample viscosity equal to that of water is assumed. For the 1:20 diluted BNF particles, the relaxation time of 0.62 ms corresponds to a monodisperse diameter of 117 nm, which is in good agreement with the literature [Rem15]. The fit values of the Perimag[®] MNP (Table 8.1) are left as reference.

The 1:10 diluted Perimag[®] sample's relaxation time of 1.08 ms corresponds to a monodisperse diameter of 140 nm, which is close to the nominal value from the datasheet 130 nm.

In Figure 8.2b the averaged FPGA-data of the 1:20 diluted BNF-sample is plotted together with the instantaneous magnetic field as estimated via Hilbert transform and a fit to the double exponential relaxation model (Equation 2.6). The estimated fit parameters are shown in Table 8.1. The Hilbert transform data shown is 100-times averaged and a mean of 100 empty measurements is subtracted. It can be observed, that the high sample rate estimation of the magnetic field obviously suffers from higher noise than the FPGA data, but offers the possibility of examining the MNP's relaxation with high time resolution. It is noticeable that the time series data of FPGA and Hilbert transform match very well, except for the first FPGA sample. This is explained by the fact that the FPGA gives a single measurement of the magnetic field over an entire shot, while the magnetic field changes nonlinearly within the first millisecond. The relaxation amplitudes ΔB obtained by the FPGA and the Hilbert transform match. It can be observed that generally shorter relaxation times $t_{1/e}$ are obtained from the Hilbert transform data than from FPGA data. For example, the relaxation time of the 1:20 diluted BNF sample is 0.42 ms, as obtained via Hilbert transform. This corresponds to a monodisperse diameter of 103 nm. Like described before, for the FPGA data a monodisperse diameter of 117 nm is obtained. This confirms that also smaller MNP fractions are detected using the Hilbert transform approach. The estimated relaxation parameters for the other samples are summarized in Table 8.1. While the fits for samples with lower concentration are still good for the FPGA data, the coefficient of determination R_{adj}^2 of the fits to the Hilbert transform data decreases. This is due to the degradation of the signal-to-noise ratio for low concentrations. For this reason, the fit parameters of the 1:1000 sample are not reported.

Table 8.1: Estimated relaxation amplitudes ΔB , relaxation times $t_{1/e}$ and fit parameters for double exponential fits (Equation 2.6) to relaxation curves of liquid BNF MNP and Perimag[®] MNP (Peri).

data from	MNP type	dilution factor	Fe (μg)	ΔB (nT/cm)	$t_{1/e}$ (ms)	B_1 (nT/cm)	τ_1 (ms)	B_2 (nT/cm)	τ_2 (ms)	O (nT/cm)	R_{adj}^2
FPGA	BNF	1:1	1370	321.23	1.35	72.57	5.20	389.62	1.10	26.98	1.00
FPGA	BNF	1:2	685	189.21	0.84	45.51	3.51	290.86	0.70	10.71	1.00
FPGA	BNF	1:10	137	44.89	0.64	9.58	3.25	84.19	0.56	2.30	1.00
FPGA	BNF	1:20	68.5	14.44	0.62	3.19	3.05	27.90	0.54	1.23	1.00
FPGA	BNF	1:100	13.7	2.73	0.64	0.74	3.09	4.98	0.54	0.30	1.00
FPGA	BNF	1:200	6.85	1.40	0.72	0.23	4.39	2.48	0.64	0.12	1.00
FPGA	BNF	1:1000	1.37	0.28	0.75	0.05	8.62	0.49	0.65	0.01	1.00
HT	BNF	1:1	1370	265.18	0.18	298.19	1.94	1214.60	0.13	33.42	0.99
HT	BNF	1:2	685	164.52	0.35	120.89	1.86	457.98	0.25	12.00	1.00
HT	BNF	1:10	137	39.68	0.42	21.98	1.81	95.46	0.32	2.64	1.00
HT	BNF	1:20	68.5	12.77	0.42	7.00	1.78	31.17	0.32	1.41	0.99
HT	BNF	1:100	13.7	2.43	0.42	1.52	1.76	5.68	0.31	0.28	0.61
HT	BNF	1:200	6.85	1.25	0.42	0.65	1.92	3.05	0.33	0.10	0.31
FPGA	Peri	1:1	850	132.99	1.43	66.40	4.88	128.91	0.81	30.72	1.00
FPGA	Peri	1:10	85	16.07	1.08	6.86	4.74	19.18	0.70	3.28	1.00
HT	Peri	1:1	850	124.23	0.73	54.94	4.97	191.99	0.49	30.78	1.00
HT	Peri	1:10	85	14.96	0.69	9.06	3.56	22.24	0.40	3.44	0.99

When detecting slowly relaxing MNP in an unshielded environment, the drift of the background magnetic field is a main problem. Here, this challenge is successfully addressed by the short baseline of the magnetometer. The 88-times averaged, unshielded MRX measurement of BNF-MNP embedded in gypsum is shown in Figure 8.3, together with the fit of the moment superposition model (Equation 2.7) and a single-exponential fit for reference.

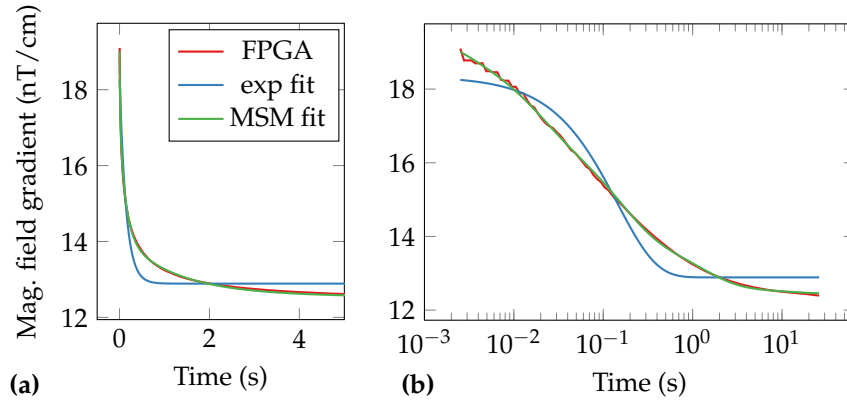


Figure 8.3: Unshielded gradiometric OPM-MRX of BNF-MNP embedded in gypsum, acquired at a sample rate of 1 kHz. The iron amount of the sample is 685 μg . The data is 88-times averaged and no empty measurements are subtracted. Linear time-axis (a) and logarithmical time axis (b). Figure from [Lebed].

8.4 Discussion

Previously presented OPM-MRX experiments and experimental OPM-MRX studies in literature [Joh12, Dol15, Baf19] were limited by OPM dead time and bandwidth, which prevented from performing MRX on fast relaxing samples, especially with commercially available sensors. In this study the benefit of a commercially available, pulsed OPM for MRX is demonstrated.

While the overall setup is, in principle, similar to the ones presented in Section 6.1 and Section 7.4, it employs field gradients and liquid MNP. The question about MNP motion might arise. While MNP in a strong magnetic field gradient exhibit directed motion, this is not the case here, since the applied gradients are at least one order of magnitude smaller than needed for a detectable motion.

In this experiment, an increase in relaxation time for highly diluted samples was observed. The same behavior was also observed in the quantification measurements using freeze dried MNP and a QZFM magnetometer (see Table 6.1).

One important aspect which should be investigated in detail in future work is the channel matching of the magnetometers, which defines the performance of the software gradiometer. Different pump and probe intensities, different temperatures and therefore different buffer gas pressures, different T_2 times and photodiode amplifier parameters will directly affect the gradiometer performance and must be studied in future work.

Another point of improvement, which was not focused on here, is the data processing of the relaxation curves. To enhance amplitude and time constant parameter estimation, adaptive filtering or resampling [Ebe06], or filtering and fitting in the Legendre space [Bao14] should be considered. The latter has the important advantage, that it does not introduce phase shifts like conventional filters.

With respect to the results of the immobilized MNP: The poor single-exponential fit

indicates a wide core diameter distribution of the MNP, which is expected due to the multi-core structure of the employed MNP and the immobilization method. In contrast, the MSM agrees well with the data. However, like stated before, fitting to the MSM is an ill-posed problem. Therefore, the solution of the parameters is not unique.

To sum up, with the commercially available pulsed OPM in its gradiometric arrangement, it is possible to acquire MRX signals of liquid MNP with relaxation times in the sub-millisecond region, in unshielded environments. The detection limit of the current setup is about $1.37 \mu\text{g}$ of iron for a liquid BNF-MNP-sample (Bionized NanoFerrite) with a volume of $100 \mu\text{L}$. The short baseline of the gradiometer also allows for unshielded measurements of slowly relaxing MNP, i.e., MNP embedded in gypsum, where usually slow environmental drifts compromise the signals.

9 Conclusion and Outlook

9.1 Conclusion

In this thesis, the high potential of OPM for MRX and MRXI was demonstrated. Our findings are a profound foundation for future OPM-MRXI research towards the combination of MRXI and biomedical applications.

The base of this study was the characterization of a commercially available SERF OPM from QuSpin, with respect to MRX. It was successfully demonstrated that these OPM are, in principle, suited for MRX and MRXI, while being mainly limited by bandwidth and dead time after switching off the magnetization pulses. Nevertheless, an iron detection limit of $\leq 5.8 \mu\text{g}$ iron was demonstrated for slowly relaxing MNP. This is an appropriate limit for clinical applications.

Our approach to translate MRX to MRXI was a two step process. In the first step, the OPM-MRX setup was extended with multiple excitation coils. In order to develop a setup with well controllable parameters, only a single OPM was used to avoid the problem of sensor crosstalk. A mathematical model of the geometric and magnetic properties was formulated for this setup. With the solution of the associated inverse problem, we finally achieved a 1D reconstruction of MNP distributions. In the second step, a multi-OPM setup was developed. The region of interest was 12 cm by 8 cm. The sensor crosstalk was identified to be neglectable at a sensor-to-sensor distance of > 3 cm. The sensors and coils were not placed on top and bottom of the phantom holder, which would be beneficial for the inverse problem. Instead, we opted for a placement around the phantom, with the vision of a future tomographic styled scanner. Here, we exploited that OPM can be freely positioned. Subsequently, we were able to precisely and accurately reconstruct point-like MNP distributions with clinically relevant iron concentrations with our novel 2D OPM-MRXI setup.

To exploit this achieved potential also when biomedical applications use fast relaxing MNP, the dead time of OPM needs to be drastically decreased, while increasing the bandwidth. For this reason, several OPM operation modes were investigated for MRX. With a pulsed free spin precession magnetometer, we reached a dead time in the range of a few microseconds. This was achieved by ultra short pump pulses and the synchronization of the pump pulses with the MNP excitation pulses. The original 1 kHz bandwidth of the pulsed OPM could be increased adaptively up to 80 kHz via instantaneous frequency retrieval using Hilbert transform. This comes with a tradeoff in sensitivity. It can be stated, that this operation mode is perfectly suited and currently the best operation mode for MRX.

This leads to the follow-up question regarding the upper limit of the excitation field

amplitude. While in SQUID-MRX usually excitation fields in the single digit millitesla range are used, we were able to increase the excitation field for in-place-magnetization of the MNP up to 100 mT. This enables performing OPM-MRX in the nonlinear MNP magnetization range, leading to an extended characterization of MNP and possibly a novel spatial encoding scheme in MRXI. Further, the ability of the OPM to withstand high magnetic fields and magnetic field gradients promises the use of OPM-MRX(I) in magnetic hyperthermia.

In another experiment we have shown, that not only the relaxation, but also the excitation of MNP can be monitored, eventually resulting in a twofold reduction of the examination time in MRXI.

Finally, we asked ourselves how to facilitate the use of MRX(I) in real world scenarios. One very challenging, but highly promising way would be the (partial) omission of magnetic shielding. A prerequisite is the possibility to measure relaxation signals at background magnetic fields. Further, it needs to be known, how background magnetic fields influence the MNP's relaxation behavior. It could be demonstrated using an intensity modulated OPM, that MRX at background fields up to (at least) 100 μ T is possible. The relaxation parameters are altered significantly and are in well accordance with the literature. The intended use of background magnetic fields could lead to additional spatial encoding schemes in MRXI.

OPM-MRX in an unshielded environment was successful due to the combination of different findings. The first prerequisite was the knowledge about the influence of background magnetic fields. Further requirements were the high adaptive bandwidth and short dead time of our pulsed free spin precession magnetometer. Additionally, we implemented a gradiometric detection scheme and main's synchronized averaging. With our novel portable tabletop system, we could demonstrate quantitative unshielded MRX measurements of fast relaxing, water suspended MNP. The outstanding detection limit was about 1.37 μ g of iron for a liquid BNF-MNP-sample (Bionized NanoFerrite) with a volume of 100 μ L.

9.2 New opportunities of OPM-MRXI for human applications

9.2.1 OPM-MRXI for human applications – glioblastoma imaging

In order to translate OPM-MRXI to human applications, the next (and currently running) step is to scale the MRXI setup up to human size. An OPM-MRXI setup covering the human head is envisioned. This setup could be used to quantitatively image MNP distributions in the brain, e.g. in a glioblastoma. This would be especially useful for the planning and post-observation of a magnetic hyperthermia treatment. Such a large scale MRXI setup has not been demonstrated yet, neither with SQUID nor OPM.

An exemplary system for the imaging of MNP targeted to a glioblastoma is shown in Figure 9.1. In this human head sized MRXI setup, the potential of flexible OPM positioning is exploited. The modular setup consists of three coil boards, where each hosts

between two and four zero field magnetometers (QZFM generation 2) from QuSpin. This results in a total magnetometer count of eight and a total magnetometer channel count of 16. Each coil board consists of 16 coils and is made from two stacked two-layer printed circuit boards. The boards combine small coils for high surface selectivity and large coils for detecting MNP in deep brain regions. Two additional OPM are mounted on the chest to measure magnetocardiography (MCG). The signal of these OPM could eventually be used to cross-check motion artifacts visible in the other channels.



Figure 9.1: Setup for proof of principle quantitative imaging of MNP in a glioblastoma. The setup consists of 48 excitation coils and 16 OPM channels. Four additional OPM channels are used to measure MCG simultaneously. The coil board on the chest is solely used for mounting the OPM.

In a first measurement, the OPM data was recorded without activating the excitation coils. It could be seen, that motion artifacts cannot be neglected, which is known for OPM based MEG measurements [Sey21]. This means, that either suppression techniques need to be integrated or that the setup and phantom/patient need to be well supported and kept in a still position. Further measurements and the investigation of achievable imaging parameters are the matter of current research.

Like stated at the beginning of this thesis, quantitative imaging of MNP distributions significantly improves treatment planning and monitoring [RR21, Fer21] and is a requirement to translate hyperthermia to clinics [Hea22]. If our novel imaging setup proves successful results, a profound foundation for effective treatments will be available.

9.2.2 OPM-MRXI in unshielded environments

Unshielded operation of MRXI would drastically facilitate the requirements for research groups and hospitals, since no magnetic shield would be required. Several challenges remain open with respect to OPM-MRXI measurements at background magnetic fields. One large issue is the change of relaxation parameters based on the amplitude and direction of the background magnetic field, like elaborated in Section 7.4. Luckily, when avoiding closeby ferromagnetic materials, the largest remaining background magnetic field source with microtesla field amplitudes is the Earth’s magnetic field, which can be

considered homogeneous or at most a first order gradient [Tie21]. When measuring the background magnetic field (gradient) with several reference magnetometers, the challenge lies in the modeling of the effects, especially if the target to examine contains MNP with an unknown diameter distribution. The second challenge for unshielded measurements is the background magnetic field drift due to elevators, underground railway and car traffic, and disturbances due to the mains. With their sub-microtesla amplitude, they are not expected to change the relaxation behavior, but need to be compensated before analyzing the relaxation data. Gradiometer based methods like shown in Section 8 have shown to be promising, besides advanced noise suppression techniques [Son09, Pyr21, Sey21]. A small region of interest will facilitate the noise suppression. To conclude, small scale OPM-MRXI in unshielded or moderately shielded environment might be principally feasible, but is challenging. It is the matter of future research to elaborate the proof of principle and to show if the reachable sensitivity is sufficient for biomedical applications.

Nomenclature

ANSD	Amplitude Noise Spectral Density
a.u.	arbitrary unit
BMSR-2	Berlin Magnetically Shielded Room 2, located at the PTB in Berlin
CT	Computer Tomography
FFT	Fast Fourier Transform
FPGA	Field Programmable Gate Array
FSP	Free Spin Precession
HT	Hilbert Transform (\mathcal{H})
LIA	Lock-In Amplifier
MCG	Magnetocardiography
MNP	Magnetic Nanoparticle(s)
MPI	Magnetic Particle Imaging
MRI	Magnetic Resonance Imaging
MRX	Magnetorelaxometry
MRXI	Magnetorelaxometry Imaging
MSR	Magnetically Shielded Room
OMG	OPM from Twinleaf (containing two pulsed magnetometers)
OPM	Optically Pumped Magnetometer(s)
PCB	Printed Circuit Board
QZFM	OPM from QuSpin
SERF	Spin Exchange Relaxation Free
SNR	Signal-to-noise ratio
SQUID	Superconducting Quantum Interference Device(s)

List of Figures

2.1	Relaxation time constants in dependence of core and hydrodynamic diameter. The MNP's shell thickness is selected as 10 nm, $T = 293.15$ K, $\kappa = 1 \times 10^4$ J/m ³ , $\tau_0 = 1 \times 10^{-9}$ s and $\eta = 0.01$ Pa s.	5
2.2	Basic principle of magnetorelaxometry. The external field B is shown in black. The MNP's net magnetic moment m is shown in red.	6
2.3	Exemplary MRX imaging setup composed of nine vectorial magnetometers (blue) and 36 excitation coils (red) arranged around a region of interest (grey), which is divided into voxels.	8
2.4	Basic operating principle of a SQUID magnetometer, measuring the external magnetic flux ϕ_{ext} . The SQUID signal is linearized using a flux locked loop (FLL), consisting of an amplifier, an integrator, a shunt resistor R and a coil, which feeds back a flux ϕ_{FB} , thus compensating ϕ_{ext} within the loop.	11
2.5	Exemplary steady state solutions of Bloch equations: (a) relaxed spin ensemble (yellow). (b) A circularly polarized pump laser (\vec{k}) is applied in z-direction, which polarizes individual spins, building up a collective spin \vec{S} (yellow). (c) In addition to optical pumping a small, constant magnetic field \vec{B} (green) is applied in x-direction. (d) Same as (c) , but with a larger \vec{B}	13
2.6	Exemplary transient solution of Bloch equations: (a) the spin ensemble (yellow) is polarized by optical pumping. (b, c, d) The pump laser is switched off and a moderate magnetic field \vec{B} (green) is applied, leading to spin precession over time. The macroscopic spin is exponentially damped (spin relaxation). (b) $t = 0$ (arbitrary unit), (c) $t = 20$ (a.u.), (d) $t = 42$ (a.u.).	13
2.7	⁸⁷ Rb ground state hyperfine structure and Zeeman substates. Not to scale.	14
2.8	⁸⁷ Rb ground state hyperfine splitting energy shifts with respect to the applied magnetic field. The data points of the plot were calculated using the Breit-Rabi formula (Equation 2.16).	16
2.9	(a) Energy probability distribution of a cloud of ⁸⁷ Rb atoms at zero magnetic field and without any electric field (light) applied. (b) D ₁ optical pumping with σ^+ light (blue). The pump laser linewidth is broad, so $F = 1$ and $F = 2$ are pumped. The relaxation via spontaneous emission (red) is indicated for one excited sublevel only. The atoms are pumped towards $F = 2$, $m_F = 2$	17

2.10	(a) Ground state energy levels split due to a magnetic field applied parallel to the quantization axis. (b) In addition to the parallel magnetic field, a field perpendicular to the quantization axis is applied, which couples the different energy levels.	18
2.11	SERF OPM setups as used in [All02, Kom03] (a) and in the QuSpin QZFM sensors [Os18] (b). Both setups also integrate a lock-in-amplifier together with an optical modulator or a magnetic modulation, which is not shown here.	20
2.12	Spin polarization with amplitude modulated light (a), frequency modulated light (b) and polarization modulated light (c). Pump direction (\vec{k}) is \vec{z} . Figure based on [Wei17].	21
2.13	Schematic of an intensity modulated OPM configuration as used in [Sch12, Jau20b]. With a function generator (fgen) and intensity modulator (IM), the linearly polarized light from the laser is pulsed at the Larmor frequency of the alkali atoms and converted into circular polarization by a $\lambda/4$ waveplate. The transmitted laser light is detected by a photodiode (PD), amplified by a current voltage converter with integrated preamplifier (I/U) and phase-sensitively demodulated with a lock-in amplifier (LIA).	22
2.14	OPM resonances. (a) Magnitude (R) and (b) quadrature component (Y), as acquired with a lock-in amplifier.	22
2.15	Schematic of a standard pump-probe-setup, which can be configured as a free-spin-precession magnetometer.	23
2.16	Vectorization of a scalar magnetometer using a lock-in-amplifier.	25
2.17	Simulation of the lock-in amplifier response (red) to a Lorentzian magnetometer transfer function (blue).	26
5.1	Schematic drawing of the pulsed optically pumped magnetometers (OPM), consisting of two pulsed magnetometers enclosed in a compact sensor head. Figure from [Jau21].	38
5.2	Schematic of a programmable, battery-powered current source. This device was used for experiments with the QZFM sensors and the intensity modulated OPM.	41
5.3	Schematic of a battery-powered current multiplexer and switch-off circuit. This device was used for experiments with the QZFM sensors. Figure from [Jau20a].	42
5.4	Schematic of a battery-powered excitation-coil driver with fixed current setting. The coil driver was used for experiments with the OMG (see Section 7.2). Figure from [Jau21].	43

6.1	(a) Schematic and (b) photography OPM-MRX setup for MNP quantification using a commercially available OPM within a well shielded environment (BMSR-2 at the PTB in Berlin). (c) Simulated magnetic flux density map of the planar excitation coil when supplied with a current of 1 A. Please note the logarithmic scaling of the axis. Figure adapted from [Jau20a].	47
6.2	Switch-off behavior of the zero field OPM (QZFM) from QuSpin. The excitation coil is switched off at timestamp zero. A small, approx. 22 pT magnetic field with a frequency of 28 Hz is constantly applied to the OPM.	48
6.3	(a) Raw relaxation data, measured with a single OPM for the dilution series. The data within the sensor dead time (gray) is not shown. (b) Relaxation amplitude fits with linear regression of iron concentration vs. relaxation amplitude. Figure from [Jau20a].	49
6.4	Setup for MNP quantification and quantitative 1D reconstruction. Schematic representation (a) and photo (b). Simulated magnetic field map (c) for the third (from left to right) activated excitation coil. Figure from [Jau20a].	52
6.5	1D reconstruction: ground truth and reconstruction for each magnetic nanoparticle (MNP) phantom. Point-like MNP phantoms in (a)–(e) and dilution series phantoms in (f) and (g). Figure from [Jau20a].	53
6.6	Setup for 2D MRX imaging. Schematic representation (a) and photo (b). Simulated magnetic field map (c) for the activated top-right excitation coil. Please note the logarithmic scaling of the axis. Figure from [Jau20a].	54
6.7	Singular values of the inverse problem of our 2D imaging setup. Figure from [Jau20a].	55
6.8	2D imaging: ground truth and reconstruction for each magnetic nanoparticle phantom. Figure from [Jau20a].	55
7.1	Portable tabletop OPM-MRX setup in unshielded laboratory environment. Figure from [Jau21].	58
7.2	(a) Unshielded raw OMG photodiode signal as output by the OPM electronics and recorded using an oscilloscope. (b) Amplitude noise spectral densities (ANSD) of the raw OMG analog output: normal operation (blue); pump laser always off (red); OMG unpowered (black). The data used for the calculation of the ANSD are recorded 100 μ s to 700 μ s after the pump pulse. Figure from [Jau21].	61
7.3	Amplitude noise spectral density (ANSD) of the unshielded OPM in a laboratory environment. The OMG is configured to pump for 22 μ s. The software gradiometer baseline is 2.3 cm. Figure from [Jau21].	62
7.4	Magnetometer amplitude response over OMG bandwidth for both magnetometer channels using Hilbert transform. Figure from [Jau21].	63

7.5	Unshielded magnetometer noise spectral densities using free-precession decay fits (brown), sliding window fits (green) and Hilbert transform (red). Unshielded gradiometer noise spectral densities using free-precession decay fits (green), sliding window fits (blue), Hilbert transform (black) and linear fit to the Hilbert transform (purple). Figure from [Jau21].	64
7.6	Coil current and OPM photodiode output. The optical pumping starts 28 μ s after initiating the coil shut-off. The signal distortion prior the pump pulses (i.e., periods -0.2 ms to 0 ms and 0.8 ms to 1 ms) is caused by the electrical heater of the OMG. Figure from [Jau21].	64
7.7	Unshielded OPM-MRX setup with possible MRX excitation fields of up to 100 mT. The battery powered notebook, the USB-oscilloscope and the OMG control electronics are visible on the upper part of the figure. The OMG's sensor head and the MRX excitation-coil are visible in the lower part of the figure. The position where the MNP sample is placed later is indicated by an arrow. The power amplifier is not visible, as it is located at a distance of about 3 m. Figure from [Jau21].	66
7.8	(a) FPGA-data of MRX of MNP embedded in gypsum at different excitation fields of up to 100 mT. The inset shows a zoom of the first 30 ms of the relaxations. Please note the different time scale of the figure and inset. The data were not averaged. (b) Pickup loop voltage during the shut-off of the different excitation fields. Figure from [Jau21].	67
7.9	MRX setup with OPM, MNP sample and MNP excitation coil (blue). The setup is housed in a magnetically shielded barrel. A three-axis Helmholtz coil system (not visible) within the shielding is used to generate the background magnetic field. Figure from [Jau20b].	69
7.10	OPM noise spectrum. Base noise of the OPM at different background magnetic fields from 5 μ T to 100 μ T, measured within a three layer magnetically shielded barrel. Figure adapted from [Jau20b].	71
7.11	Measured OPM frequency response at $B_0 = 5$ μ T and $B_0 = 50$ μ T. The dotted line indicates the -3 dB bandwidth at ≈ 500 Hz. The data is acquired using a spectrum analyzer and a random-noise-fed pancake coil. Figure adapted from [Jau20b].	71
7.12	OPM resonances. Cesium resonances, acquired with the lock-in amplifier at different background magnetic fields. (a) Magnitude (LIA-R), (b) quadrature component (LIA-Y); The frequency axes are centered at the Larmor frequency. The region of linear Y-response used for data analysis is marked by black dotted lines. Figure adapted from [Jau20b].	72
7.13	(a) MRX of liquid MNP with parallel and antiparallel excitation fields with respect to the background magnetic fields. The data is acquired with the OPM, 1 kHz lowpass filtered and seven-times averaged. (b) Amplitude-normalized relaxation signals. Figure adapted from [Jau20b].	73

7.14	Relaxation amplitudes and integral relaxation times of liquid MNP at different background magnetic fields. Antiparallel excitation (a,b) and parallel excitation (c,d). Crosses indicate results for unaveraged data, squares indicate results for seven-times averaged data. Figure adapted from [Jau20b].	74
7.15	MRX of immobilized MNP at different background magnetic fields. The excitation field is applied parallel and antiparallel with respect to the background magnetic field. The data is acquired with the OPM, 100 Hz lowpass filtered and three-times averaged. Figure from [Jau20b].	75
7.16	Relaxation amplitudes and integral relaxation times of immobilized MNP at different background magnetic fields. Antiparallel excitation (a,b) and parallel excitation (c,d). Crosses indicate results for unaveraged data, squares indicate results for three-times averaged data. Figure from [Jau20b].	75
7.17	MRX and inverse MRX with bichromatic chopping and dual-demodulation OPM. Amplitude scaled raw data of (a) LIA1 at 18.8 kHz and (b) LIA2 at 216.8 kHz. Empty measurement in blue, measurement with MNP in red. The data is not averaged. Figure from [Jau20b].	78
8.1	Unshielded OPM-MRX measurements of BNF-MNP (sample with dilution factor 1:20). The excitation coil is on when no FPGA data is available, e.g., in the time span from 20 ms to 30 ms. The FPGA data is not averaged. Figure from [Jau21].	82
8.2	Unshielded gradiometric OPM-MRX measurements of a BNF-MNP dilution series. The excitation coil is switched off a few μ s before the timestamp 0 s. The gradiometric data is 100-times averaged and an averaged empty measurement is subtracted. Individual FPGA-data-points are indicated by crosses, solid lines are the corresponding exponential fits (compare Tab. 8.1). (a) FPGA data. (b) FPGA data and instantaneous magnetic field obtained via Hilbert transform of 1:20 BNF sample; top: logarithmical time axis, bottom: linear time-axis. Figure from [Jau21].	82
8.3	Unshielded gradiometric OPM-MRX of BNF-MNP embedded in gypsum, acquired at a sample rate of 1 kHz. The iron amount of the sample is 685 μ g. The data is 88-times averaged and no empty measurements are subtracted. Linear time-axis (a) and logarithmical time axis (b). Figure from [Lebed].	85
9.1	Setup for proof of principle quantitative imaging of MNP in a glioblastoma. The setup consists of 48 excitation coils and 16 OPM channels. Four additional OPM channels are used to measure MCG simultaneously. The coil board on the chest is solely used for mounting the OPM.	89

List of Tables

3.1	Summary of commercially available, research grade OPM. Values reported here are taken from the manufacturer’s datasheet or homepage.	28
6.1	Estimated fit parameters for stretched exponential fits (Equation 2.8) to relaxation curves of freeze dried Resovist [®] MNP.	49
7.1	Estimated relaxation parameters ΔB , $t_{1/e}$ and offset O of relaxation curves with excitation fields ranging from 1 mT to 100 mT. The sample consists of gypsum-immobilized MNP with a total iron amount of 6.4 mg.	68
8.1	Estimated relaxation amplitudes ΔB , relaxation times $t_{1/e}$ and fit parameters for double exponential fits (Equation 2.6) to relaxation curves of liquid BNF MNP and Perimag [®] MNP (Peri).	84

Bibliography

- [AD18] E. Al-Dabbagh, J.-H. Storm and R. Körber. Ultra-sensitive SQUID systems for pulsed fields—degaussing superconducting pick-up coils. *IEEE Transactions on Applied Superconductivity*, 28(4):1–5, 2018.
- [Afa15] S. Afach, G. Ban, G. Bison, K. Bodek, Z. Chowdhuri, Z. Grujić, L. Hayen, V. Hélaine, M. Kasprzak, K. Kirch et al. Highly stable atomic vector magnetometer based on free spin precession. *Optics express*, 23(17):22108–22115, 2015.
- [Akb12] A. Akbarzadeh, M. Samiei and S. Davaran. Magnetic nanoparticles: preparation, physical properties, and applications in biomedicine. *Nanoscale research letters*, 7(1):1–13, 2012.
- [Ale92] E. B. Alexandrov and V. A. Bonch-Bruevich. Optically pumped atomic magnetometers after three decades. *Optical Engineering*, 31(4):711–717, 1992.
- [Ale95] E. Aleksandrov, M. Balabas, A. Vershovskii, A. Ivanov, N. Yakobson, V. Velichanskii and N. Senkov. Laser pumping in the scheme of an Mx-magnetometer. *Optics and Spectroscopy*, 78(2):292–298, 1995.
- [All02] J. C. Allred, R. N. Lyman, T. W. Kornack and M. V. Romalis. High-Sensitivity Atomic Magnetometer Unaffected by Spin-Exchange Relaxation. *Phys. Rev. Lett.*, 89:130801, 2002.
- [Ari77] E. Arimondo, M. Inguscio and P. Violino. Experimental determinations of the hyperfine structure in the alkali atoms. *Reviews of Modern Physics*, 49(1):31, 1977.
- [Att15] A. Attaluri, S. K. Kandala, M. Wabler, H. Zhou, C. Cornejo, M. Armour, M. Hedayati, Y. Zhang, T. L. DeWeese, C. Herman et al. Magnetic nanoparticle hyperthermia enhances radiation therapy: A study in mouse models of human prostate cancer. *International Journal of Hyperthermia*, 31(4):359–374, 2015.
- [Auz10] M. Auzinsh, D. Budker and S. Rochester. Optically polarized atoms: understanding light-atom interactions. Oxford University Press, 2010.
- [Baf19] O. Baffa, R. Matsuda, S. Arsalani, A. Prospero, J. Miranda and R. Wakai. Development of an optical pumped gradiometric system to detect magnetic

- relaxation of magnetic nanoparticles. *Journal of Magnetism and Magnetic Materials*, 475:533–538, 2019.
- [Bao14] G. Bao and D. Schild. Fast and accurate fitting and filtering of noisy exponentials in Legendre space. *PLoS One*, 9(3):e90500, 2014.
- [Bau08] D. Baumgarten, M. Liehr, F. Wiekhorst, U. Steinhoff, P. Münster, P. Miethe, L. Trahms and J. Haueisen. Magnetic nanoparticle imaging by means of minimum norm estimates from remanence measurements. *Medical & biological engineering & computing*, 46(12):1177, 2008.
- [Bau09] D. Baumgarten, M. Liehr and J. Haueisen. Imaging of magnetic nanoparticle loaded rat organs using a 16 channel micro SQUID system. In World Congress on Medical Physics and Biomedical Engineering, September 7-12, 2009, Munich, Germany, pages 366–369. Springer, 2009.
- [Bau10] D. Baumgarten and J. Haueisen. A spatio-temporal approach for the solution of the inverse problem in the reconstruction of magnetic nanoparticle distributions. *IEEE transactions on magnetics*, 46(8):3496–3499, 2010.
- [Bel57] W. E. Bell and A. L. Bloom. Optical detection of magnetic resonance in alkali metal vapor. *Physical Review*, 107(6):1559, 1957.
- [Bel61] W. E. Bell and A. L. Bloom. Optically driven spin precession. *Physical Review Letters*, 6(6):280, 1961.
- [Bia20] V. Biancalana, R. Cecchi, L. Stiazzini and A. Vigilante. Fast switching coil system for sample premagnetization in an unshielded ultra-low-field nuclear magnetic resonance experiment. *Review of Scientific Instruments*, 91(4):045119, 2020.
- [Bia21] G. G. d. A. Biasotti, A. G. Próspero, M. D. T. Alvarez, M. Liebl, L. A. Pinto, G. A. Soares, A. F. Bakuzis, O. Baffa, F. Wiekhorst and J. R. d. A. Miranda. 2D Quantitative Imaging of Magnetic Nanoparticles by an AC Biosusceptometry Based Scanning Approach and Inverse Problem. *Sensors*, 21(21):7063, 2021.
- [BJ63] W. F. Brown Jr. Thermal fluctuations of a single-domain particle. *Physical Review*, 130(5):1677, 1963.
- [Bog15] S. Bogren, A. Fornara, F. Ludwig, M. del Puerto Morales, U. Steinhoff, M. F. Hansen, O. Kazakova and C. Johansson. Classification of magnetic nanoparticle systems—synthesis, standardization and analysis methods in the nanomag project. *International journal of molecular sciences*, 16(9):20308–20325, 2015.

- [Bot18] E. Boto, N. Holmes, J. Leggett, G. Roberts, V. Shah, S. S. Meyer, L. D. Muñoz, K. J. Mullinger, T. M. Tierney, S. Bestmann et al. Moving magnetoencephalography towards real-world applications with a wearable system. *Nature*, 555(7698):657–661, 2018.
- [Bre31] G. Breit and I. Rabi. Measurement of nuclear spin. *Physical Review*, 38(11):2082, 1931.
- [Bro52] J. Brossel and F. Bitter. A New "Double Resonance" Method for Investigating Atomic Energy Levels. Application to Hg P 1 3. *Physical Review*, 86(3):308, 1952.
- [Bud00] D. Budker, D. Kimball, S. Rochester, V. Yashchuk and M. Zolotarev. Sensitive magnetometry based on nonlinear magneto-optical rotation. *Physical Review A*, 62(4):043403, 2000.
- [Bud05] D. Budker, L. Hollberg, D. F. Kimball, J. Kitching, S. Pustelny and V. V. Yashchuk. Microwave transitions and nonlinear magneto-optical rotation in anti-relaxation-coated cells. *Physical Review A*, 71(1):012903, 2005.
- [Bud07] D. Budker and M. Romalis. Optical magnetometry. *Nature physics*, 3(4):227–234, 2007.
- [Byr88] R. H. Byrd, R. B. Schnabel and G. A. Shultz. Approximate solution of the trust region problem by minimization over two-dimensional subspaces. *Mathematical programming*, 40(1-3):247–263, 1988.
- [Cha83] R. Chantrell, S. Hoon and B. Tanner. Time-dependent magnetization in fine-particle ferromagnetic systems. *Journal of magnetism and magnetic materials*, 38(2):133–141, 1983.
- [Cha20] P. Chandrasekharan, Z. W. Tay, D. Hensley, X. Y. Zhou, B. K. Fung, C. Colson, Y. Lu, B. D. Fellows, Q. Huynh, C. Saayujya et al. Using magnetic particle imaging systems to localize and guide magnetic hyperthermia treatment: tracers, hardware, and future medical applications. *Theranostics*, 10(7):2965, 2020.
- [Che08] B. Chertok, B. A. Moffat, A. E. David, F. Yu, C. Bergemann, B. D. Ross and V. C. Yang. Iron oxide nanoparticles as a drug delivery vehicle for MRI monitored magnetic targeting of brain tumors. *Biomaterials*, 29(4):487–496, 2008.
- [Chw19] A. Chwala, M. Schmelz, V. Zakosarenko, M. Schiffler, M. Schneider, M. Thürk, S. Bräuer, F. Bauer, M. Schulz, A. Krüger et al. Underwater operation of a full tensor SQUID gradiometer system. *Superconductor Science and Technology*, 32(2):024003, 2019.

- [Cio98] C. Ciofi, R. Giannetti, V. Dattilo and B. Neri. Ultra low-noise current sources. *IEEE Transactions on Instrumentation and Measurement*, 47(1):78–81, 1998.
- [Coe12] A. Coene, G. Crevecoeur and L. Dupre. Adaptive control of excitation coil arrays for targeted magnetic nanoparticle reconstruction using magnetorelaxometry. *IEEE transactions on magnetics*, 48(11):2842–2845, 2012.
- [Coe14] A. Coene, G. Crevecoeur, M. Liebl, F. Wiekhorst, L. Dupré and U. Steinhoff. Uncertainty of reconstructions of spatially distributed magnetic nanoparticles under realistic noise conditions. *Journal of Applied Physics*, 115(17):17B509, 2014.
- [Coe17] A. Coene, J. Leliaert, M. Liebl, N. Loewa, U. Steinhoff, G. Crevecoeur, L. Dupré and F. Wiekhorst. Multi-color magnetic nanoparticle imaging using magnetorelaxometry. *Physics in Medicine & Biology*, 62(8):3139, 2017.
- [Cof94] W. T. Coffey, D. Crothers, Y. P. Kalmykov, E. S. Massawe and J. Waldron. Exact analytic formula for the correlation time of a single-domain ferromagnetic particle. *Physical Review E*, 49(3):1869, 1994.
- [Cof95] W. Coffey, D. Crothers, Y. P. Kalmykov and J. Waldron. Constant-magnetic-field effect in Néel relaxation of single-domain ferromagnetic particles. *Physical Review B*, 51(22):15947, 1995.
- [Col19] S. Colombo, V. Lebedev, A. Tonyushkin, S. Pengue and A. Weis. Imaging magnetic nanoparticle distributions by atomic magnetometry-based susceptometry. *IEEE transactions on medical imaging*, 39(4):922–933, 2019.
- [Cor78] A. Corney. Atomic and laser spectroscopy. Clarendon Press Oxford, 1978.
- [Cra46] H. Cramér. Mathematical Methods of Statistics. *Princeton Landmarks in Mathematics and Physics*, 1946.
- [Cre12] G. Crevecoeur, D. Baumgarten, U. Steinhoff, J. Haueisen, L. Trahms and L. Dupré. Advancements in magnetic nanoparticle reconstruction using sequential activation of excitation coil arrays using magnetorelaxometry. *IEEE Transactions on Magnetics*, 48(4):1313–1316, 2012.
- [Dan10] H. Dang, A. C. Maloof and M. V. Romalis. Ultrahigh sensitivity magnetic field and magnetization measurements with an atomic magnetometer. *Applied Physics Letters*, 97(15):151110, 2010.
- [Das21] P. T. Das, H. Nhalil, M. Schultz, A. Grosz and L. Klein. Measurements of nanomagnetic bead relaxation dynamics using planar Hall effect magnetometer. *Journal of Applied Physics*, 129(12):124506, 2021.
- [Ded01] C. Dedman, K. Baldwin and M. Colla. Fast switching of magnetic fields in a magneto-optic trap. *Review of Scientific Instruments*, 72(11):4055–4058, 2001.

- [Deh57] H. Dehmelt. Modulation of a light beam by precessing absorbing atoms. *Physical Review*, 105(6):1924, 1957.
- [Dei14] R. J. Deissler, Y. Wu and M. A. Martens. Dependence of Brownian and Néel relaxation times on magnetic field strength. *Medical Physics*, 41(1):012301, 2014.
- [Den09] C. Dennis, A. Jackson, J. Borchers, P. Hoopes, R. Strawbridge, A. Foreman, J. Van Lierop, C. Grüttner and R. Ivkov. Nearly complete regression of tumors via collective behavior of magnetic nanoparticles in hyperthermia. *Nanotechnology*, 20(39):395103, 2009.
- [Den10] M. Denoual, S. Saez, F. Kauffman and C. Dolabdjian. Magnetorelaxometry using improved giant magnetoresistance magnetometer. *Sensors and Actuators A: Physical*, 159(2):184–188, 2010.
- [Die16] J. Dieckhoff, D. Eberbeck, M. Schilling and F. Ludwig. Magnetic-field dependence of Brownian and Néel relaxation times. *Journal of Applied Physics*, 119(4):043903, 2016.
- [Dol15] V. Dolgovskiy, V. Lebedev, S. Colombo, A. Weis, B. Michen, L. Ackermann-Hirschi and A. Petri-Fink. A quantitative study of particle size effects in the magnetorelaxometry of magnetic nanoparticles using atomic magnetometry. *Journal of Magnetism and Magnetic Materials*, 379:137–150, 2015.
- [Dol16] V. Dolgovskiy, I. Fescenko, N. Sekiguchi, S. Colombo, V. Lebedev, J. Zhang and A. Weis. A magnetic source imaging camera. *Applied Physics Letters*, 109(2):023505, 2016.
- [DR69a] J. Dupont-Roc, S. Haroche and C. Cohen-Tannoudji. Detection of very weak magnetic fields (10^{-9} gauss) by ^{87}Rb zero-field level crossing resonances. *Physics Letters A*, 28:638–639, 1969.
- [DR69b] J. Dupont-Roc, S. Haroche and C. Cohen-Tannoudji. Detection of very weak magnetic fields (10^{-9} gauss) by ^{87}Rb zero-field level crossing resonances. *Physics Letters A*, 28(9):638–639, 1969.
- [dR10] L. de Rochefort, T. Liu, B. Kressler, J. Liu, P. Spincemaille, V. Lebon, J. Wu and Y. Wang. Quantitative susceptibility map reconstruction from MR phase data using bayesian regularization: validation and application to brain imaging. *Magnetic Resonance in Medicine: An Official Journal of the International Society for Magnetic Resonance in Medicine*, 63(1):194–206, 2010.
- [Dru07] D. Drung, C. Aßmann, J. Beyer, A. Kirste, M. Peters, F. Ruede, T. Schurig, C. Hinnrichs and H. Barthelmeß. High-performance dc SQUID sensors and electronics. In IEEE/CSC & ESAS European Superconductivity News Forum, 1. 2007.

- [Dud17] G. Dudzik. Ultra-stable, low-noise two-stage current source concept for electronics and laser applications. *IET Circuits, Devices & Systems*, 11(6):613–617, 2017.
- [Dut20] S. Dutz, N. Buske, J. Landers, C. Gräfe, H. Wende and J. H. Clement. Bio-compatible magnetic fluids of co-doped iron oxide nanoparticles with tunable magnetic properties. *Nanomaterials*, 10(6):1019, 2020.
- [Ebe06] D. Eberbeck, F. Wiekhorst, U. Steinhoff and L. Trahms. Aggregation behaviour of magnetic nanoparticle suspensions investigated by magnetorelaxometry. *Journal of Physics: Condensed Matter*, 18(38):S2829, 2006.
- [Ebe11] D. Eberbeck, F. Wiekhorst, S. Wagner and L. Trahms. How the size distribution of magnetic nanoparticles determines their magnetic particle imaging performance. *Applied physics letters*, 98(18):182502, 2011.
- [Ebe13] D. Eberbeck, C. Dennis, N. Huls, K. Krycka, C. Grüttner and F. Westphal. Multicore Magnetic Nanoparticles for Magnetic Particle Imaging. *Magnetics, IEEE Transactions on*, 49:269–274, 2013.
- [Eng96] H. W. Engl, M. Hanke and A. Neubauer. Regularization of inverse problems, volume 375. Springer Science & Business Media, 1996.
- [Eri08] C. J. Erickson, M. Van Zijll, G. Doermann and D. S. Durfee. An ultrahigh stability, low-noise laser current driver with digital control. *Review of Scientific Instruments*, 79(7):073107, 2008.
- [Fer25] E. Fermi and F. Rasetti. Über den Einfluß eines wechselnden magnetischen Feldes auf die Polarisation der Resonanzstrahlung. *Zeitschrift für Physik*, 33(1):246–250, 1925.
- [Fer21] S. Fernandes, T. Fernandez, S. Metze, P. B. Balakrishnan, B. T. Mai, J. Conteh, C. De Mei, A. Turdo, S. Di Franco, G. Stassi et al. Magnetic Nanoparticle-Based Hyperthermia Mediates Drug Delivery and Impairs the Tumorigenic Capacity of Quiescent Colorectal Cancer Stem Cells. *ACS Applied Materials & Interfaces*, 2021.
- [Fri19] R.-M. Friedrich, S. Zabel, A. Galka, N. Lukat, J.-M. Wagner, C. Kirchhof, E. Quandt, J. McCord, C. Selhuber-Unkel, M. Siniatchkin et al. Magnetic particle mapping using magnetoelectric sensors as an imaging modality. *Scientific reports*, 9(1):1–11, 2019.
- [Gar96] D. Garanin. Integral relaxation time of single-domain ferromagnetic particles. *Physical Review E*, 54(4):3250, 1996.
- [Gav21] H. Gavilán, S. K. Avugadda, T. Fernández-Cabada, N. Soni, M. Cassani, B. T. Mai, R. Chantrell and T. Pellegrino. Magnetic nanoparticles and clusters for

magnetic hyperthermia: optimizing their heat performance and developing combinatorial therapies to tackle cancer. *Chemical Society Reviews*, 2021.

- [Gem10] C. Gemmel, W. Heil, S. Karpuk, K. Lenz, C. Ludwig, Y. Sobolev, K. Tullney, M. Burghoff, W. Kilian, S. Knappe-Grüneberg et al. Ultra-sensitive magnetometry based on free precession of nuclear spins. *The European Physical Journal D*, 57(3):303–320, 2010.
- [Gra21] A. V. Gramolin, D. Aybas, D. Johnson, J. Adam and A. O. Sushkov. Search for axion-like dark matter with ferromagnets. *Nature Physics*, 17(1):79–84, 2021.
- [Gro06] S. Groeger, G. Bison, J.-L. Schenker, R. Wynands and A. Weis. A high-sensitivity laser-pumped Mx magnetometer. *The European Physical Journal D-Atomic, Molecular, Optical and Plasma Physics*, 38(2):239–247, 2006.
- [Gru13] Z. D. Grujić and A. Weis. Atomic magnetic resonance induced by amplitude-, frequency-, or polarization-modulated light. *Physical Review A*, 88(1):012508, 2013.
- [Gru15] Z. D. Grujić, P. A. Koss, G. Bison and A. Weis. A sensitive and accurate atomic magnetometer based on free spin precession. *The European Physical Journal D*, 69(5):135, 2015.
- [Han24] W. Hanle. Über magnetische beeinflussung der polarisation der resonanzfluoreszenz. *Zeitschrift für Physik*, 30(1):93–105, 1924.
- [Han02] J. D. Hanson and S. P. Hirshman. Compact expressions for the Biot–Savart fields of a filamentary segment. *Physics of Plasmas*, 9(10):4410–4412, 2002.
- [Hap72] W. Happer. Optical pumping. *Reviews of Modern Physics*, 44(2):169, 1972.
- [Hap73] W. Happer and H. Tang. Spin-exchange shift and narrowing of magnetic resonance lines in optically pumped alkali vapors. *Physical Review Letters*, 31(5):273, 1973.
- [Har17] M. Harabech, J. Leliaert, A. Coene, G. Crevecoeur, D. Van Roost and L. Dupré. The effect of the magnetic nanoparticle’s size dependence of the relaxation time constant on the specific loss power of magnetic nanoparticle hyperthermia. *Journal of Magnetism and Magnetic Materials*, 426:206–210, 2017.
- [He18] S. He, H. Zhang, Y. Liu, F. Sun, X. Yu, X. Li, L. Zhang, L. Wang, K. Mao, G. Wang et al. Maximizing specific loss power for magnetic hyperthermia by hard–soft mixed ferrites. *Small*, 14(29):1800135, 2018.

- [Hea22] S. Healy, A. F. Bakuzis, P. W. Goodwill, A. Attaluri, J. W. Bulte and R. Ivkov. Clinical magnetic hyperthermia requires integrated magnetic particle imaging. *Wiley Interdisciplinary Reviews: Nanomedicine and Nanobiotechnology*, page e1779, 2022.
- [Hed18] M. Hedayati, B. Abubaker-Sharif, M. Khattab, A. Razavi, I. Mohammed, A. Nejad, M. Wabler, H. Zhou, J. Mihalic, C. Gruettner et al. An optimised spectrophotometric assay for convenient and accurate quantitation of intracellular iron from iron oxide nanoparticles. *International Journal of Hyperthermia*, 34(4):373–381, 2018.
- [Hun22] D. Hunter, T. Dyer and E. Riis. An accurate optically pumped magnetometer based on Ramsey-style interrogation. *Optics Letters*, 2022.
- [Hö15] P. Hömmen. Examination of the Effects of Measurement Uncertainties on Quantitative Imaging of Magnetic Nanoparticles Using Magnetorelaxometry. Master’s thesis, Technische Universität Ilmenau, 2015.
- [Iiv17] J. Iivanainen, M. Stenroos and L. Parkkonen. Measuring MEG closer to the brain: Performance of on-scalp sensor arrays. *NeuroImage*, 147:542–553, 2017.
- [Ing18] S. J. Ingleby, C. O’Dwyer, P. F. Griffin, A. S. Arnold and E. Riis. Vector magnetometry exploiting phase-geometry effects in a double-resonance alignment magnetometer. *Physical Review Applied*, 10(3):034035, 2018.
- [Jau20a] A. Jaufenthaler, P. Schier, T. Middelmann, M. Liebl, F. Wiekhorst and D. Baumgarten. Quantitative 2D magnetorelaxometry imaging of magnetic nanoparticles using optically pumped magnetometers. *Sensors*, 20(3):753, 2020.
- [Jau20b] A. Jaufenthaler, V. Schultze, T. Scholtes, C. B. Schmidt, M. Handler, R. Stolz and D. Baumgarten. OPM magnetorelaxometry in the presence of a DC bias field. *EPJ Quantum Technology*, 7(1):1–14, 2020.
- [Jau21] A. Jaufenthaler, T. Kornack, V. Lebedev, M. E. Limes, R. Körber, M. Liebl and D. Baumgarten. Pulsed Optically Pumped Magnetometers: Addressing Dead Time and Bandwidth for the Unshielded Magnetorelaxometry of Magnetic Nanoparticles. *Sensors*, 21(4):1212, 2021.
- [Joh12] C. Johnson, N. L. Adolphi, K. L. Butler, D. M. Lovato, R. Larson, P. D. Schwindt and E. R. Flynn. Magnetic relaxometry with an atomic magnetometer and SQUID sensors on targeted cancer cells. *Journal of Magnetism and Magnetic Materials*, 324(17):2613–2619, 2012.
- [Jur06] R. Jurgons, C. Seliger, A. Hilpert, L. Trahms, S. Odenbach and C. Alexiou. Drug loaded magnetic nanoparticles for cancer therapy. *Journal of Physics: Condensed Matter*, 18(38):S2893, 2006.

- [Kal09] M. Kallumadil, M. Tada, T. Nakagawa, M. Abe, P. Southern and Q. A. Pankhurst. Suitability of commercial colloids for magnetic hyperthermia. *Journal of Magnetism and Magnetic Materials*, 321(10):1509–1513, 2009.
- [Kan16] E. Kanal. Gadolinium based contrast agents (GBCA): Safety overview after 3 decades of clinical experience. *Magnetic resonance imaging*, 34(10):1341–1345, 2016.
- [Kas50a] A. Kastler. Quelques suggestions concernant la production optique et la détection optique d’une inégalité de population des niveaux de quantification spatiale des atomes. Application à l’expérience de Stern et Gerlach et à la résonance magnétique. *J. phys. radium*, 11(6):255–265, 1950.
- [Kas50b] A. Kastler. Some suggestions concerning the production and detection by optical means of inequalities in the populations of levels of spatial quantization in atoms. Application to the Stern and Gerlach and magnetic resonance experiments. *J. Phys. Radium*, 11(11):255–265, 1950.
- [Kas73] A. Kastler. The Hanle effect and its use for the measurements of very small magnetic fields. *Nuclear instruments and methods*, 110:259–265, 1973.
- [Kna10] S. Knappe, T. H. Sander, O. Kosch, F. Wiekhorst, J. Kitching and L. Trahms. Cross-validation of microfabricated atomic magnetometers with superconducting quantum interference devices for biomagnetic applications. *Applied Physics Letters*, 97(13):133703, 2010.
- [Kna16] S. Knappe, O. Alem, D. Sheng and J. Kitching. Microfabricated optically-pumped magnetometers for biomagnetic applications. In *Journal of Physics: Conference Series*, volume 723, page 012055. IOP Publishing, 2016.
- [Kob11] K. Kobayashi, M. Yoshizawa and Y. Uchikawa. Wide dynamic range analog FLL system using high- T_c SQUID for biomagnetic measurements. *IEEE transactions on magnetics*, 47(10):2871–2873, 2011.
- [Kom03] I. Kominis, T. Kornack, J. Allred and M. V. Romalis. A subfemtotesla multi-channel atomic magnetometer. *Nature*, 422(6932):596–599, 2003.
- [Kor07] T. Kornack, S. Smullin, S.-K. Lee and M. Romalis. A low-noise ferrite magnetic shield. *Applied physics letters*, 90(22):223501, 2007.
- [Köt95] R. Kötz, P. Fannin and L. Trahms. Time domain study of Brownian and Néel relaxation in ferrofluids. *Journal of magnetism and magnetic materials*, 149(1-2):42–46, 1995.
- [Kuw20] A. Kuwahata, T. Kitaizumi, K. Saichi, T. Sato, R. Igarashi, T. Ohshima, Y. Masuyama, T. Iwasaki, M. Hatano, F. Jelezko et al. Magnetometer with nitrogen-vacancy center in a bulk diamond for detecting magnetic nanoparticles in biomedical applications. *Scientific reports*, 10(1):1–9, 2020.

- [Lan02] J. Lange, R. Kötitz, A. Haller, L. Trahms, W. Semmler and W. Weitschies. Magnetorelaxometry—A new binding specific detection method based on magnetic nanoparticles. *Journal of magnetism and magnetic materials*, 252:381–383, 2002.
- [Leb20] V. Lebedev, S. Hartwig and T. Middelmann. Fast and robust optically pumped cesium magnetometer. *Advanced Optical Technologies*, 1(ahead-of-print), 2020.
- [Lebed] V. Lebedev, A. Jaufenthaler, T. Middelmann and D. Baumgarten. Unshielded High Bandwidth Magnetorelaxometry of Magnetic Nanoparticles with Optically Pumped Magnetometers. In *High Performance Magnetic Field Sensors for On-Scalp Magnetoencephalography and Other Applications*. Springer, Accepted.
- [Lee14] J.-J. Lee, K. J. Jeong, M. Hashimoto, A. H. Kwon, A. Rwei, S. A. Shankarappa, J. H. Tsui and D. S. Kohane. Synthetic ligand-coated magnetic nanoparticles for microfluidic bacterial separation from blood. *Nano letters*, 14(1):1–5, 2014.
- [Lee21] W. Lee, V. Lucivero, M. Romalis, M. Limes, E. Foley and T. Kornack. Heading errors in all-optical alkali-vapor magnetometers in geomagnetic fields. *arXiv preprint arXiv:2103.01358*, 2021.
- [Leh] J. Lehmann and C. Cohen-Tannoudji. Pompage optique en champ magnetique faible.
- [Lel14] J. Leliaert, A. Coene, G. Crevecoeur, A. Vansteenkiste, D. Eberbeck, F. Wiekhorst, B. Van Waeyenberge and L. Dupré. Regarding the Néel relaxation time constant in magnetorelaxometry. *Journal of Applied Physics*, 116(16):163914, 2014.
- [Len14] L. Lenci, A. Auyuanet, S. Barreiro, P. Valente, A. Lezama and H. Failache. Vectorial atomic magnetometer based on coherent transients of laser absorption in Rb vapor. *Physical Review A*, 89(4):043836, 2014.
- [Li06] Z. Li, R. T. Wakai and T. G. Walker. Parametric modulation of an atomic magnetometer. *Applied physics letters*, 89(13):134105, 2006.
- [Li20] R. Li, F. N. Baynes, A. N. Luiten and C. Perrella. Continuous High-Sensitivity and High-Bandwidth Atomic Magnetometer. *Physical Review Applied*, 14(6):064067, 2020.
- [Lib93] K. Libbrecht and J. L. Hall. A low-noise high-speed diode laser current controller. *Review of scientific instruments*, 64(8):2133–2135, 1993.
- [Lie14] M. Liebl, U. Steinhoff, F. Wiekhorst, J. Haueisen and L. Trahms. Quantitative imaging of magnetic nanoparticles by magnetorelaxometry with multiple excitation coils. *Physics in Medicine & Biology*, 59(21):6607, 2014.

- [Lie15] M. Liebl, F. Wiekhorst, D. Eberbeck, P. Radon, D. Gutkelch, D. Baumgarten, U. Steinhoff and L. Trahms. Magnetorelaxometry procedures for quantitative imaging and characterization of magnetic nanoparticles in biomedical applications. *Biomedical Engineering/Biomedizinische Technik*, 60(5):427–443, 2015.
- [Lie16] M. Liebl. Quantitative Bildgebung magnetischer Nanopartikel mittels magnetrelaxometrischer Tomographie für biomedizinische Anwendungen. Ph.D. thesis, Technischen Universität Ilmenau, 2016. <https://nbn-resolving.org/urn:nbn:de:gbv:ilm1-2016000744>.
- [Lim20] M. Limes, E. Foley, T. Kornack, S. Caliga, S. McBride, A. Braun, W. Lee, V. Lucivero and M. Romalis. Portable magnetometry for detection of biomagnetism in ambient environments. *Physical Review Applied*, 14(1):011002, 2020.
- [Liu11] P. Liu, K. Skucha, M. Megens and B. Boser. A CMOS Hall-effect sensor for the characterization and detection of magnetic nanoparticles for biomedical applications. *IEEE transactions on magnetics*, 47(10):3449–3451, 2011.
- [Loe09] M. R. Loebinger, P. G. Kyrtatos, M. Turmaine, A. N. Price, Q. Pankhurst, M. F. Lythgoe and S. M. Janes. Magnetic resonance imaging of mesenchymal stem cells homing to pulmonary metastases using biocompatible magnetic nanoparticles. *Cancer research*, 69(23):8862–8867, 2009.
- [Lüb96] A. S. Lübbe, C. Bergemann, H. Riess, F. Schriever, P. Reichardt, K. Possinger, M. Matthias, B. Dörken, F. Herrmann, R. Gürtler et al. Clinical experiences with magnetic drug targeting: a phase I study with 4'-epidoxorubicin in 14 patients with advanced solid tumors. *Cancer research*, 56(20):4686–4693, 1996.
- [Lüb01] A. S. Lübbe, C. Alexiou and C. Bergemann. Clinical applications of magnetic drug targeting. *Journal of Surgical Research*, 95(2):200–206, 2001.
- [Lud05a] F. Ludwig, E. Heim, S. Mäuselein, D. Eberbeck and M. Schilling. Magnetorelaxometry of magnetic nanoparticles with fluxgate magnetometers for the analysis of biological targets. *Journal of magnetism and magnetic materials*, 293(1):690–695, 2005.
- [Lud05b] F. Ludwig, S. Mäuselein, E. Heim and M. Schilling. Magnetorelaxometry of magnetic nanoparticles in magnetically unshielded environment utilizing a differential fluxgate arrangement. *Review of scientific instruments*, 76(10):106102, 2005.
- [Lud06] F. Ludwig, E. Heim, D. Menzel and M. Schilling. Investigation of superparamagnetic Fe₃O₄ nanoparticles by fluxgate magnetorelaxometry for use in magnetic relaxation immunoassays. *Journal of applied physics*, 99(8):08P106, 2006.

- [Lud09] F. Ludwig, E. Heim, D. Eberbeck, K. Schwarz, L. Trahms and M. Schilling. Comparison and calibration of fluxgate and SQUID magnetorelaxometry techniques for the characterization of magnetic core-shell nanoparticles. *IEEE Transactions on Magnetics*, 45(10):4857–4860, 2009.
- [Mar22] U. Marhl, A. Jodko-Władzińska, R. Brühl, T. Sander and V. Jazbinšek. Transforming and comparing data between standard SQUID and OPM-MEG systems. *PloS one*, 17(1):e0262669, 2022.
- [Mat17] A. N. Matlashov, V. K. Semenov and W. H. Anderson. AC defluxing of SQUIDS. *IEEE Transactions on Applied Superconductivity*, 27(4):1–5, 2017.
- [Mod14] V. V. Mody, A. Cox, S. Shah, A. Singh, W. Bevins and H. Parihar. Magnetic nanoparticle drug delivery systems for targeting tumor. *Applied Nanoscience*, 4(4):385–392, 2014.
- [Moh00] P. J. Mohr and B. N. Taylor. CODATA recommended values of the fundamental physical constants: 1998. *Reviews of modern physics*, 72(2):351, 2000.
- [Mol82] R. S. Molday and D. Mackenzie. Immunospecific ferromagnetic iron-dextran reagents for the labeling and magnetic separation of cells. *Journal of immunological methods*, 52(3):353–367, 1982.
- [Mot11] K. Motomura, M. Ishitobi, Y. Komoike, H. Koyama, A. Noguchi, H. Sumino, Y. Kumatani, H. Inaji, T. Horinouchi and K. Nakanishi. SPIO-enhanced magnetic resonance imaging for the detection of metastases in sentinel nodes localized by computed tomography lymphography in patients with breast cancer. *Annals of surgical oncology*, 18(12):3422–3429, 2011.
- [Née49] L. Néel. Théorie du traînage magnétique des ferromagnétiques en grains fins avec applications aux terres cuites. *Ann. géophys.*, 5:99–136, 1949.
- [Oel20] G. Oelsner, R. IJsselsteijn, T. Scholtes, A. Krüger, V. Schultze, G. Seyffert, G. Werner, M. Jäger, A. Chwala and R. Stolz. Integrated optically pumped magnetometer for measurements within Earth’s magnetic field. *arXiv preprint arXiv:2008.01570*, 2020.
- [Ort13] D. Ortega and Q. A. Pankhurst. Magnetic hyperthermia. *Nanoscience*, 1(60):e88, 2013.
- [Osb18] J. Osborne, J. Orton, O. Alem and V. Shah. Fully integrated standalone zero field optically pumped magnetometer for biomagnetism. In *Steep Dispersion Engineering and Opto-Atomic Precision Metrology XI*, volume 10548, page 105481G. International Society for Optics and Photonics, 2018.
- [Pan03] Q. A. Pankhurst, J. Connolly, S. K. Jones and J. Dobson. Applications of magnetic nanoparticles in biomedicine. *Journal of physics D: Applied physics*, 36(13):R167, 2003.

- [Pan09] Q. Pankhurst, N. Thanh, S. Jones and J. Dobson. Progress in applications of magnetic nanoparticles in biomedicine. *Journal of Physics D: Applied Physics*, 42(22):224001, 2009.
- [Ped21] D. Peddis, S. Laureti and D. Fiorani. *New Trends in Nanoparticle Magnetism*. Springer, 2021.
- [Per] C. Perrella, K. Netz, R. Li and A. Luiten. High-bandwidth optical magnetometry via phase retrieval. Abstract, *Hot Vapor Workshop*, 2021.
- [Pra21] E. J. Pratt, M. Ledbetter, R. Jiménez-Martínez, B. Shapiro, A. Solon, G. Z. Iwata, S. Garber, J. Gormley, D. Decker, D. Delgadillo et al. Kernel Flux: a whole-head 432-magnetometer optically-pumped magnetoencephalography (OP-MEG) system for brain activity imaging during natural human experiences. In *Optical and Quantum Sensing and Precision Metrology*, volume 11700, page 1170032. International Society for Optics and Photonics, 2021.
- [Pyr21] T. Pyragius and K. Jensen. A high performance active noise control system for magnetic fields. *Review of Scientific Instruments*, 92(12):124702, 2021.
- [QuS] QuSpin. About Us. <http://quspin.com/about-us/>. Accessed: March 2022.
- [Rai94] Y. L. Raikher and M. I. Shliomis. The effective field method in the orientational kinetics of magnetic fluids and liquid crystals. *Advances in Chemical Physics*, 87:595–752, 1994.
- [Rao92] C. R. Rao. Information and the accuracy attainable in the estimation of statistical parameters. In *Breakthroughs in statistics*, pages 235–247. Springer, 1992.
- [Ree14] D. B. Reeves and J. B. Weaver. Approaches for modeling magnetic nanoparticle dynamics. *Critical ReviewsTM in Biomedical Engineering*, 42(1), 2014.
- [Rei03] P. Reimer and T. Balzer. Ferucarbotran (Resovist): a new clinically approved RES-specific contrast agent for contrast-enhanced MRI of the liver: properties, clinical development, and applications. *European radiology*, 13(6):1266–1276, 2003.
- [Rem15] H. Remmer, J. Dieckhoff, M. Schilling and F. Ludwig. Suitability of magnetic single- and multi-core nanoparticles to detect protein binding with dynamic magnetic measurement techniques. *Journal of Magnetism and Magnetic Materials*, 380:236–240, 2015.
- [Ric10] H. Richter, M. Kettering, F. Wiekhorst, U. Steinhoff, I. Hilger and L. Trahms. Magnetorelaxometry for localization and quantification of magnetic nanoparticles for thermal ablation studies. *Physics in Medicine & Biology*, 55(3):623, 2010.

- [Ril03] G. Rilling, P. Flandrin, P. Goncalves et al. On empirical mode decomposition and its algorithms. In IEEE-EURASIP workshop on nonlinear signal and image processing, volume 3, pages 8–11. Citeseer, 2003.
- [Roc10] S. M. Rochester. Modeling nonlinear magneto-optical effects in atomic vapors. University of California, Berkeley, 2010.
- [Roc12] S. Rochester, M. Ledbetter, T. Zigdon, A. Wilson-Gordon and D. Budker. Orientation-to-alignment conversion and spin squeezing. *Physical Review A*, 85(2):022125, 2012.
- [Rom02] E. Romanus, M. Hückel, C. Gross, S. Prass, W. Weitschies, R. Bräuer and P. Weber. Magnetic nanoparticle relaxation measurement as a novel tool for in vivo diagnostics. *Journal of magnetism and magnetic materials*, 252:387–389, 2002.
- [Rom10] M. Romalis. Hybrid optical pumping of optically dense alkali-metal vapor without quenching gas. *Physical review letters*, 105(24):243001, 2010.
- [Ros07] M. A. Rosenberry, J. Reyes, D. Tupa and T. J. Gay. Radiation trapping in rubidium optical pumping at low buffer-gas pressures. *Physical Review A*, 75(2):023401, 2007.
- [RR21] I. Rubia-Rodríguez, A. Santana-Otero, S. Spassov, E. Tombácz, C. Johansson, P. De La Presa, F. J. Teran, M. del Puerto Morales, S. Veintemillas-Verdaguer, N. T. Thanh et al. Whither Magnetic Hyperthermia? A Tentative Roadmap. *Materials*, 14(4):706, 2021.
- [Rüh09] D. Rühmer, E. Heim, T. Wawrzik, F. Ludwig and M. Schilling. Magnetic Relaxation Imaging of Magnetic Nanoparticle Distributions. In World Congress on Medical Physics and Biomedical Engineering, September 7-12, 2009, Munich, Germany, pages 418–420. Springer, 2009.
- [San21] T. Sander, U. Marhl, R. Brühl, T. Middelman and V. Jazbinšek. A 50 channel optically pumped magnetometer MEG in an externally actively shielded two-layer room. *International Journal of Bioelectromagnetism*, 23(1):5/1–4, 2021.
- [Sar09a] S. Sarangi, I. Tan and A. Brazdeikis. Magnetic imaging method based on magnetic relaxation of magnetic nanoparticles. *Journal of Applied Physics*, 105(9):093926, 2009.
- [Sar09b] S. Sarangi, I.-C. Tan and A. Brazdeikis. Magnetic imaging method based on magnetic relaxation of magnetic nanoparticles. *Journal of Applied Physics*, 105:093926 – 093926, 2009.
- [Sar11] S. Sarangi, I. Tan and A. Brazdeikis. Brownian relaxation of interacting magnetic nanoparticles in a colloid subjected to a pulsatile magnetic field. *Journal of nanoscience and nanotechnology*, 11(5):4136–4141, 2011.

- [Sav17] I. Savukov, Y. Kim, V. Shah and M. Boshier. High-sensitivity operation of single-beam optically pumped magnetometer in a kHz frequency range. *Measurement Science and Technology*, 28(3):035104, 2017.
- [Sch05] P. Schwindt, L. Hollberg and J. Kitching. Self-oscillating rubidium magnetometer using nonlinear magneto-optical rotation. *Review of Scientific Instruments*, 76(12):126103, 2005.
- [Sch09] T. Schurig and L. Trahms. SQUID Activities at PTB: Status 2008. In IEEE&ESAS European Superconductivity News Forum, volume 8. 2009.
- [Sch10] V. Schultze, R. IJsselsteijn and H.-G. Meyer. Noise reduction in optically pumped magnetometer assemblies. *Applied Physics B*, 100(4):717–724, 2010.
- [Sch11] T. Scholtes, V. Schultze, R. IJsselsteijn, S. Woetzel and H.-G. Meyer. Light-narrowed optically pumped Mx magnetometer with a miniaturized Cs cell. *Physical Review A*, 84(4):043416, 2011.
- [Sch12] V. Schultze, R. IJsselsteijn, T. Scholtes, S. Woetzel and H.-G. Meyer. Characteristics and performance of an intensity-modulated optically pumped magnetometer in comparison to the classical Mx magnetometer. *Optics Express*, 20(13):14201–14212, 2012.
- [Sch15a] T. Scholtes. Optisch gepumpte Magnetometer mit reduzierter Spin-Austausch-Relaxation im Erdmagnetfeld. Ph.D. thesis, Friedrich-Schiller-Universität Jena, 2015.
- [Sch15b] V. Schultze, T. Scholtes, R. IJsselsteijn and H.-G. Meyer. Improving the sensitivity of optically pumped magnetometers by hyperfine repumping. *JOSA B*, 32(5):730–736, 2015.
- [Sch16] T. Scholtes, S. Pustelny, S. Fritzsche, V. Schultze, R. Stolz and H.-G. Meyer. Suppression of spin-exchange relaxation in tilted magnetic fields within the geophysical range. *Physical Review A*, 94(1):013403, 2016.
- [Sch17a] M. Schmelz and R. Stolz. Superconducting Quantum Interference Device (SQUID) Magnetometers. In *High Sensitivity Magnetometers*, pages 279–311. Springer, 2017.
- [Sch17b] D. Schmidt, D. Eberbeck, U. Steinhoff and F. Wiekhorst. Finding the magnetic size distribution of magnetic nanoparticles from magnetization measurements via the iterative Kaczmarz algorithm. *Journal of Magnetism and Magnetic Materials*, 431:33–37, 2017.
- [Sch19a] P. Schier, C. Barton, S. Spassov, C. Johansson, D. Baumgarten, O. Kazakova, P. Southern, Q. Pankhurst, M. Coisson, C. Grüttner et al. European research on magnetic nanoparticles for biomedical applications: standardisation

- aspects. In Polish Conference on Biocybernetics and Biomedical Engineering, pages 316–326. Springer, 2019.
- [Sch19b] P. Schier, M. Liebl, U. Steinhoff, M. Handler, F. Wiekhorst and D. Baumgarten. Optimizing Excitation Coil Currents for Advanced Magnetorelaxometry Imaging. *Journal of Mathematical Imaging and Vision*, pages 1–15, 2019.
- [Sch21] P. Schier, A. Coene, A. Jaufenthaler and D. Baumgarten. Evaluating selection criteria for optimized excitation coils in magnetorelaxometry imaging. *Physics in Medicine & Biology*, 66(23):235001, 2021.
- [Sec16] C. M. Seck, P. J. Martin, E. C. Cook, B. C. Odom and D. A. Steck. Noise reduction of a Libbrecht–Hall style current driver. *Review of Scientific Instruments*, 87(6):064703, 2016.
- [Sey21] R. A. Seymour, N. Alexander, S. Mellor, G. C. O’Neill, T. M. Tierney, G. R. Barnes and E. A. Maguire. Interference suppression techniques for OPM-based MEG: Opportunities and challenges. *NeuroImage*, page 118834, 2021.
- [SG13] A. Santillán-Guzmán, M. Fischer, U. Heute and G. Schmidt. Real-time empirical mode decomposition for EEG signal enhancement. In 21st European Signal Processing Conference (EUSIPCO 2013), pages 1–5. IEEE, 2013.
- [SHA03] SHARP Corporation. PC817X Series, 2003.
- [Sha13] V. K. Shah and R. T. Wakai. A compact, high performance atomic magnetometer for biomedical applications. *Physics in Medicine & Biology*, 58(22):8153, 2013.
- [She13] D. Sheng, S. Li, N. Dural and M. V. Romalis. Subfemtotesla scalar atomic magnetometry using multipass cells. *Physical Review Letters*, 110(16):160802, 2013.
- [Shi15] T.-H. Shin, Y. Choi, S. Kim and J. Cheon. Recent advances in magnetic nanoparticle-based multi-modal imaging. *Chemical Society Reviews*, 44(14):4501–4516, 2015.
- [Shl94] M. Shliomis and V. Stepanov. Theory of the dynamic susceptibility of magnetic fluids. *Advances in Chemical Physics: Relaxation Phenomena in Condensed Matter*, 87:1–30, 1994.
- [Shu09] V. I. Shubayev, T. R. Pisanic II and S. Jin. Magnetic nanoparticles for theragnostics. *Advanced drug delivery reviews*, 61(6):467–477, 2009.
- [SL15] D. Schmid-Lorch, T. Häberle, F. Reinhard, A. Zappe, M. Slota, L. Bogani, A. Finkler and J. Wrachtrup. Relaxometry and dephasing imaging of superparamagnetic magnetite nanoparticles using a single qubit. *Nano letters*, 15(8):4942–4947, 2015.

- [Son09] T. Song, L. Cui, K. Gaa, L. Feffer, S. Taulu, R. R. Lee and M. Huang. Signal space separation algorithm and its application on suppressing artifacts caused by vagus nerve stimulation for magnetoencephalography recordings. *Journal of Clinical Neurophysiology*, 26(6):392–400, 2009.
- [Ste01] D. A. Steck. Rubidium 87 D line data, 2001.
- [Sto16] J.-H. Storm, D. Drung, M. Burghoff and R. Körber. A modular, extendible and field-tolerant multichannel vector magnetometer based on current sensor SQUIDs. *Superconductor Science and Technology*, 29(9):094001, 2016.
- [Sun08] C. Sun, J. S. Lee and M. Zhang. Magnetic nanoparticles in MR imaging and drug delivery. *Advanced drug delivery reviews*, 60(11):1252–1265, 2008.
- [Tan21a] J. Tang, Y. Yin, Y. Zhai, B. Zhou, B. Han, H. Yang and G. Liu. Transient dynamics of atomic spin in the spin-exchange-relaxation-free regime. *Optics Express*, 29(6):8333–8343, 2021.
- [Tan21b] J. Tang, Y. Zhai, B. Zhou, B. Han and G. Liu. Dual-Axis Closed Loop of a Single-Beam Atomic Magnetometer: Toward High Bandwidth and High Sensitivity. *IEEE Transactions on Instrumentation and Measurement*, 70:1–8, 2021.
- [Tei15] L. Teich and C. Schröder. Hybrid Molecular and Spin Dynamics Simulations for Ensembles of Magnetic Nanoparticles for Magnetoresistive Systems. *Sensors*, 15(11):28826–28841, 2015.
- [Thi07] F. Thiel, A. Schnabel, S. Knappe-Grüneberg, D. Stollfuß and M. Burghoff. Demagnetization of magnetically shielded rooms. *Review of scientific instruments*, 78(3):035106, 2007.
- [Tie21] T. M. Tierney, N. Alexander, S. Mellor, N. Holmes, R. Seymour, G. C. O’Neill, E. A. Maguire and G. R. Barnes. Modelling optically pumped magnetometer interference in MEG as a spatially homogeneous magnetic field. *NeuroImage*, 244:118484, 2021.
- [Tum07] S. Tumanski. Induction coil sensors—A review. *Measurement Science and Technology*, 18(3):R31, 2007.
- [Ver20] A. Vershovskii, A. Pazgalev and M. Petrenko. All-Optical Magnetometric Sensor for Magnetoencephalography and Ultralow Field Tomography. *Technical Physics Letters*, 46(9):877–880, 2020.
- [vG20] A. von Gladiss, M. Graeser, A. Cordes, A. C. Bakenecker, A. Behrends, X. Chen and T. M. Buzug. Investigating spatial resolution, field sequences and image reconstruction strategies using hybrid phantoms in MPI. *International Journal on Magnetic Particle Imaging*, 6(1), 2020.

- [Vie20] T. Viereck, S. Draack, M. Kuester, M. Schilling and F. Ludwig. Initial imaging experiments with a direct-driven relaxation Magnetic Particle Imaging setup. *International Journal on Magnetic Particle Imaging*, 6(2 Suppl 1), 2020.
- [Wah18] J. Wahsner, E. M. Gale, A. Rodríguez-Rodríguez and P. Caravan. Chemistry of MRI contrast agents: current challenges and new frontiers. *Chemical reviews*, 119(2):957–1057, 2018.
- [Wan15] Y.-X. J. Wang. Current status of superparamagnetic iron oxide contrast agents for liver magnetic resonance imaging. *World journal of gastroenterology*, 21(47):13400, 2015.
- [Wan20] T. Wang, W. Lee, M. Romalis, M. Limes, T. Kornack and E. Foley. Pulsed ^{87}Rb vector magnetometer using a fast rotating field. *Bulletin of the American Physical Society*, 65, 2020.
- [War99] L. Warzemann, J. Schambach, P. Weber, W. Weitschies and R. Kötz. LTS SQUID gradiometer system for in vivo magnetorelaxometry. *Superconductor Science and Technology*, 12(11):953, 1999.
- [Wei07] J. Weizenecker, J. Borgert and B. Gleich. A simulation study on the resolution and sensitivity of magnetic particle imaging. *Physics in Medicine & Biology*, 52(21):6363, 2007.
- [Wei17] A. Weis, G. Bison and Z. D. Grujić. Magnetic resonance based atomic magnetometers. In *High Sensitivity Magnetometers*, pages 361–424. Springer, 2017.
- [Wie09] F. Wiekhorst, U. Steinhoff, D. Eberbeck, K. Schwarz, H. Richter, R. Renner, M. Roessner, C. Rudolph and L. Trahms. Quantification of magnetic nanoparticle concentration in pig lung tissue after magnetic aerosol drug targeting by magnetorelaxometry. In *4th European Conference of the International Federation for Medical and Biological Engineering*, pages 2326–2329. Springer, 2009.
- [Wie12a] F. Wiekhorst, U. Steinhoff, D. Eberbeck and L. Trahms. Magnetorelaxometry assisting biomedical applications of magnetic nanoparticles. *Pharmaceutical research*, 29(5):1189–1202, 2012.
- [Wie12b] F. Wiekhorst, U. Steinhoff, D. Eberbeck and L. Trahms. Magnetorelaxometry assisting biomedical applications of magnetic nanoparticles. *Pharmaceutical research*, 29(5):1189–1202, 2012.
- [Wil20] N. Wilson, C. Perrella, R. Anderson, A. Luiten and P. Light. Wide-bandwidth atomic magnetometry via instantaneous-phase retrieval. *Physical Review Research*, 2(1):013213, 2020.
- [Woe11] S. Woetzel, V. Schultze, R. Ijsselsteijn, T. Schulz, S. Anders, R. Stolz and H.-G. Meyer. Microfabricated atomic vapor cell arrays for magnetic field measurements. *The Review of Scientific Instruments*, 82:033111, 2011.

- [Zha21] R. Zhang, R. Mhaskar, K. Smith, E. Balasubramaniam and M. Prouty. Vector measurements using all optical scalar atomic magnetometers. *Journal of Applied Physics*, 129(4):044502, 2021.
- [Zhe20] W. Zheng, S. Su, G. Zhang, X. Bi and Q. Lin. Vector magnetocardiography measurement with a compact elliptically polarized laser-pumped magnetometer. *Biomedical optics express*, 11(2):649–659, 2020.
- [Zho17] X. Zhou, C.-C. Huang and D. A. Hall. Giant magnetoresistive biosensor array for detecting magnetorelaxation. *IEEE transactions on biomedical circuits and systems*, 11(4):755–764, 2017.

Scientific contributions

Dipl.-Ing. Mag. rer. nat. Aaron Jaufenthaler BSc.

Peer-reviewed publications

1. **A. Jaufenthaler**, T. Kornack, V. Lebedev, M. E. Limes, R. Körber, M. Liebl and D. Baumgarten. Pulsed optically pumped magnetometers: Addressing dead time and bandwidth for unshielded magnetorelaxometry of magnetic nanoparticles. *Sensors*, 21(4):1212, 2021. <https://doi.org/10.3390/s21041212>
2. P. Schier, A. Coene, **A. Jaufenthaler** and D. Baumgarten. Evaluating selection criteria for optimized excitation coils in magnetorelaxometry imaging. *Physics in Medicine & Biology*, 2021. <https://doi.org/10.1088/1361-6560/ac36e8>
3. **A. Jaufenthaler**, P. Schier, T. Middelman, M. Liebl, F. Wiekhorst and D. Baumgarten. Quantitative 2D Magnetorelaxometry Imaging of Magnetic Nanoparticles using Optically Pumped Magnetometers. *Sensors*, 20(3):753, 2020. <https://doi.org/10.3390/s20030753>
4. **A. Jaufenthaler**, V. Schultze, T. Scholtes, C. B. Schmidt, M. Handler, R. Stolz and D. Baumgarten. OPM magnetorelaxometry in the presence of a DC bias field. Special issue on Quantum Magnetometers. *EPJ Quantum Technology*, 7(1):1–14, 2020. <https://doi.org/10.1140/epjqt/s40507-020-00087-3>

Book chapter

1. V. Lebedev, **A. Jaufenthaler**, T. Middelman and D. Baumgarten. Unshielded High Bandwidth Magnetorelaxometry of Magnetic Nanoparticles with Optically Pumped Magnetometers. In High Performance Magnetic Field Sensors for On-Scalp Magnetoencephalography and Other Applications, Springer, Accepted.

Poster presentations at scientific conferences

1. **A. Jaufenthaler**, P. Schier and D. Baumgarten. Towards unshielded magnetorelaxometry imaging of magnetic nanoparticles using pulsed OPM. *Workshop on Optically Pumped Magnetometers (WOPM-2021)*, October 4-5, 2021.

2. **A. Jaufenthaler**, P. Schier, T. Middelmann, M. Liebl, D. Eberbeck, D. Baumgarten. Quantitative 2D magnetorelaxometry imaging of magnetic nanoparticles using optically pumped magnetometers. *IEEE Advances in Magnetism (IEEE-AIM 2020-21)*, online, June 13-16, 2021.
3. **A. Jaufenthaler**, P. Schier, T. Middelmann, M. Liebl, C. B. Schmidt, T. Scholtes, G. Oelsner, V. Schultze, R. Stolz, T. Kornack and D. Baumgarten, Quantitative Imaging of Magnetic Nanoparticles with Magnetorelaxometry and Optically Pumped Magnetometers. *3rd Ilmenau Symposium on Medical Application of Magnetic Nanoparticles and Ferrofluids (ISMAP 2019)*, TU Ilmenau, August 27-28, 2019.
4. **A. Jaufenthaler** and D. Baumgarten, Quantitative Biomedical Imaging of Magnetic Nanoparticles with Magnetorelaxometry by Exploiting Optically Pumped Magnetometers. *CRC 1261 Summer School 2019, Magnetic sensing and applications in medicine and industry – state of the art and new prospects*, Kiel, August 19-21, 2019.
5. **A. Jaufenthaler**, C. B. Schmidt, T. Scholtes, G. Oelsner, V. Schultze, R. Stolz and D. Baumgarten. OPM magnetorelaxometry in the presence of a DC bias field. *Workshop on Optically Pumped Magnetometers (WOPM-2019)*, August 14-16, 2019.
6. **A. Jaufenthaler**, T. Kornack and D. Baumgarten, Pulsed OPM in Magnetorelaxometry of Magnetic Nanoparticles: Analyzing OPM's Free Precession Signals. *Quantum Sensing & Magnetometry - from the nanoscale up to geological explorations (QSM2019)*, August 12-14, 2019.
7. **A. Jaufenthaler**, T. Kornack, D. Baumgarten, Pulsed optically pumped magnetometers: addressing optically pumped magnetometer dead time for magnetorelaxometry of magnetic nanoparticles. *International Conference on Fine Particle Magnetism (ICFPM19)*, Gijon, May 27-31, 2019.
8. **A. Jaufenthaler** and D. Baumgarten, A novel approach for quantitative reconstruction of floating magnetic nanoparticles using randomised Kaczmarz algorithm. *15th International Workshop on Optimization and Inverse Problems in Electromagnetism (OIPE2018)*, September 11-13, 2018.
9. **A. Jaufenthaler**, T. Sander, K. Rolfs and D. Baumgarten. Quantification of magnetic nanoparticles using magnetorelaxometry and optically pumped magnetometers. *21st International Conference on Biomagnetism (BIOMAG2018)*, August 26-30, 2018.
10. **A. Jaufenthaler**, T. Middelmann, M. Liebl, K. Rolfs, T. Sander, D. Baumgarten. Quantification of Magnetic Nanoparticles using Magnetorelaxometry with Optically Pumped Magnetometers. *Workshop on Optically Pumped Magnetometers (WOPM-2018)*, August 25, 2018.

11. **A. Jaufenthaler** and D. Baumgarten. Simulation of a novel approach for quantitative floating magnetic nanoparticle reconstruction. *World Congress on Medical Physics and Biomedical Engineering (IUPESM2018)*, June 3-8, 2018.
12. **A. Jaufenthaler** and D. Baumgarten. Exploiting Optically Pumped Magnetometer's Flexibility To Optimize The Problem Conditioning In Magnetorelaxometry Imaging. *Workshop on Optically Pumped Magnetometers (WOPM-2017)*, August 21-22, 2017.

Oral presentations at scientific conferences

1. **A. Jaufenthaler** and D. Baumgarten. Magnetorelaxometry using Twinleaf's OMG. *Workshop on Optically Pumped Magnetometers (μ WOPM2020)*, online, October 15-16, 2020.
2. **A. Jaufenthaler**, T. Middelmann, M. Liebl, D. Eberbeck, D. Baumgarten. Quantitative 1d-reconstruction of magnetic nanoparticles using magnetorelaxometry and optically pumped magnetometers. *53rd Annual Conference of the German Society for Biomedical Engineering (BMT2019)*, September 25-26, Frankfurt am Main, 2019.
3. **A. Jaufenthaler**, T. Kornack, D. Baumgarten. Pulsed optically pumped magnetometers: addressing optically pumped magnetometer dead time for magnetorelaxometry of magnetic nanoparticles. *Today's Noise Tomorrow's Signal (TNTS2019)*, Berlin, February 13-15, 2019.

Invited oral presentations

1. **A. Jaufenthaler** and D. Baumgarten. Low dead time, wide bandwidth optically pumped magnetometer for unshielded magnetorelaxometry of magnetic nanoparticles. *Photonics Workshop*, Kopaonik, March 13 – 16, 2022.
2. **A. Jaufenthaler** and D. Baumgarten. Quantification and imaging of magnetic nanoparticles with magnetorelaxometry and optically pumped magnetometers. *Seminar of the working group Quantum Systems at the Leibniz-IPHT Jena*, February 16, 2021.

Danksagung

Mein ganz besonderer Dank gilt Herrn Univ.-Prof. Dr.-Ing. Daniel Baumgarten, der diese Arbeit angeregt und mir dadurch die Möglichkeit gegeben hat, an diesem spannenden, sowie interdisziplinären Thema zu arbeiten. Danke für die vielen Diskussionen und die stets außerordentlich wertvollen Ratschläge.

Ein weiterer Dank gilt meinen Arbeitskollegen der UMIT Tirol für das angenehme Arbeitsumfeld. Ein spezieller Dank gilt dabei Peter Schier für die vielen wertvollen Diskussionen.

Ein großer Dank geht an die Kollegen vom Leibniz-IPHT Jena für die konstruktive Zusammenarbeit und die schöne Zeit in Jena.

I would like to thank my colleagues from PTB Berlin for the good collaboration and the possibility to use the core facility equipment.

Thanks to QuSpin and Twinleaf for the helpful support and the possibility of special-purpose solutions.

Meiner Frau Julia, meiner Schwester Patricia, meinen Eltern und meinen Freunden gilt ein besonderes Dankeschön für die vielseitige Unterstützung.

Verpflichtungs- und Einverständniserklärung

Ich erkläre, dass ich meine Dissertation selbständig verfasst und alle in ihr verwendeten Unterlagen, Hilfsmittel und die zugrunde gelegte Literatur genannt habe.

Ich nehme zur Kenntnis, dass auch bei auszugsweiser Veröffentlichung meiner Dissertation die Universität, das/die Institut/e und der/die Arbeitsbereich/e, an dem/denen die Dissertation ausgearbeitet wurde, und die Betreuerin/nen bzw. der/die Betreuer zu nennen sind.

Ich nehme zur Kenntnis, dass meine Dissertation zur internen Dokumentation und Archivierung sowie zur Abgleichung mit der Plagiatssoftware elektronisch im Dateiformat „pdf“ ohne Kennwortschutz bei der/dem Betreuerin/Betreuer einzureichen ist, wobei auf die elektronisch archivierte Dissertation nur die/der Betreuerin/Betreuer der Dissertation und das studienrechtliche Organ Zugriff haben.

Hall in Tirol, am 26.05.2022

.....
Aaron Jaufenthaler